UNIVERSITY OF
LIVERPOOL

Department Of Engineering

PhD Thesis

Circular Laser Beam Intensity Profile Shaping for Uniform Surface Treatments

Thesis submitted in accordance with the requirements of the University of Liverpool for the degree of Doctor in Philosophy

By

Daniel Wellburn

2010

Declaration

I hereby declare that this submission is my own work and that, to the best of my knowledge and belief, it contains no material previously published or written by another person nor material which to a substantial extent has been accepted for the award of any other degree or diploma of the university or other institute of higher learning, except where due acknowledgment has been made in the text:

Signature

Name: Daniel Wellburn.....

Date: Friday 6th August 2010.....

Abstract

Laser surface modification applications such as transformation hardening, annealing, melting, alloying or cladding often require high levels of uniformity across the treated area in order to produce successful finishes. Problems arise when attempting to heat treat a surface uniformly with a moving circular heat source such as a laser beam. The circular geometry causes differences in interaction time across the width of the treated area. Surface heat treatment with a 2D moving heat source is explored using finite element modelling simulations involving heat transfer by conduction. Various fixed circularly-symmetric heat source intensity profiles are examined for their effectiveness in creating a uniform maximum temperature rise across the width of the treated area. The effect of changing the Péclet number is included in this investigation, highlighting an important problem in laser materials processing: the effectiveness of any one heat source intensity profile is limited to a short range of Péclet numbers, outside of which the temperature distribution pattern on the surface will no longer be suitable for the process the profile was designed for. A solution to this problem is presented in the form of creating a dynamic intensity profile which can be adjusted to accommodate for a range of processing conditions and materials. The dynamic profile consists of an annular ring with an added central intensity feature which can be varied to adjust for changes to the Péclet number. Three types of central intensity feature additions to the annular ring – Gaussian, holey-Gaussian and Plateau - are tested in a finite element model simulating a heat source moving over the surface of a material. A prototype refractive optical system based around a 'sombrero' lens is designed using simple lens formulae with the aim of successfully reproducing the annular ring with variable holey-Gaussian intensity feature. The prototype was built using zinc selenide components for use with a CO_2 laser. The beam profile modulation mechanism was tested by profiling the output intensity profile whilst changing the input beam magnification to vary the relative size of the

central intensity feature. Although the modulation mechanism in the design was proven to operate effectively the holey-Gaussian feature addition to the annular ring is shown to be ineffective in achieving high uniformities at higher Péclet numbers. An annular ring with a variable plateau intensity feature in the centre produced better uniformities over the range of Péclet numbers tested, particularly at the higher Péclet numbers. Geometrical ray tracing and the intensity law are used to develop a system of equations for a numerical method by which an optical system capable of producing an annular ring profile with a plateau fill feature in the centre can be designed for any laser system. Employing this method one such optical system is designed for use with a CO_2 laser. Modelling of the output intensity profile shows that as well as adjusting its relative size the shape of the plateau fill intensity feature is distorted when the input beam diameter is adjusted. The output intensity profile for various input beam diameters is tested for uniformity of heat treatment over a range of Péclet numbers in the finite element model. It is shown that the distortions produced are not detrimental to its performance.

Acknowledgements

The Author would like to express thanks to the following people for assistance during the course of completing this thesis:

To my PhD supervisors Professor Ken Watkins and Dr Geoff Dearden for the numerous helpful discussions, constructive criticism, guidance, enthusiasm and humour which made the experience not only relatively trouble free but also enjoyable.

To Dr Martin Sharp for discussions and ideas which had a major effect on the direction of the work presented in this thesis. Martin is recorded as co-inventor of the prototype optical system presented in Chapter 3 of this thesis for suggestions which led to the conception of the beam profile modulation mechanism.

To Nick Ellis of ULO Optics for advice on technical optics issues, help with ZEMAX and a great deal of patience.

To members of the direct write group particularly Dr Eamonn Fearon.

To Tony Jones for essential assistance provided in writing the macros required to numerically solve the lens surface equations.

To all the staff at Lairdside Laser Engineering Centre particularly Dr Stuart Edwardson and Doug Eckford for practical help of all kinds without which I would have been truly stranded.

To Emeritus Professor Bill Steen for some really helpful technical discussions and bags of enthusiastic encouragement.

To Professor John Dowden and Dr Nilinjan Chakraborty for the essential guidance they provided to bringing this thesis up to a publishable standard.

Finally to my family and friends who have been a constant source of support throughout. I really couldn't have made it through without you.

Table of Contents

Table of Figures

List of Abbreviations, Subscripts and Symbols

Abbreviations

FEM – Finite Element Method
TDP – Temperature distribution profile
FGAR – Full-Gaussian Annular Ring
OHGAR – Outer Half Gaussian Annular Ring
IHGAR – Inner Half Gaussian Annular Ring
BFD – Back Focal Distance

Subscripts

init -initial
max - maximum
o – relating to objective lens
s – relating to sombrero lens
IN – relating to input reference plane
AX – relating to central Axicon section of sombrero lens
PL – relating to plateau fill
HG – Relating to holey-Gaussian
AR – relating to annular ring
OUT/img – relating to image or output plane

Symbols

Symbol	Description	SI Units	Symbol	Description	SI Units
A	area	m^2	θ	angle	rad
c	speed of light	ms^{-1}	Q	heat source	J
c_p	specific heat capacity	$Jkg^{-1}K^{-1}$	q_0	input heat flux	K
f	lens focal length	m	r	radial distance	m
I_0	maximum intensity	Wm^{-2}	ρ	density	kgm^{-3}
k	thermal conductivity	$JK^{-1}m^{-1}s^{-1}$	R_0	characterstic beam radius	m
l	length	m	T	temperature	K
m	mass	kg	U	uniformity	-
n	unit normal vector	-	V	volume	m^3
n	refractive index	-	v	velocity	ms^{-1}
P	power	W	w_0	Gaussian peak width	m
Pe	Péclet number	-	z, Z, u, p, d	Distances along optical axis	m
ψ	dimensionless width	-	α	thermal diffusivity	m^2s^{-1}

1 Introduction

Lasers have proved to be a highly important tool in macro-scale materials processing. They are able to direct high amounts of energy in controlled amounts directly where it is needed. They eliminate the need for physical contact with the material and provide a chemically clean processing environment in which process monitoring and control is easily carried out. Lasers in macro-scale materials processing are used amongst other things for forming, cutting, welding, drilling and surface modification. Laser surface modification itself covers a number of different applications including laser surface melting, laser alloying, laser cladding, laser surface annealing and laser transformation hardening. Pyrolytic[a] laser surface treatments can be split into three categories: heating, melting and vaporisation depending on the temperatures reached in the material. The main benefit of surface treatments of these kinds is to allow the surface properties of bulk materials to be locally or globally altered without the need to treat the rest of the material. It can also permit cheaper materials to be used in place of more expensive materials as well as allowing completely novel or improved material functionality which may not be possible using other methods. Heating laser processes are of key interest to the findings in this thesis. Some melting processes are also relevant although these are limited to convection limited processes due to the methodology chosen in this thesis.

The majority of laser heating techniques involve fulfilling three criteria:

1. first, the material must be heated to a minimum prescribed temperature whilst taking care to ensure that a maximum allowed temperature is not exceeded;
2. second the material must be retained within that temperature band for a specified time period;
3. and third, (in some but not all cases) the rate at which the material cools from its elevated temperature must be controlled.

[a] those which involve heating of the surface

Though the nature of laser treatment is selective, it is usually a requirement for areas much wider than the diameter of the beam to be uniformly treated to ensure the integrity of the overall surface under specific conditions. For uniform treatment the laser must interact with the surface to ensure the aforementioned criteria are met for all areas on the surface. Care must also be taken to ensure that adjacent processed lines or tracks overlap sufficiently so as to eliminate any discontinuity in material properties across width of the treated surface. There are three main methods for ensuring uniformity of treatment across a wide area: shaping the beam geometry or the beam intensity profile; using a rapidly scanning beam; and/or carefully controlling the overlap between successive passes. Shaping the beam geometry and shaping the intensity profile have received notable attention in the literature [1-14]. Many of the papers remark on the effectiveness of a square, rectangular, strip or line shaped beam geometry for achieving a uniform treatment across the width of the treated area. Multi directional processes would not benefit from such geometries however as the direction of movement of the beam would affect the temperature distribution on the surface[15, 16]. The only geometry whose effect is independent of processing direction is a circle, provided that the intensity profile within the geometry is circularly symmetric. It is shown in the literature[17-20] that the Péclet number has a major effect on the surface temperature distribution caused by a moving laser beam. In this thesis, the effect of changing the Péclet number on the surface temperature distribution for various circularly symmetric fixed intensity profiles is recorded to highlight an important problem in laser surface processing – that an intensity profile optimised to provide a uniform treatment under one set of processing parameters for a given material will become ineffective if the process parameters, material or material properties are changed significantly. The only way in which the changes to the Péclet number can be accommodated is by allowing modulation of the intensity profile.

The aims of the research are now broken down into strategic objectives and the chosen tactical actions intended to complete these objectives. The first of these objectives is to achieve the first requirement of uniform heat treatment using a moving heat source (in this case a laser beam) with a circularly symmetric intensity profile for as wide an area as possible under the moving heat source. This will be

completed by exploring a range of intensity profiles over a range of Péclet numbers using a finite element heat conduction model. The second objective is to recreate the full range of intensity profiles required to satisfy the first objective using a single optical system. This will be completed by designing a refractive optical system and a mechanism for controlling the intensity profile in the desired manner.

Chapter 2 contains an investigation of the effect of different fixed intensity profiles on the surface temperature distribution and surmises that, in order to continue to achieve uniformity, the intensity profile must be modulated if the processing conditions or material properties change. Dynamic intensity profiles are those which can be modulated, by adjustment of the optics for example, to provide a smoothly changing intensity profile on the target plane. The performance of three different dynamic profiles is investigated over a range of Péclet numbers.

Chapter 3 discusses how geometrical methods in optics design can be used to develop refractive beam shaping systems which create and allow modulation of two of the dynamic profiles designed in Chapter 2. A prototype system is designed for use with a CO_2 laser using simple lens equations and is built and tested on a high powered CO_2 laser to provide proof of concept of the beam profile modulation mechanism. An optimised design is then presented and an example modelled for use with the same CO_2 laser the prototype is tested on. A step-by-step design method is provided to allow the same dynamic intensity profile to be recreated by others for other laser systems and the results are provided in dimensionless form to allow scaling of the technology.

Chapter 4 provides a summary of the key findings and discusses the limitations introduced in the choice of methodology in three key areas: in the approach to assessing and achieving uniformity; in modelling heat transfer by conduction only; and in the choice of the geometrical optics approximation used in the lens design. Key target areas for future work are also signposted.

2 Developing Dynamic Intensity Profiles for Uniform Surface Treatments

2.1 Introduction.

The purpose of this section is to provide insight into the effect of changing the intensity profile of a circular moving heat source on the temperature distribution on the surface of a material. The material properties, heat source radius and the traverse speed also have a major effect on the temperature distribution. The implications of this will be highlighted in a study of the variation in surface temperature distribution over a range of Péclet numbers for various heat source intensity profiles. It will be shown that no one circularly symmetric intensity profile is effective in creating a uniform temperature rise on the surface of a material over a wide range of Péclet numbers. A solution to this problem will be presented using a dynamic intensity profile which is modulated to adjust for different Péclet numbers. Three dynamic intensity profile designs are analysed for their effectiveness over a range of Péclet numbers relevant to the target applications.

2.1.1 Laser Radiation

LASER stands for light amplification by the stimulated emission of radiation. In a laser the lasing medium produces the light amplification and can be solid, liquid, gas or plasma. The lasing material is made to 'lase' by pumping it full of energy to force electrons to become excited and make the transition into higher energy levels. Once the return transitions are made to lower energy levels, photons of light are emitted. The laser cavity contains the lasing medium and the cavity mirrors which oscillate the light and select the laser beam structure or mode. The laser beam has a unique combination of properties compared with other forms of light. Its waves are monochromatic and spatially coherent and the brightness is generally very high due to the rate of photon emission in the lasing medium. The beam also has a low divergence over a very long range. This creates a very powerful form of light –a laser beam allows the delivery a very intense form of in-phase energy wave directly to where it is needed even if that is some distance from the laser output window itself. Although the laser light can be delivered in very high peak-power pulses, this research

treats the laser beam as a continuous wave with no time dependent intensity fluctuations.

2.1.2 Laser-Material Interaction

When a laser beam strikes a surface some of the incident beam is reflected by the material some is absorbed by the material and some is transmitted through the material. The proportion of each is determined by both the properties of the material and by the properties of the incident beam.

The electromagnetic radiation is split into magnetic and electric field vectors. The electric field will cause an electric force on the charged particles in the surface and assuming that the frequency of the wave is not closely matched to the resonant frequency of the particles, a forced vibration of the charged particle is set up. Since the positively charged particles (the atomic nuclei) are too large to be affected by the relatively small electric force, it is the free and bound electrons in the surface which absorb the energy of the incident wave.

If the free electrons absorb the incident wave, they vibrate then reradiate photons in all directions when they lose the energy shortly afterwards. This can lead to reflection of light from the surface or, if the photons are reabsorbed by other free electrons deeper in the material, the light be transmitted through the material in the same way. If the bound electrons absorb the energy their vibration will be restrained by the lattice phonons[b]. This can cause the structure to vibrate thus leading to the generation of heat within the surface.

For transparent materials the proportion of absorbed radiation, the absorptivity A, is given in terms of the proportion of transmitted radiation, or transmissivity T, and the proportion of reflected radiation, or reflectivity R:

$$A = 1 - (T + R) \qquad [1]$$

[b] Lattice phonons are the quantum modes of vibration of the lattice

The target applications for the research conducted in this thesis all involve opaque materials, therefore any discussion of the mechanisms or factors affecting the transmissivity will end here. For opaque materials the transmissivity term disappears giving:

$$A = 1 - R \qquad [2]$$

The reflectivity R is given in terms of the material extinction coefficient κ and the refractive index n of the material. n is related to the velocity of light in the medium and κ is related to the decay.

$$R = \frac{(n-1)^2 + \kappa^2}{(n+1)^2 + \kappa^2} \qquad [3]$$

Drude theory[21] provides amendments to this formula to take account of both the polarisation of light and the angle of incidence of the beam. For p-polarised beams (those polarised parallel to the plane of incidence of the ray) the reflectivity is given by R_P below, for s-polarised beams (those polarised perpendicular to the plane of incidence) the reflectivity is given by R_S below:

$$R_P = \frac{(n - 1/\cos\theta)^2 + \kappa^2}{(n + 1/\cos\theta)^2 + \kappa^2} \qquad [4]$$

$$R_S = \frac{(n - \cos\theta)^2 + \kappa^2}{(n + \cos\theta)^2 + \kappa^2} \qquad [5]$$

Other factors which affect the reflectance of the material are the wavelength, the temperature and surface roughness of the material and the presence of any thin films or oxidation on the surface. Shorter wavelengths are absorbed more easily as the more energetic photons are absorbed by a greater number of bound electrons. At increased temperatures the phonon population increases and there is a greater chance that the electrons will interact with the structure rather than reradiate therefore in most materials absorptivity increases with increasing temperature. If a surface film is applied with a thickness of $[(2n+1)/4]\lambda$ then interference coupling can

occur leading to greater absorptivity. If the roughness of a surface is greater than the wavelength then multiple reflections within the undulations can also lead to greater absorptivity.

The attenuation of the absorbed wave through the depth of the material is given by the Beer-Lambert law[21] which describes the amplitude of the electric field at a depth $E(z)$ as a function of the field amplitude at the surface E_0, the extinction co-efficient κ, and the wavelength of the light λ:

$$E(z) = E_0 e^{-\frac{2\pi\kappa z}{\lambda}} \quad [6]$$

The intensity is the square of the field amplitude therefore the intensity $I(z)$ at a given depth as a function of the intensity at the surface is:

$$I(z) = I_0 e^{-\frac{4\pi\kappa z}{\lambda}} \quad [7]$$

The absorption depth is given as the depth at which the absorption drops to I_0/e. In most laser surface treatments absorption depths are very low compared with the characteristic width of the beam, often the absorption depths are just a few atomic layers. Assuming that the optical effects are linear - that the amount of heating is roughly proportional to the intensity of the beam - the absorbed laser beam can be approximated as a 2D heat source on the surface of a material with an intensity profile resembling that of the incident beam.

2.1.3 Laser Surface Heat Treatment

The aims of the research conducted in this thesis are to investigate laser beam intensity profiles for processes where uniformity of treatment is important. These processes can be split into heating processes such as laser transformation hardening and laser surface annealing and melting processes such as laser surface melting, laser surface alloying and laser cladding. A summary of each of these processes follows with a brief review of the literature to highlight the variety of applications which may benefit from uniform surface heat treatment.

2.1.3.1 Laser Transformation Hardening

Laser transformation hardening involves heating the surface of a bulk material to the Austenite region without causing surface melting. The heating process must be sufficiently slow as to allow conduction of the heat to the required depth. The bulk of the material acts as a heat sink and allows the fast quenching required for Martensite formation without the use of an external quenchant such as oil or water. Martensite has much improved hardness and wear properties compared with those of the bulk material. The Martensite microstructure formed by laser heating is finer than that formed by other heating methods (flames, arcs or induction) due to faster quenching. Applications of laser transformation hardening include hardening of tool steels[22-25] and engine valves[26, 27], controlling chip formation in the turning of tool steels[28], the prevention of burr formation in the face milling of carbon steel[29] and improving the tribological properties and hence the service life of various mechanical and automotive components[30].

2.1.3.2 Laser Surface Annealing

Laser surface annealing involves heating of non-metal (usually semi-conductor) materials in order to facilitate bulk diffusion or recrystallisation at the surface. For example laser annealing of silicon-on-sapphire films has been carried out to relieve the stresses created in the film deposition process[31]. Heating of the amorphous silicon layer allowed relaxing of the lattice which caused crystallisation due to the effect of residual stresses from the sapphire beneath. CO_2 laser annealing of amorphous PZT (piezoelectric transducer) films deposited using metal-organic decomposition produced thick and thin films with greatly improved ferro-electric properties [32-34]. Stultz[35] reports large grain sizes obtained by using a modified beam shape to illicit polycrystallisation of an amorphous silicon substrate. Polycrystalline silicon substrates are of high value in modern electronics applications including flat-panel displays, mobile phones and logical integrated circuits[36].

2.1.3.3 Laser Surface Melting

If the laser heats the surface beyond its melting point a melt pool will form which will re-solidify once the heat is quenched by the surrounding material. The melting and re-solidification of a material can cause marked changes in the material properties. Marangoni forces caused by the high temperature gradients on the surface cause mixing and homogenisation of the material inside the melt pool. The final microstructure of the material depends on the ratio of the temperature gradient to the solidification rate[37]. Laser surface melting has been used for numerous applications including densification of ceramic substrates[38], improving the tensile strength, wear and corrosion properties of tool[39-43] and stainless[44-46] steels, improving the hardness[47, 48] and erosion resistance[49] of cast iron, improving the corrosion and pitting properties of bio-implants[50] and polishing of silica micro optical components[51].

2.1.3.4 Laser Surface Alloying

In addition to changing the microstructure of the surface, the composition of the surface of a bulk material can be altered by adding new materials to the melt pool. Just as in laser surface melting, the Marangoni forces facilitate mixing to create a homogenous surface composition. The addition of the new material(s) can be accomplished by several means including thin foil application[52, 53], electroplating[54, 55], reactive gas shroud[56-59], powder feed[60-63], preplaced powder[64-66] and plasma spray[67, 68]. Applications of laser surface alloying include: improving the tribological properties of Ti and Ti6Al4V by creating a TiN surface layer[56, 69]; creation of a stainless steel layer to improve corrosion resistance of carbon steel[70]; hardening of mild steel[71], aluminium[72] and stainless steel[73]; and improving the tribological properties of alumina[74] for non-lubricated sliding contacts such as those used in space.

2.1.3.5 Laser Cladding

Where an entirely different material from the bulk is required for the surface layer, laser melting and laser alloying are not sufficient due to inclusion of all or some of the bulk material in the layer. Laser cladding allows the addition of a layer of material

which may be completely different from the bulk material. The material is added in the form of a preplaced powder, a powder stream blown directly into the melt pool or in the form of a feed wire and is fused to the bulk material by melting and re-solidification. Laser cladding can be used as a surface modification technique or to build 3D components in a layer by layer deposition process. Applications of laser cladding include forming of a protective layer on the surface of turbine blades for improved corrosion and wear resistance [75-78], repair of large engine components[79] and improvements in the wear resistance of a variety of metals and alloys[80-86].

2.1.3.6 Other Laser Surface Treatments

There are a number of lesser known laser surface treatments in existence. For example Osvey et al[87] and Kepiro et al[88] report the removal of small surface defects from porcelain china by heating with a CO_2 laser after the firing process. Sato et al[89] discuss a laser curing process based on heating of silver particulate loaded polymeric inks deposited directly onto substrates for direct write of circuitry and electrical components. The process relies on conduction of heat through the ink film to the substrate to cross-link a polymer matrix and evaporate solvents. Target applications for this technique include the fabrication of flexible electronics for the lighting and displays industry and direct write of circuitry in the manufacturing and aerospace industries.

2.1.3.7 Mechanisms and Uniformity in Laser Surface Heat Treatments

In order for the laser to bring about the desired change in the surface of a material, the thermal history of the workpiece surface must follow a prescribed pattern. For example Davis et al[90] provide an outline of the thermal history required for surface hardening of metals. The material must reach the A_3 temperature (at which Austenite is formed), it must then remain at or above this temperature (whilst not exceeding the melting temperature) for long enough to allow carbon diffusion to take place. The material must then be quenched sufficiently quickly as to allow the formation of Martensite.

To achieve true uniformity in the finished surface properties after heat treatment, each point across and at the desired depth below the surface of the material must experience the prescribed thermal history. The strategic objectives of this research are to attempt to achieve true uniformity in the thermal history experienced by the surface. The tactics employed will be to address the primary requirement outlined by Davis et al[90]: that the material reach a desired minimum temperature (for example the A_3 temperature) without being raised above a maximum temperature (for example the melting temperature). This will be the initial target which will drive the design of the intensity profiles in this chapter. The secondary and tertiary requirements - that the material remain within the temperature window for a sufficient time period and that the material then be quenched sufficiently rapidly – will be considered after the primary objective has been achieved. It is expected that control of all three requirements simultaneously will not be possible due to the circular shape of the moving beam. However, it may be possible to control them practice using other methods in combination with shaping the shaping the intensity profile, such as varying the traverse speed or increasing the total laser power. It may be possible to ensure uniformity in the finished surface properties[c] by ensuring that all points across the width and below a specified depth beneath the surface of the treated area still fulfil the thermal history requirements despite not experiencing exactly identical thermal treatment. This would only be possible however if there are sufficiently wide tolerances in processing parameters. A study into whether this is actually possible is beyond the scope of this thesis.

2.1.3.8 Parametric Target Window

Ion, Shercliff and Ashby[91] produced parametric processing charts for a number of different CO_2 laser heat treatment processes by extracting data on the processing parameters from a large amount of existing literature. They use two dimensionless parameters: the dimensionless laser power P^* which links the actual laser power P, the absorptivity A of the material, the thermal conductivity k and the initial T_0 and melt T_m temperatures; and the dimensionless traverse speed v^* (referred to later on

[c] Within acceptable tolerance levels

as the Péclet number *Pe*) which links the traverse speed *v*, the characteristic beam radius R_0 and the thermal diffusivity α.

$$P^* = \frac{AP}{R_0 k(T_m - T_0)} \quad [8]$$

$$v^* = Pe = \frac{vR_0}{\alpha} \quad [9]$$

These dimensionless parameters are plotted against each other to show the operating regions on a processing diagram for a range of laser surface heat treatments. The chart is shown below in Figure 1 and is taken directly from Ion et al's paper[91]. Many of the surface heat treatments included in this chart are relevant to this thesis such as those introduced in the previous sections (2.1.3.1 to 2.1.3.5) but there are some, such as those involving vaporisation and those involving melting where convection is a significant factor in determining the temperature distribution, which this body of research has not been far reaching enough to cover.

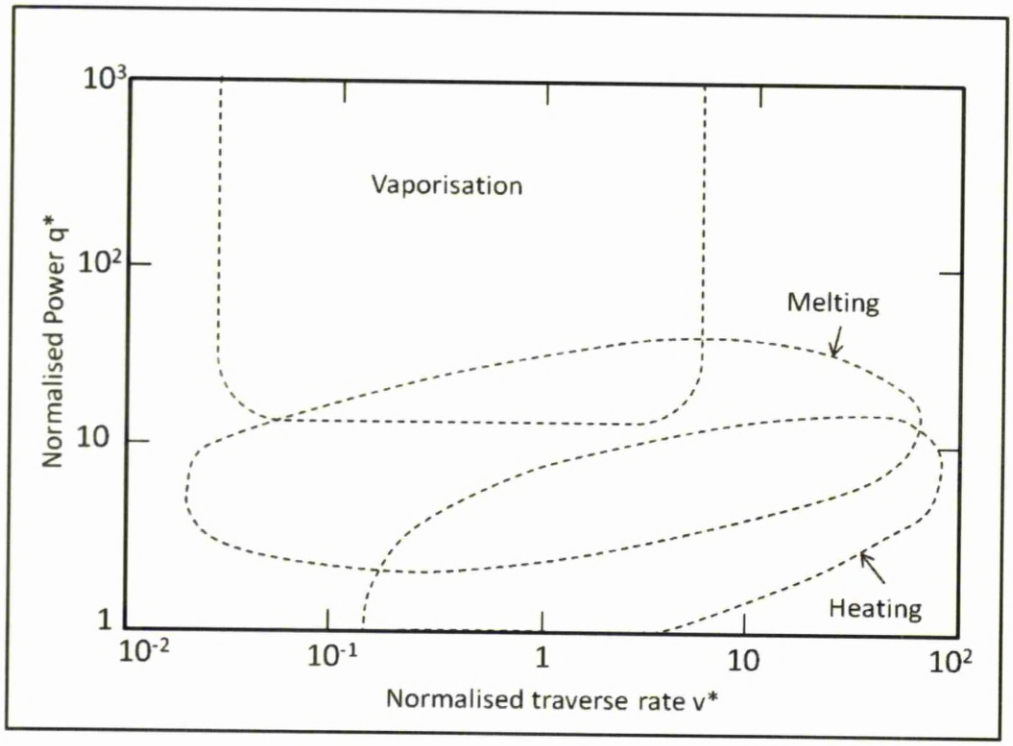

Figure 1: Dimensionless parameter sets/operating conditions for different laser surface heat treatments from Ion et al's 1991 paper. Broken lines represent practical operating regions taken from their reviewed literature [91]

2.1.4 Heat Transfer Modelling

Prediction of the temperature field created by a laser beam moving over the surface of a material is essential for understanding of many laser surface heat treatments. There are several methods for calculating the temperature field. Analytical methods were first published by Rosenthal[92] who modelled the temperature field created by moving point and line sources to simulate surface melt runs for conduction welding. A collection of Rosenthal's and other solutions can be found in Carslaw and Jaegers book *Conduction of Heat in Solids*[93]. Christensen et al[94] reproduced Rosenthal's work using dimensionless numbers to provide a more generalised and useful solution, enabling it to be applied to a much wider range of welding process parameters and materials. The method predicted the temperature accurately for areas far from the source but the infinite temperatures created at the location of the source proved troublesome for calculating temperatures close to the source. Improvements to the

analytical method were brought about by Eagar and Tsai[95] who were the first to solve the heat transfer equation for a moving 2D heat source on a semi infinite plate. They used superposition of point sources solutions to simulate a moving Gaussian heat source intensity profile and generalised their solution by expressing it in dimensionless form.

Other methods for solving the heat transfer partial differential equations are numerical. One such method is the finite element method.

2.1.4.1 Finite Element Method

The Finite Element Method (FEM) is applied to calculate solutions to partial differential equations (PDEs) in order to calculate unknown variables across a domain. FEM was first developed in 1943 by Richard Courant for vibration systems using results for PDEs previously obtained by Rayleigh, Ritz and Galerkin. FEM works on the basis that any domain can be split up into smaller regions know as finite elements using a process called discretisation. Points of contact between the elements are known as nodes and it is their distribution which dictates the shape of the elements themselves. It is a requirement of FEM that the solution be continuous across each common boundary between the elements. Once the position of the nodes is established a differential equation can now be applied to each single element. An approximate solution to the distribution of the unknown variable (e.g. temperature, displacement or stress) across the individual element domain is then given as a continuous function comprised of discrete values of the variable at each node. A system of simultaneous equations is constructed for each element in terms of unknown nodal values. The unknown nodal values are then solved using either linear algebra or non-linear numerical schemes and a description of the change of value of the unknown variable across the whole domain is given in terms of the individual values at the nodes.

2.1.4.2 Finite Element Modelling

Finite Element Modelling is a computer simulation technique that employs FEM. Commercial development of FEM software began in the mid 1950's for the purpose of structural analysis. Today FEM software is used to investigate almost any physical phenomenon from fluid mechanics[96] to black holes[97]. It is most widely used in aerospace, automotive and civil engineering sectors which often require solutions to unusual problems or in complex geometries. Examples of FEM software currently used in industry are ABAQUS, ANSYS, NASTRAN and ALGOR.

2.1.4.3 COMSOL Multiphysics FEM software

COMSOL Multiphysics[98] is a finite element modelling package which allows multiple, co-dependent physical phenomena, for example electrical resistance and temperature, to be simulated. It is experiencing growing use in research - to date there are over 350 published papers[d] reporting its use in many diverse areas, from fluid mechanics simulation for retinal surgery[99] to design of shear tensors in robotic hands[100]. Studies directly relevant to this thesis can also be found in the literature. Bianco, Manca and Ricci[101] studied the opto-thermal fields generated within a thin film structure by a moving laser heat source and reported the transient temperature field at various Péclet numbers. In a separate paper Bianco et al[102] reported the temperature field in a 3D semi-infinite solid created by a moving Gaussian laser beam. The results at various Biot and Péclet numbers are reported. In the case of this research, COMSOL Multiphysics[98] is used in an identical way to Bianco et al[102] to simulate the heat transfer by conduction through a semi infinite 3D solid caused by a 2D heat source moving across its top surface. There are no co-dependent phenomena involved and as such any standard FEM software would have also been suitable and could be used by anyone wishing to replicate or extend this body of work.

[d] Web search for papers using COMSOL carried out January 2010

2.1.5 Heat Flow Theory

Heat transfer can occur via any of the following mechanisms: convection, radiation and conduction. Below the melting temperature, heat transfer within a solid takes place solely by conduction. Above the melting temperature, heat transfer can take place via conduction and convection due to flow of material inside the melt pool. At low Prandlt Numbers heat transfer is dominated by conduction[103, 104]. Heat transfer by convection is not considered in this thesis and as such the research contained here is limited to laser surface heating processes and laser melting processes in the low Prandlt Number range[103, 104].

When considering heat conduction through a material, certain properties must be considered. The properties of interest are the thermal conductivity k the density ρ and the specific heat capacity c_p which are given by the following equations:

$$c_p = \frac{Q}{m\Delta T} \quad [10]$$

$$k \sim \frac{Ql}{A\Delta T\Delta t} \quad [11]$$

$$\rho = \frac{m}{V} \quad [12]$$

These properties combine to give the thermal diffusivity α (sometimes denoted by κ, D or k) where:

$$\alpha = \frac{k}{\rho c_p} \quad [13]$$

α is generally temperature dependent since c_p; ρ and k are temperature dependent to some extent in most materials. The principle of conservation of thermal energy can be used to derive the partial differential equation whose solution allows the temperature distribution within a material to be calculated.

The principle of conservation of energy can be expressed as follows:

The net rate of increase of thermal energy within a volume V is equal to the net rate of generation of thermal energy within V and on surface S minus the net flow of thermal energy through the surface S.

This statement gives rise to the partial differential equation whose solution gives the time dependent temperature distribution in any solid monolithic workpiece:

$$\rho c_p \frac{\partial T}{\partial t} + \rho c_p \boldsymbol{v}.\nabla T = \nabla.k\nabla \mathrm{T} + \mathrm{q} \qquad [14]$$

The first term on the left hand side of equation [14] is the total rate of increase of thermal energy per unit volume. The second term on the left hand side takes account of the contribution to the flow of heat through surface S by the movement of the material relative to the heat source q. The first term on the right hand side is the second contribution to the flow of heat through S and is derived from Fourier's law which states that the rate of flow perpendicular to the surface is proportional to the negative of the temperature gradient.

The term q describes a heat source or sink. A full derivation of equation [14] can be found in reference [105].

The time dependent relative temperature distribution pattern[e] (or time dependent relative ΔTDP) due to a moving heat source within a given monolithic workpiece is governed by α, the traverse speed v, characteristic size R_0 and the outline shape and intensity profile of the heat source. If the relative intensity profiles of any two moving heat sources are the same, the relative ΔTDP in a given material is determined by the Péclet number Pe.

$$Pe = \frac{vR_0}{\alpha} \qquad [15]$$

The Péclet number is therefore high for conduction limited processes – those where the thermal diffusivity is low, the traverse speed is high or the heat source is large –

[e] That is: the dimensionless or normalised temperature increase distribution

and low for highly conductive processes. It should be noted at this point that the Péclet number does not determine the absolute temperature values only the relative temperature distribution within the workpiece.

The Péclet number used in this context is different to that commonly used in conventional convective heat transfer. In conventional convective heat transfer, the Péclet number is the product of the Reynolds number *Re* and the Prandlt Number *Pr* and represents the ratio of the heat convected to the fluid and the heat conducted within the fluid. As heat transfer by convection is not considered in this body of work, the Péclet number as used in the context of this thesis takes a different meaning: it is the ratio of the heat generated within the solid by the moving heat source to the heat conducted within the solid.

2.2 Modelling Set Up

2.2.1 General Assumptions and Approximations

Approximations and assumptions are an important part of the modelling process. Any approximations and assumptions drawn into the model must be well thought out and justified however. A well thought out and reasonable assumption or approximation can save a lot of unnecessary modelling time, whereas an incorrect one may cause results to become warped at best or totally misleading and inaccurate at worst.

The model considers the heat transfer by conduction through an isotropic solid with no phase changes in the material. It should be noted that although c_p, ρ and k are generally temperature dependent, the model used in this thesis assumes that they are temperature independent for simplicity. The temperature dependence of the thermal conductivity for example is well documented for many materials [106-109] – each material behaving differently to the next. Therefore any specific study involving a material with its own temperature dependent material properties will only serve applications using the material and will distract from the main goals of this body of work. That is not to say that these factors are not important – they are important when considering specific situations – just that they won't form part of the investigations for the purposes of obtaining generalised results.

It is important at this point to stress the additional limitations which are brought about by the choice of methodology employed in this thesis. The finite element model simulations do not consider melting and therefore do not take into account the contribution to the temperature field brought about by the latent heat of melting or by convection effects. This limits the relevance of the results obtained to laser heating processes such as laser transformation hardening and laser surface annealing. The results may still hold some relevance however for some melting processes, specifically those melting processes where heat transfer by convection is limited. Chakraborty and Chakraborty[103] have classified such cases as occurring in the case of materials with characteristically low Prandtl numbers so long as the Reynolds number remains below certain limits. The Prandlt number *Pr* is the ratio of the kinematic viscosity v and the thermal diffusion α and the Reynolds number *Re* is the ratio of inertial forces ($\rho v^2 R_0^2$) to viscous forces ($\mu v R_0$):

$$Pr = \frac{v}{\alpha} \qquad [16]$$

$$Re = \frac{2\rho v R_0}{\mu} \qquad [17]$$

Therefore for materials with low Prandlt numbers, such as many of the molten metals in laser surface treatments, thermal diffusion should dominate and thus convection effects need not be considered when attempting to model the melt pool geometry. However it has been shown[110-114] that in a number of laser melting processes, convection effects are significant in determining the melt pool characteristics and therefore cannot be ignored in these instances. Chakraborty and Chakraborty[103] show however that so long as the Reynolds number remains below a certain transitional value, then heat transfer is dominated by conduction. The regime diagram they constructed was later updated by Chakraborty in subsequent paper. The diagram plots the Prandlt number against $Ch^2$where *Ch* is a dimensionless number given by:

$$Ch = \left[\frac{\mu}{\rho \left| \frac{\partial \sigma_{sur}}{\partial T} \right| \left(\frac{1}{\mu} \frac{P_{abs}}{\pi k} \right)} \right]^{\frac{1}{3}} \quad [18]$$

Where P_{abs} is the absorbed power in the surface and σ_{sur} is the coefficient of surface tension on the melt pool surface.

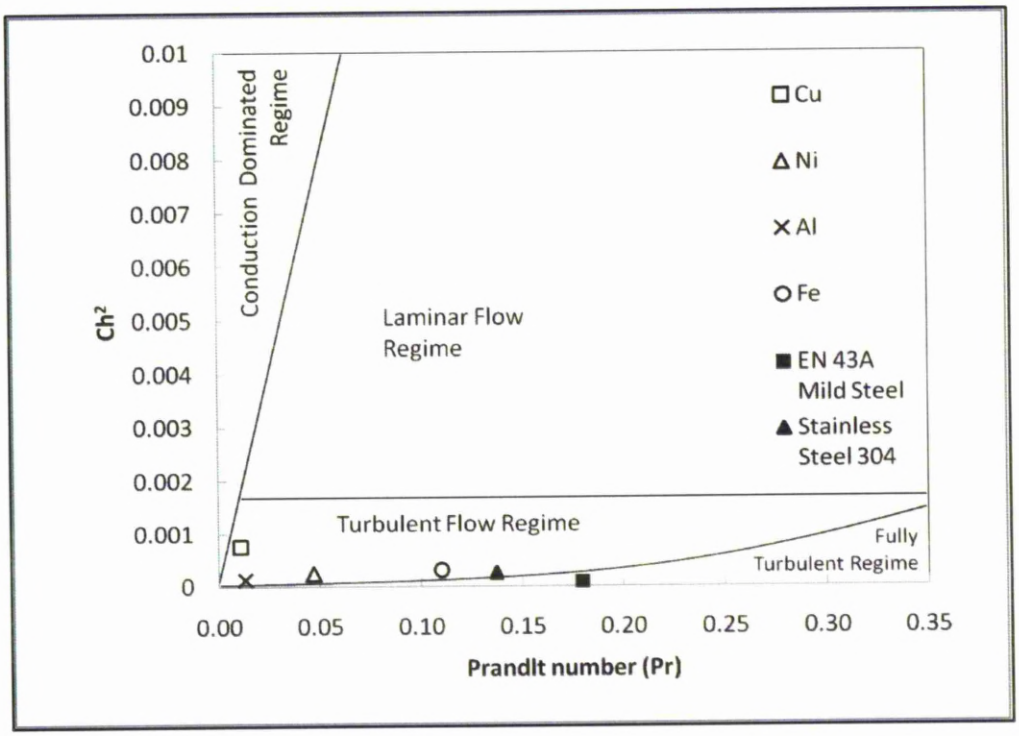

Figure 2: Regime diagram by Chakraborty[104] annotated with laser melting examples from the literature[9, 114-116]. This diagram was constructed based on a melt pool aspect ratio (depth/width) of 1/3.

Chakraborty and Chakraborty[103] concluded that for very low Prandlt number there only needs to be a very small drop in Ch^2 for the regime to change from one where conduction dominates directly to a fully turbulent regime where convection effects are highly significant. In a separate paper, Chakraborty[104] validates this regime diagram in finite element simulations of laser welding. Two metals were used - Fe (Pr=0.1) and Cu (Pr=0.01) - and each were modelled considering both conduction and convection effects and again by considering conduction effects only. It was shown

that the solutions obtained between the two conduction/convection models and the conduction only model were vastly different for Fe but not for Cu.

The data used to plot the examples shown in Figure 2 was taken from Sarkar et al[114] (Al and Fe), Chakraborty[115] (Cu and Ni), Han and Liou[116] (stainless steel 304) and Safdar et al[9] (mild steel EN 43A). Refractory ceramics data was also captured from Li et al[117] but appeared far outside the limits of Figure 2 ($Pr=1.73$, $Ch^2=0.003$) and solidly in the laminar flow regime. Figure 2 highlights the limits of the research conducted in this thesis with respect to melting processes. In only considering heat transfer by conduction, the majority of the melting processes in the literature will not be properly predicted in the simulations carried out herein. Al, Fe, Ni, mild steel EN 43A, and stainless steel 304 are all in either the turbulent flow or fully-turbulent regimes. This implies that convection plays a non negligible part in heat transfer in laser melting processes involving these materials. Cu is close to the conduction dominated regime however and therefore the research carried out herein may have some applicability in laser melting processes for such materials. An additional caveat is that since the latent heat of melting is not included in the analysis; this will also affect the validity of the results for any laser melting regardless of which regime it falls in Figure 2.

Heat transfer by convection and radiation from the surface is considered in the model, however the effect of altering them does not form any part of the investigations carried out in this thesis. A surface emissivity of 1 will be used for surface radiation calculations with a heat transfer coefficient of 10 W/m^2K being used for surface to air convection calculations. A surface emissivity of 1 implies the material will be treated as a blackbody. The choice of an emissivity of 1 in this case means that the laser reflection coefficient need not be used when considering absorbed laser power and the resultant maximum (laser) heat source intensities. In practice however no real material in this context ever acts as a blackbody – generally emissivities are less than unity but are also heavily material and surface dependent. Choosing the emissivity in this case to match a specific material would not hold any more (or less) relevance for

other materials[f] than a setting the material as a black body. However, it is could still be argued that a surface emissivity of less than unity would have been more realistic. The penetration depth of the laser radiation into the material for many of the target applications is generally order(s) of magnitude less[g] than the width of the beam (usually only a few atomic layers) which allows a 2D approximation for the heat source. Absorption coefficients and any burn-off characteristics are ignored as these are also often application or material specific. As the purposes of the investigations of this thesis are to report relative temperature differences, the absolute temperatures and laser powers are not reported. The research lays the basis on which to engineer solutions to specific applications by varying other parameters not investigated in this research. For example the research will report a method by which to control the uniformity in the maximum temperature reached across the width of the treated area – it will be left up to the applications engineer to adjust the laser power to achieve the required absolute temperature increase.

2.2.2 Model Preparation and Modelling Process

Using COMSOL[98] the modelling process can be broken down into a sequence of stages. The following list describes each stage and explains how it is carried out. A brief discussion about the caveats for each stage in general is followed by a more in depth discussion about the steps taken at each stage in this research to ensure the model is accurate and valid.

2.2.2.1 Drawing the geometry

Geometries will form the basis on which the model is built – each of the proceeding stages is impossible to carry out without a geometry in place. The geometry is constructed by specifying points, lines and shapes in 3D space and by extruding and/or revolving these entities to create 3D structures. General considerations for drawing the geometry are:

[f] Save for materials with similar emissivities

[g] This is true for opaque solid materials in which evaporation does not occur – generally in these cases the penetration depth is of the order of a few atomic layers.

- 'Matching up' pairs of surfaces if they are in physical contact. This ensures that conduction of heat between the surfaces is permitted
- Segmenting the geometry both where different materials exist and where different mesh sizes will be needed. This allows regions to be given different material properties and mesh sizes where appropriate
- Ensuring accuracy in dimensions and in the level of detail particularly in areas of interest
- Ensuring values entered are units congruent with the units used by the program (SI units)

Specific considerations when drawing the geometry for the purposes of this research are:

- Ensuring the geometry is sufficiently segmented as to allow enough reference points, lines, planes or subdomains to specify tighter meshing of areas where the heat source passes over and looser meshing of areas of lesser interest such as those far from the moving heat source
- Ensuring the semi infinite block is large enough to be considered semi infinite

A method of testing whether the geometry can be considered semi-infinite in this case is to choose a point three times the radius of the heat source away from its axis of movement, running the model at the lowest Péclet Number to be used in the investigation, then increasing the overall block width by the radius of the heat source until a difference of no more than 0.5 % in the temperature reached at this point is obtained. In this case this occurred when the width of block was extended to 5 times the radius of the heat source.

The geometry used for this research is shown in Figure 3. Notice the upper central area (the blue section) – this was created not for specifying a different material but to be able to refine the mesh in this area. The heat source will move along the top of this section in a straight line parallel to its edges from left to right in the picture. Its width is set at 1.5 times that of the heat source.

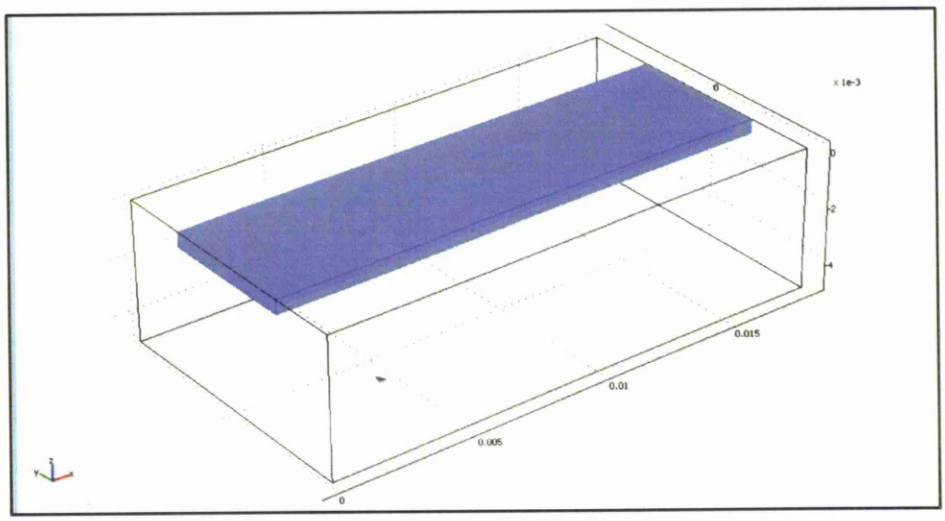

Figure 3: Drawing of geometry – semi infinite block used for heat transfer analysis of moving heat sources.

2.2.2.2 Defining the Physics

In a 3D geometry physical properties can be set on 4 different levels:

- Point: 1D points can be used as point sources and/or to fix the value of a variable at a point
- Edge: 2D edges can be used as line sources and/or to fix the value of a variable at an edge
- Boundary: 2D planes can be used to generate 2D sources on to, set boundary conditions and/or to fix the value of a variable at a boundary
- Subdomain: 3D parts can be used to generate 3D sources within and/or to set intrinsic material properties relevant to the type of modelling being carried out (e.g. thermal properties for heat transfer modelling, electrical properties for electro-magnetic modelling etc)

General considerations of setting physical properties are:

- Ensuring values entered are units congruent with the units used by the program (SI units) and that all physical properties specified in the governing equations are entered

- Ensuring all boundary conditions are considered and properly specified
- Ensuring any anisotropies in material properties are accounted for
- Ensuring any assumptions or approximations made about the conditions at any point, edge, boundary or subdomain are justified

In this research the model was running in the 'general heat transfer - 3D mode' and was limited to considering heat transfer by conduction only since this research is only interested in heat sources moving across the surface of solids and not liquids. Heat transfer by convection would have had to be added into the model if liquids were being investigated. The model was run in time dependent mode as opposed to stationary mode to allow analysis of the transient temperature distribution.

The partial differential equation used for heat transfer by conduction through the material is given by equation [14]

For heat transfer by conduction across a boundary COMSOL[98] can issue one of two conditions:

1. Heat Flux – Heat flux across a boundary is governed by the following equation

$$-\mathbf{n} \cdot (-k\nabla T) = q + h(T_{inf} - T) + \varepsilon\sigma(T_{amb}^4 - T^4) \qquad [19]$$

This takes into account:

a. The total heat flux across the boundary normal to the surface where the normal vector **n** is orientated out of (rather than into) the surface. This is given by the term on LHS of the equation.
b. Heat flux entering the domain such as that from some external heat source or from some external heat sink described by the first term on the RHS (right hand side of the equation) - q
c. Convection of heat to the surrounding environment (2nd term on RHS) where h is the heat transfer coefficient and T_{inf} is the ambient bulk temperature

d. Radiation of heat to the surrounding environment (3rd term on RHS) where T_{amb} is the temperature of the surrounding radiation environment, σ is the Stefan Boltzmann constant and ε is the surface emissivity.

2. Insulation – Insulation specifies the heat transfer as zero and is governed by the following equation

$$-\mathbf{n}.(-k\nabla T) = 0 \qquad [20]$$

3. Prescribed Temperature – the boundary is maintained at a prescribed temperature
4. Axial symmetry – the boundary considered as an internal boundary along the plane of symmetry of a full geometry.

In this model the all external boundaries of the semi infinite block were set as per the heat flux condition given in equation [19].

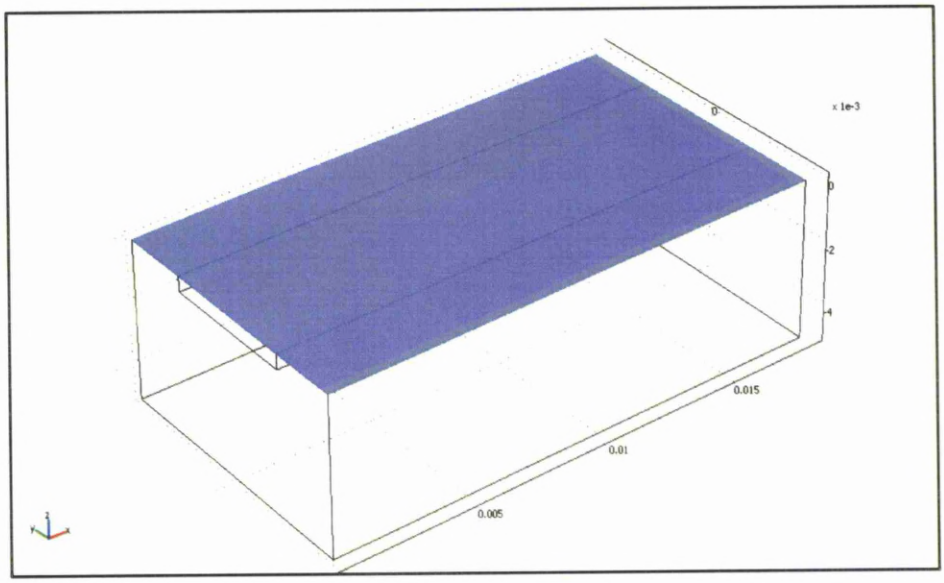

Figure 4: Highlighted top surface of semi infinite block

The blue top surface as shown in Figure 4 was given an input heat flux q in the form of a heat source described by a mathematical function, for example that of a Gaussian heat intensity profile which is described by:

$$q = \mathrm{I(r)} = \mathrm{I_0 exp}\left(\frac{-2r^2}{w_0^2}\right) \quad [21]$$

Where I_0 is the intensity maximum, w_0 is the radius at which the intensity drops to $1/e^2$ of I_0 and r is the radial coordinate given by:

$$r = \sqrt{(x - x_0)^2 + (y - y_0)^2} \quad [22]$$

The movement of the heat source is enabled by the variables x_0 and y_0 which are the co-ordinates of the centre of the heat source after a time t has elapsed:

$$x_0 = x_{initial} + v_x t \quad [23]$$

$$y_0 = y_{initial} + v_y t \quad [24]$$

v_x and v_y represent the components of the heat source traverse velocity in the x and y direction respectively and the initial co-ordinates $x_{initial}$ and $y_{initial}$ are the initial position of the centre of the heat source which were specified at twice the radius of the heat source from the first edge parallel to the y axis on the top surface of the block. All other heat sources are modelled as moving heat sources using the same technique but with different functions describing $I(r)$.

2.2.2.3 Meshing

Since the program works using finite element analysis, any model must be split into finite elements using a mesh. A mesh is a matrix of tetrahedra[h] which the solid is split

[h] In other modelling programs such as ABAQUS, the mesh consists of cuboids but the principle is the same.

up into. Using tetrahedral mesh elements is the default mesh element shape used by COMSOL[98]. This is possibly a deliberate effort made by the software designers to ensure that complex geometries can be easily accommodated without the user having to change the mesh element shape from a more basic construction such as the cuboid shape used by other simpler programs such as ABAQUS. For geometry as simple as the type used in this thesis, simpler mesh geometry such as that used by ABAQUS would have been more than sufficient. However the use of the default tetrahedral mesh element shape posed no real disadvantage in model solution time and is not inferior to the cuboid mesh element shape in terms of the resolution or accuracy of the output solution. For these reasons the mesh was not changed from its default shape of tetrahedral.

The density of mesh elements governs the resolution of the solution. Some areas of the model may require a tighter mesh (smaller node spacing) than others. This is usually due to areas being of greater interest or of finer detail compared with other areas. In this case the mesh size underneath the moving heat source was set at 1% of the overall width of the semi-infinite block. The difference in mesh sizes in the semi infinite block used in this research is illustrated in Figure 5.

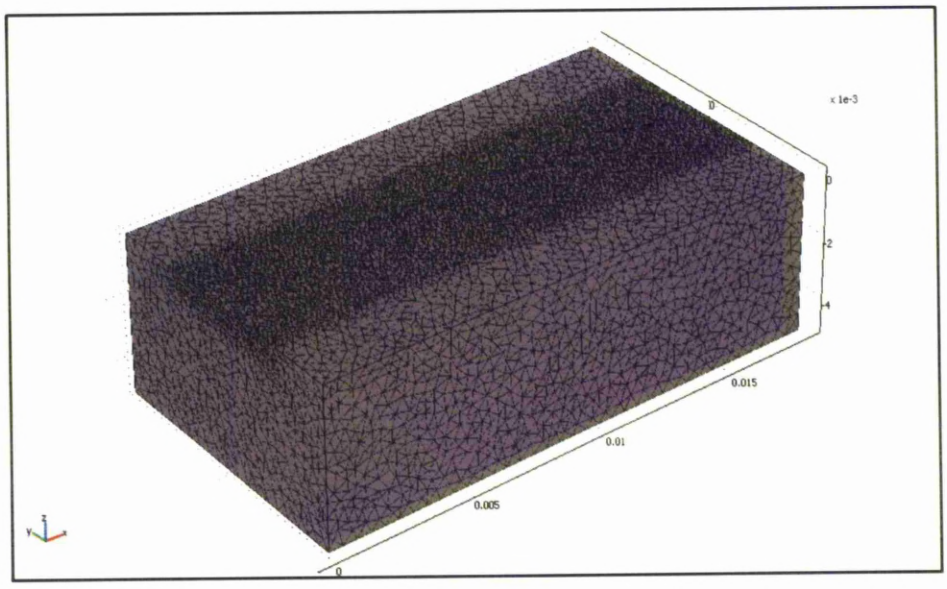

Figure 5: Meshed semi-infinite block with refined mesh in areas around and directly beneath the path of the moving heat source.

2.2.2.4 Solving the model

Once meshed the model is then ready to be solved. COMSOL[98] is capable of using 5 different types of solver to obtain a solution:

- Stationary
- Time dependent
- Eigenvalue
- Parametric
- Adaptive

Due to the nature of the problem being solved in this research, a time dependent solver was adopted.

There are a number of non-physical parameters in the program which must be correctly adjusted to ensure an accurate solution is obtained. Firstly the time stepping must be adjusted. Time stepping can be thought of as a splitting of the time dimension in a similar fashion to the mesh applied in the spatial dimensions. The time stepping in COMSOL[98] is set by the user. The user specifies a regular spacing between time steps which must be carried out carefully so that the last time step will converge with the total solution time, otherwise a solution cannot be obtained.

It is sensible to refer to the size of time steps as a proportion of the total elapsed time simulated in the solution similar to the way the mesh size is referred to in proportional terms as described earlier. Just as with the mesh, a suitable length for the time steps is found using an iterative method, doubling the number of time steps until no more than 0.5% difference occurs in maximum temperatures. In this research the time stepping proportion of the maximum solution time was set at 0.01 and the total solution varied between 1 and 18 seconds.

Tolerance levels must also be set. These are the permissible absolute and relative errors in each incremental time step in the solution and need to be set to be smaller than any total or incremental increases in the dependent variables expected in these steps. In this research they were set to accept the default relative (0.01) and absolute (0.001) tolerances given by the program. The total heat input was then iteratively

adjusted until a difference of no more than 0.5% in the maximum temperature increase was achieved. The tolerances refer to the how accurately the calculated solution satisfies the partial differential equation, equation [14].

To generate a quasi-steady state solution, the moving heat source was allowed to move a distance of 5 times the maximum beam radius R_0. This was controlled by adjusting the overall time according to the speed of the moving heat source to ensure the beam travelled the required distance. The Péclet number was adjusted by keeping the material properties and beam radius constant and by varying the traverse speed in the x direction along the surface of the semi infinite block. The intensity profile itself was specified using a mathematical function to describe its intensity profile in 2D space.

The solver is then started and a solution is generated.

Output solutions can be viewed in numerous ways. Figure 6 shows a 3D false colour output to the solution for a 2D heat source moving across the surface of a semi infinite block. The colours represent temperatures over a range specified by the bar on the right hand side.

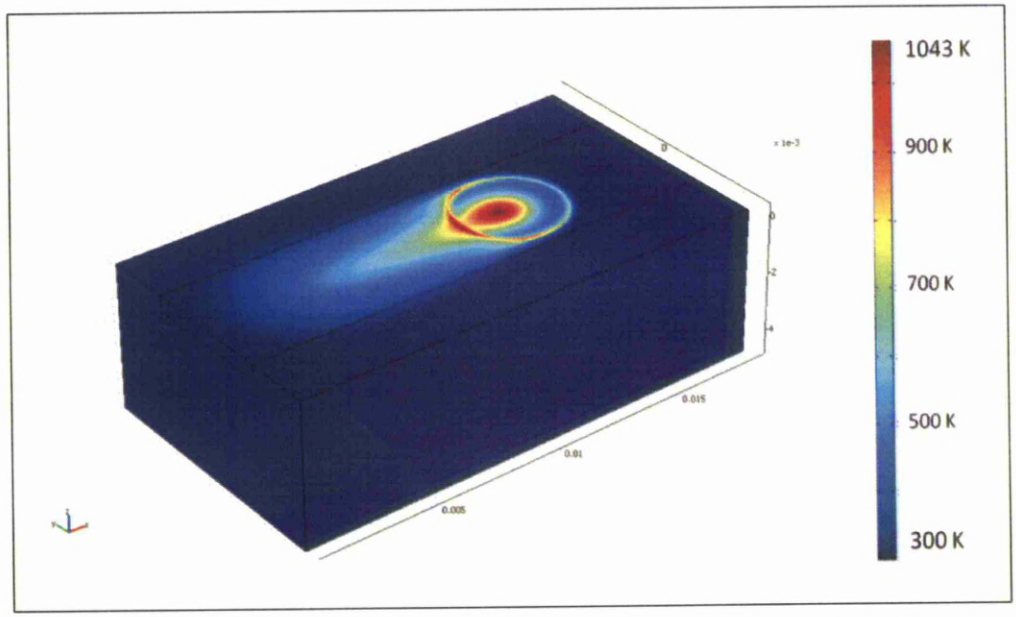

Figure 6: One example view of an output to a solution

2.2.2.5 Output measurements

For the purposes of this research, the output considered will be a normalised temperature distribution plot (ΔTDP) which shows the maximum temperature reached across the width of the treated area after the heat source has passed. An example of a temperature distribution plot of this type can be seen in Figure 7 the outline of which is shown adjacent to it. This is constructed by recording the temperature over a cross-sectional line under and orthogonal to the path of the moving heat source at fixed time intervals and superimposing them on the same graph. The dimensionless temperature at any point T^*:

$$T^* = \frac{(T - T_{init})}{(T_{max} - T_{init})} \quad [25]$$

Is plotted against the dimensionless width ψ:

$$\psi = \frac{y}{R_0} \quad [26]$$

This ensures the axes are normalised to unity in each plot allowing comparison between outputs.

The process of constructing these graphs is illustrated in Figure 7 and Figure 8 where the beam position relative to the reference line (which remains in a fixed position on the surface of the material) is shown in Figure 8 and an example of the resultant temperature distribution plot in Figure 7 with the first few temperature lines numbered according to the beam position in Figure 8. The overall outline of the contour plot therefore shows the relative maximum temperatures reached across the cross-section and it is this outline that is analysed for uniformity.

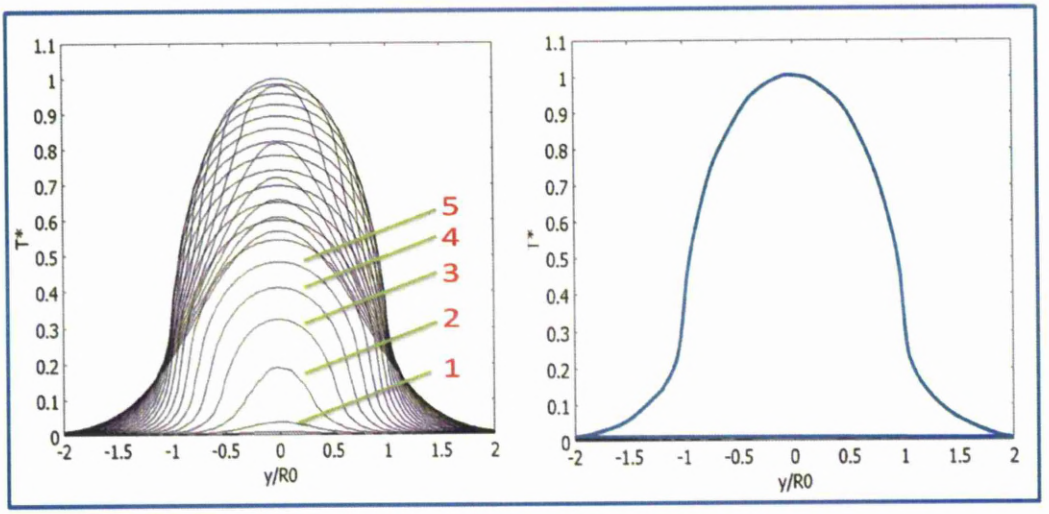

Figure 7: An Example of a Temperature Distribution Plot (left) and its outline (right).

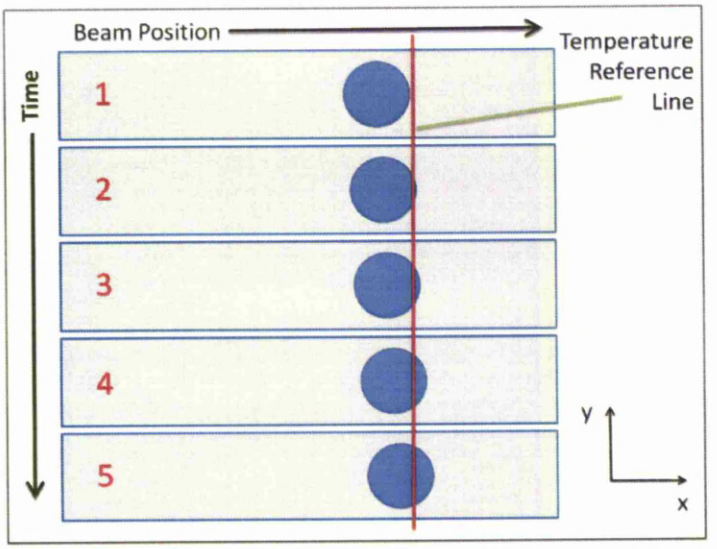

Figure 8: Schematic of time dependent beam position relative to reference line on material surface.

The measurements of the outline of the ΔTDP which are used to calculate the uniformity are shown in Figure 9.

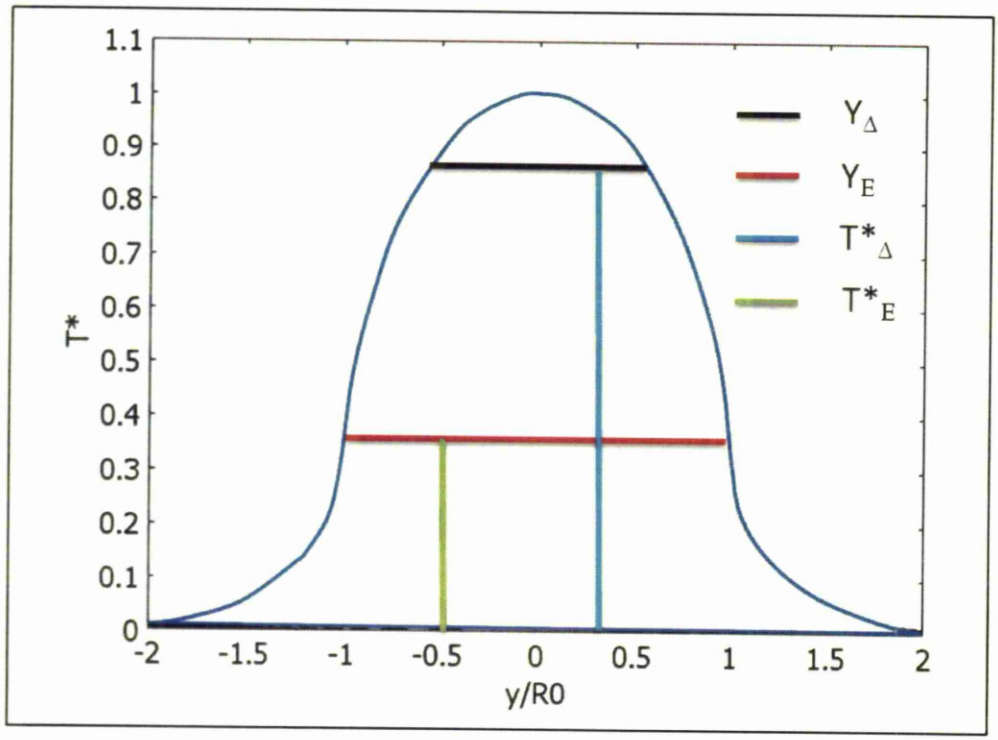

Figure 9: Measurements of the outline of the ΔTDP used in the calculation of its uniformity

The measure of uniformity U is taken as:

$$U_{T_\Delta^*/T_E^*} = \frac{Y_\Delta}{Y_E} \qquad [27]$$

Where Y_Δ is the width of the distribution which falls above a dimensionless temperature rise T^*_Δ at the top of the distribution and Y_E is the width of the distribution which reaches T^*_Δ at the bottom of the distribution. Temperatures above T^*_Δ but less than T^*_{max} can be thought of as existing within a level in which a treatment will bring about a desired change in a given material without overheating any portion. T^*_E can be thought of as relating to a temperature at a proportional threshold above which a mild or weak change will occur in the material which may distort or blur the edges of the affected zone. For the purposes of this investigation a uniformity of 1[i] is deemed ideal. Beam profiles will be compared at various Péclet numbers using this uniformity measurement. Where beam profile modulation is

[i] Due to thermal diffusion, a uniformity of 1 is not possible in real applications.

possible[j] the performance of the system at any Péclet number will be based on the best uniformity producible using that system[k]. A plot of the uniformity values versus Péclet number will be used to compare the flexibility and effectiveness of such systems compared with fixed beam profiles. The chosen values of T^*_Δ and T^*_E become the subscripts of U. For example in this research T^*_Δ and T^*_E are chosen as 0.95 and 0.37 (1/e) respectively, the uniformities will therefore be expressed as $U_{0.95/0.37}$. Choice of these arbitrary values for our measurement of uniformity will serve as an illustrative example and although relative uniformity measurements will be comparable with those made under other T^*_Δ and T^*_E values, the absolute measurements of uniformity will be different.

Assessing the ΔTDP outlines for uniformity in this way only addresses the maximum temperature rise achieved across the width of the treated area and therefore addresses only the first of the three criteria for uniform heat treatment. Temporal characteristics such as heating and cooling rates and the time period the material remains above a threshold temperature are not accounted for in this type of measurement. Aiming to optimise these temporal characteristics is assumed to be much more problematic for circularly symmetric moving heat source intensity profiles due to the substantial difference in the time spent under the heat source for central areas compared with areas at the edge of the treated area. This is illustrated in Figure 10 and Figure 11. When optimising circular heat source intensity profiles for uniform heat treatment of surfaces, the aim will be to achieve uniformity in the maximum temperature rise at the surface or at a specified depth. The effect this has on variation in temporal temperature characteristics across the width of the treated area at different Péclet numbers will merely be reported as a consequence of achieving this uniformity.

[j] In the new optical design proposed or in any previously reported optical system such as Crafer and Oakley's.

[k] At each Péclet number the profile will be adjusted within system constraints until peak uniformity is achieved.

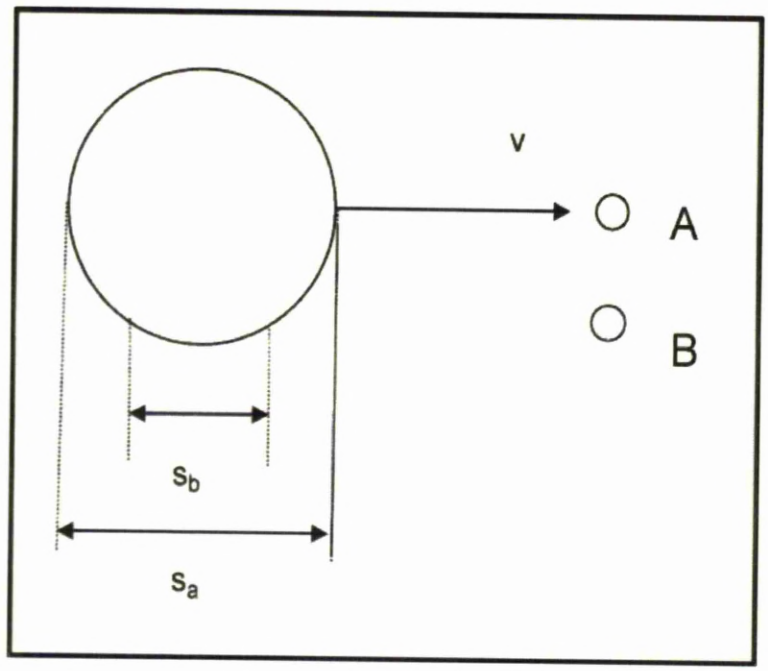

Figure 10: Illustration of interaction time variation between areas under the centre and edges of the moving heat source

Figure 11: Interaction time vs. distance from centre of circular heat source (both axes are normalised to unity).

2.3 Traditional Laser Heating Problems

Gaussian beam intensity profiles occur naturally as the operating mode for many lasers. The proximity to a true Gaussian profile (a beam with an M^2 of 1) is often considered a mark of quality. There is good cause for this – the achievable minimum spot size and the divergence of the beam both benefit from low M^2 values as does the propagation of the beam through an optical system[21]. Reduction in spot size is critical for high fluence applications such as laser cutting and for applications where resolution is important such as in laser marking. Hence a near as possible Gaussian beam is sought for these applications. Some applications however (particularly in the field of laser surface treatment) require different intensity profiles for optimum performance[118]. Laser surface heat treatments such as those summarised in section 2.1.3 often benefit from a uniform treatment. A Gaussian intensity distribution is not capable of providing uniform heat treatment during a single scan. The large disparity between the intensity at the centre of the Gaussian beam and that at its outside edge leads to significant overheating at the centre of the processed area[119]. Removal of the high intensity variation across a Gaussian beam can be carried out by homogenising the beam. Homogenising the beam creates a top-hat[I] shaped intensity profile – a circular geometry with uniform intensity. To those inexperienced in the study of the effect of moving heat sources, the uniform intensity profile of the top hat beam may seem an appropriate approach when attempting to achieve a uniform surface treatment. The circular shape of the beam however dictates that, when the heat source or laser beam in this case is moving, points further from its axis of movement experience reduced beam interaction time which leads to under-heating compared with points at the centre.

[I] Also known as a Fermi-Dirac distribution.

2.4 Literature Review: Existing Solutions to Traditional Laser Heating Problems

2.4.1 Engineering the Movement of the Laser Beam

The problem of overheating in the centre of the area under the path of the moving beam can be compensated for by overlapping adjacent passes of the beam. Overlapping the beam however can cause fluctuation in the surface properties. Ingelgem et al[120] for example noted the effect of excessive overlapping on the uniformity of surface hardness of stainless steel. They reported a reduction in surface hardness in the overlapped area when overlapping was increased from 10% to 50% due to back tempering of the hardened region formed in previous passes. Kim et al[121] report a similar effect in their paper on laser transformation hardening of rod shaped carbon steel where back tempering led to major fluctuations in surface hardness across the width of the treated area.

Rapid scanning of a focused laser beam can be used to create the desired temperature distribution on the surface of a material. Bonss et al[122] showcased the use of rapid scanning mirror optics to harden wide areas of metallic parts. Using a high powered diode laser with long focal length optics an area 27mm wide was hardened to a consistent degree and depth. The authors discussed the possibility of varying the time dependent scanning functions and time periods to alter the temperature distribution created to suit specific surface heating applications.

Ensuring uniformity across the width of the area under the beam is essential if uniformity is desired in one pass of the beam or if the overlapping ratio is to be minimised. There are two types of modifications that can be made to the laser beam in order to attempt to achieve this – engineering the beam geometry (the outline shape of the beam cross-section) and engineering the cross-sectional intensity profile of the beam within the beam geometry. The latter will be dealt with first.

2.4.2 Engineering the Intensity Profile

Shaping the intensity profile of a moving laser beam can have a massive effect on the temperature distribution on the surface of a material. Previous studies have shown

ingenuity in both the intensity profiles created [4, 6, 123, 124] and in the methods used for creating them [8, 125-127]. Victor et al[124] produced a single novel transmissive optic with three sections to create one leading and two trailing beams from an input Gaussian beam for laser welding. They reported increased smoothing of weld toes compared with using a conventional Gaussian beam due to the post-heating effect created by the trailing beam portions. A Gaussian beam was quartered using reflective optics to create a square shaped uniform temperature profile under a stationary beam[128]. The quarters of the beam were positioned in a square shaped pattern with the maximum intensities appearing at the corners of the square to compensate at places where lateral conduction losses are greatest. The effect of laser mode on the surface temperature distribution was investigated by Kar and Langlais[129] and earlier by Sharp[130] who modelled the difference in heating effects between TEM_{00} and TEM^*_{01} modes. Both investigations showed that the TEM^*_{01} mode gave a more uniform heating effect across the width of the treated area. More recently Gibson et al[4] created a novel beam intensity profile using diffractive optics for use in direct metal deposition of Inconel 625. A 'rugby posts' shaped intensity profile with square beam geometry was formed to create the desired uniform temperature distribution on the material surface. This beam profile can be seen in Figure 12. The temperature distribution created was more uniform than that created by a Gaussian beam, resulting in a flattened topology and a reduction in both the maximum and average grain sizes in the deposited layer.

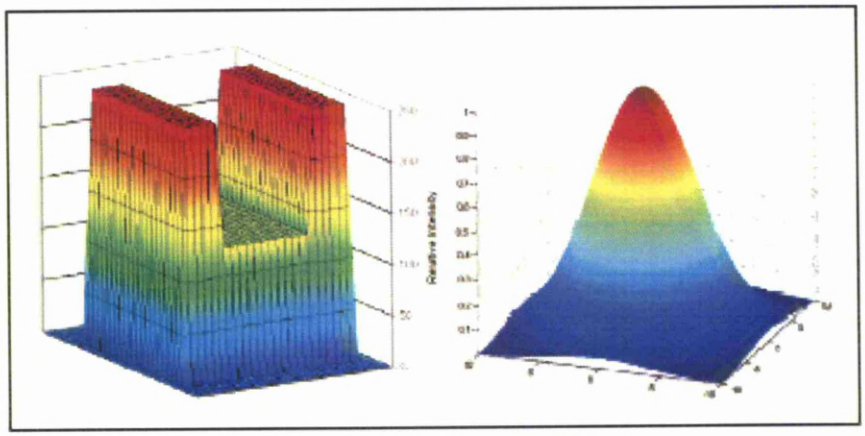

Figure 12: Rugby shaped intensity profile (left) as compared with a Gaussian intensity profile (right). From Gibson et al[4]

A strip-shaped beam geometry with an M-shaped intensity profile (seen in Figure 13) was created by Hagino et al using a computer generated hologram. Like Gibson et al[4] the optimum beam profile for the target application (in this case laser transformation hardening) was developed using finite element analysis of the temperature distribution. The profile was tested using the output from a high-powered diode laser to harden the surface of S45C medium carbon steel and the results compared with those obtained for top hat and Gaussian shaped beams. The M shaped profile performed considerably better than the top hat and Gaussian beam profiles, achieving shallower hardened regions with higher uniformity in depth across the width of the treated area.

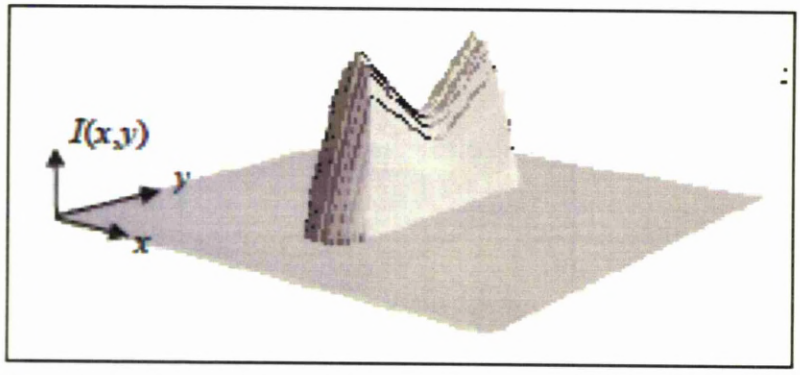

Figure 13: Intensity profile created for laser transformation hardening by Hagino et al[131].

The optimum intensity profile for creating a uniform temperature distribution within the area under a moving square shaped beam was formulated after Burger et al[132] and is shown in Figure 14. Along its length (parallel to the direction of movement), the profile has a very high intensity leading edge to immediately raise the temperature to the desired level – the intensity drops towards the trailing edge to maintain this temperature. Across its width the beam has an 'armchair' shaped intensity profile to compensate for lateral conduction losses.

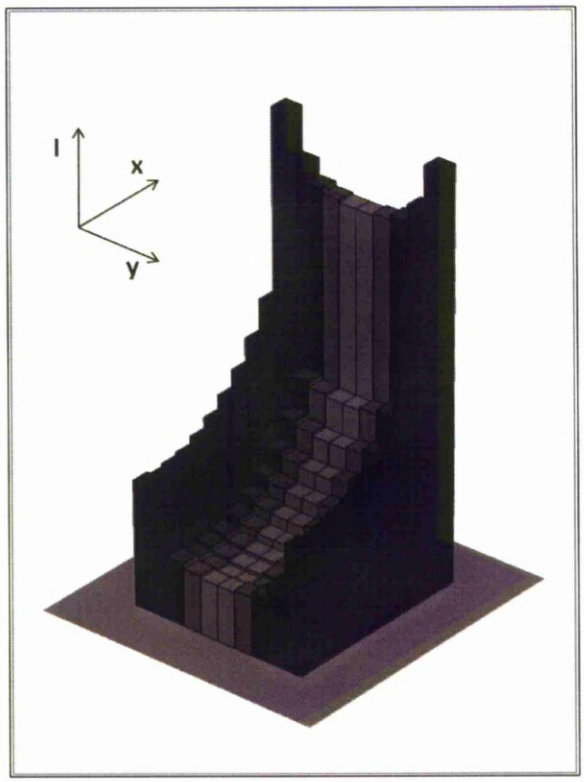

Figure 14: Qualitative representation of ideal intensity profile for homogenous heating inside the illuminated area after Burger[132]

Burger calculated the transformation hardened case depth for both uniformly illuminated square beams and the calculated intensity profile for uniform heating inside the illuminated area shown in Figure 14. He concluded the following:

- For all intensity profiles, case depth becomes shallower as the Péclet number is increased.
- Case depth at any fixed Péclet number depends on the intensity profile
- Case depth is at a maximum when there is a homogenous temperature field at the surface, such as when using the optimised intensity profile shown in Figure 14.

An important point to note is that Burger designed this intensity profile for a specific material and the optimised intensity profile in Figure 14 is only optimised for use over a relatively short range of Péclet numbers.

2.4.3 Engineering the Beam Geometry

For uniform temperature distribution across the path of movement it has been shown that a strip (or short rectangle) geometry is highly effective [1, 7, 133]. Leung et al [7] reported uniform hardness across a 15 mm wide area treated with a 15mm by 2mm strip shaped beam. Square shaped and long rectangle[m] distributions are less effective due to conduction losses at the outer edges. Triangle[11] and diamond[9] shaped beams have also been noted for their advantages in achieving uniform temperature distributions and slower heating and cooling rates which provide benefits such as for martensite formation in laser transformation hardening[15]. Triantafyllidis et al[2] investigated using different beam geometries to alter the cooling rates for laser surface treatment of ceramics. They found that rhomboid and pi shaped beam geometries caused reduced cooling rates and that uniform strip shaped beams caused higher cooling rates compared with circular, triangular and rectangular beams. Safdar et al[12] studied the effect of beam geometry on the stress distribution in laser bending of tubes. It was found that a doughnut shaped beam produced the least lateral bending, the circular beam produced the highest bending angle, the triangle beam produced the least inner distortions and the rectangular beam produced the least outer distortions. Stultz[35] reported the effect of altering the beam geometry on the grain size and grain growth direction in laser annealing of amorphous silicon substrates. Tilted half moon, crescent and extended crescent beam geometries each caused grain growth in a different direction to create polycrystalline microstructures.

2.4.4 Addressing the Problem of Directionality: Why Use Circular Beams?

Achieving true uniformity in heating and cooling rates and in other temporal temperature characteristics is impossible with a circular circularly symmetric beam. The difference in interaction time between points passing under the centre of the beam and points passing under the edges of the beam is inescapable.

It would be reasonable to ask at this point why anyone should be interested in circular beams for uniform surface treatment. The previously given examples of effective

[m] Long and short rectangles refer to the orientation of the rectangle with respect to the direction of movement; this is parallel to the longest and shortest sides respectively.

beam geometries for uniform surface treatment have almost completely consisted of non-circular beams.

In some laser processes, particularly in processing of 3D parts and components, changes in the direction of movement are necessary. In many cases any differences in treatment with processing direction would be undesirable. Circularly asymmetric beam profiles will perform differently when moved in different directions. For example a square beam will appear diamond shaped when moved at 45 degrees rather than orthogonal to its sides. The difference in the temperature distribution created when different orientations of the same shape are used is highlighted by Safdar et al [15, 16] where triangles and rectangle shaped beams were used in different orientations to different effect. It was reported that a forward facing triangle geometry (base trailing apex) gave much lower heating rate than a rearward facing triangle geometry (apex trailing base) due to the increase in line density (energy per unit length in the lateral direction to scanning) from front to rear. The papers also provided some insight into the effect of characteristics of the beam geometry on the heating and cooling rates. For example a beam geometry with a short length in the scanning direction will lead to high heating rates but low cooling rates.

Safdar et al's papers[9-12] raise an important point in laser materials processing which is highly significant for this research and worth repeating: changing the orientation of the beam geometry can have a drastic effect on the temperature distribution on the surface of a material.

At this point it is important to emphasise a key point which is part of the motivation for the direction in which this research is aimed: the only beam that is capable of having the same effect on any isotropic material in any orientation is a circular geometry with a circularly symmetric intensity profile. If omnidirectionality in the processing direction is essential for a given laser surface treatment then this is clearly a very important point indeed. For these reasons and due to the problem of non-uniformity having been solved by previous authors using non-circular beams, research in this thesis is directed at optimising the intensity profile of circular beam geometries.

2.4.5 Annular Ring Intensity Profiles

One circularly symmetric beam profile which is capable of achieving a relatively uniform maximum temperature rise on a surface is the annular ring. Annular rings are noted for having some success achieving more uniform heating effects both in stationary[134] and moving beam applications[135]. At low Péclet numbers heat conduction within the material balances the effects of the moving annular ring heat source which naturally heats the outer edges of the treated area more than the centre.

2.5 Finite Element Modelling of Circularly Symmetric Laser Beam Profiles

In the following section finite element modelling is carried out to analyse the effect of various circularly symmetric beam profiles using the methods detailed in section 2.2. Known fixed intensity profiles are modelled to illustrate the issues surrounding shaping the intensity profile to achieve a uniform maximum temperature rise on the surface of a material. The effect of varying the Péclet number will illustrate the variation in effectiveness of any fixed intensity profile once processing conditions or the material is changed. Dynamic profiles are then investigated as a solution to retaining a beam profile's effectiveness over a wide range of Péclet numbers.

2.5.1 Fixed Intensity Profiles

2.5.1.1 Conventional Beam Profiles

Using the COMSOL[98] model, three standard heat sources are simulated traversing the surface of a semi-infinite block. 2D Gaussian, top-hat and annular ring heat source intensity profiles shown in Figure 15 are made to traverse the surface of a semi-infinite 3D block.

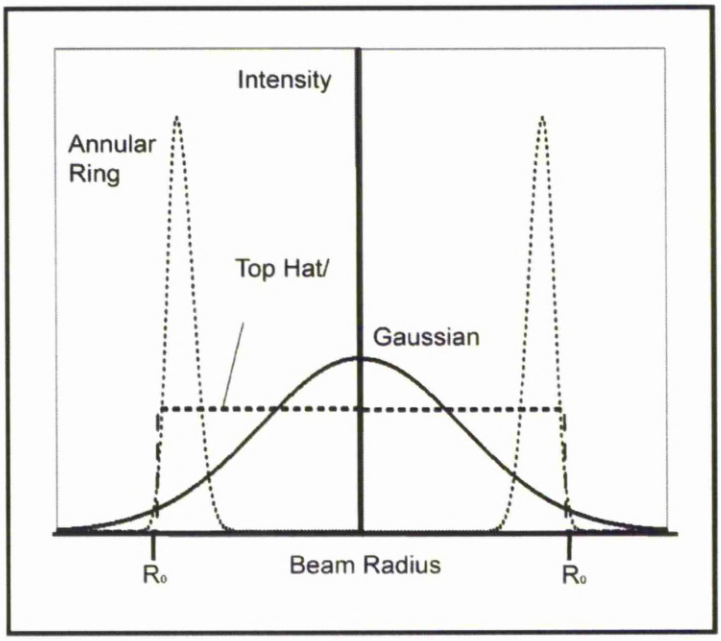

Figure 15: Intensity profile plots for Gaussian, top hat and an annular ring profile.

After a sufficient time lapse, the model solver is stopped and ΔTDPs are taken to assess the level of uniformity achievable with each heat source over a range of Péclet numbers from 6 to 96. This Péclet number range covers a large proportion of processes reported in the literature from which Ion et al[91] sourced their dimensionless parameter sets shown in section 2.1.3.8. Example ΔTDP's are shown in Figure 16 to illustrate how the temperature across the width of the material evolves as the beam passes over it.

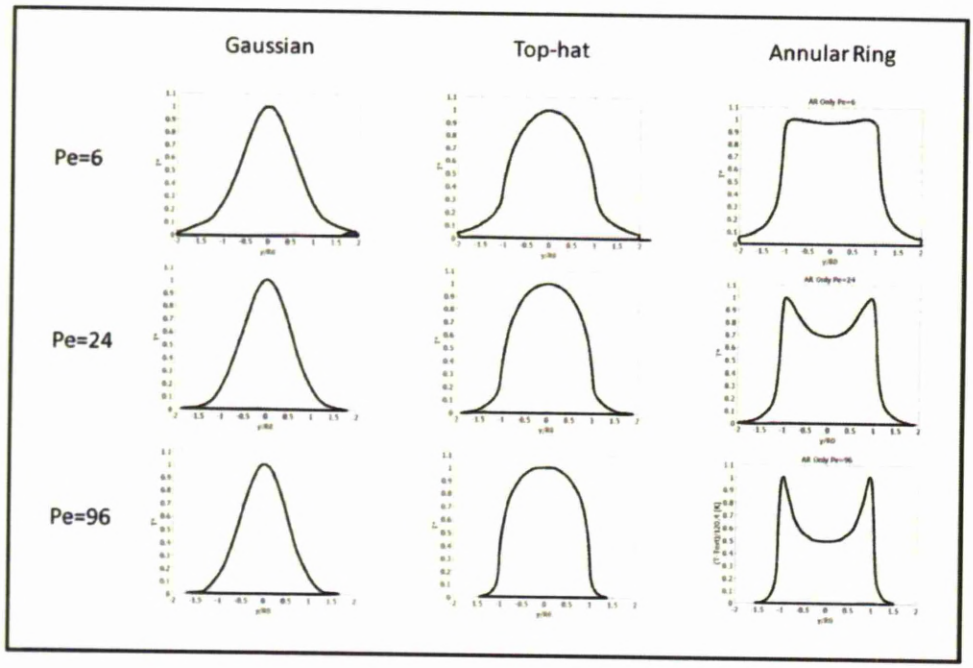

Figure 16: Example surface ΔTDPs for Gaussian, top-hat and annular ring heat sources at three different Péclet numbers.

As previously discussed in section 1.1.2, circularly symmetric moving Gaussian and top-hat beams are poor at achieving a uniform maximum temperature rise on the surface of a material. Gaussian beams overheat the centre of the treated area due to three factors:

1. Intensity in the centre of the profile is far greater than that at the outer edges
2. The circular shape of the beam outline causes the edges of the treated area to experience reduced interaction time compared with the centre of the treated area
3. Lateral conduction at the edges of the treated area

Top hat beams overheat the centre of the treated area due to factors 2 and 3 above. The annular ring however is able to produce a highly uniform maximum temperature rise in the transverse direction (along the surface and perpendicular to the axis of the moving beam) at *Pe=6*. As the Péclet number is increased however, the edges of the

treated area are overheated compared with the centre because in this case heat generation within the material due to the beam intensity profile dominates over heat conduction within the material. At a Péclet number lower than 6 the centre of the treated area becomes overheated compared with the edges due to heat conduction effects dominating. The performance of each of the intensity profiles can be represented in a plot of uniformity values vs. Péclet number. Such a plot can be seen in Figure 17.

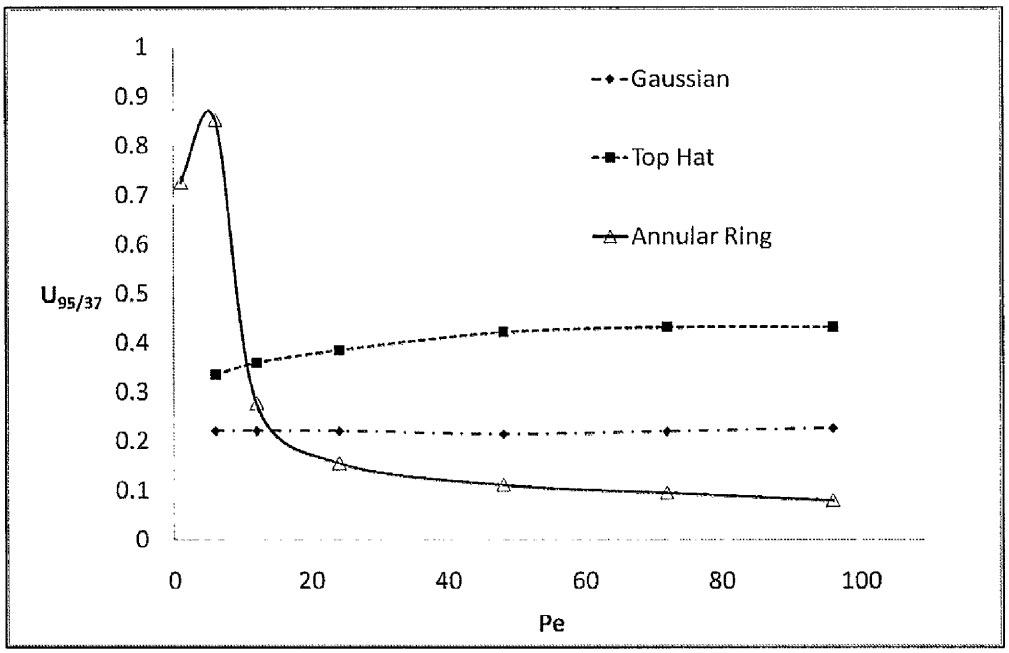

Figure 17: Uniformity vs. Péclet number for Gaussian, top-hat and annular ring beams. Uniformities are measured as $U_{95/37}$

The annular ring is clearly capable of achieving the best uniformities at lower Péclet numbers but its performance fails dramatically as soon as the Péclet number is increased.

As yet only the surface temperature distribution has been considered. Since most laser surface processing techniques require heating to a certain depth, it is important to highlight the effect of the temperature distribution on the surface on the temperature distribution at some depth beneath the surface. This is especially important for the surface ΔTDP's created by annular rings as they will form the basis

of the solution to the problem investigated in this thesis. The reasons for this are a matter for later discussion.

A selection of ΔTDPs at depths beneath the surface over a range of Péclet numbers are shown in Figure 18 for the annular ring shown in Figure 15.

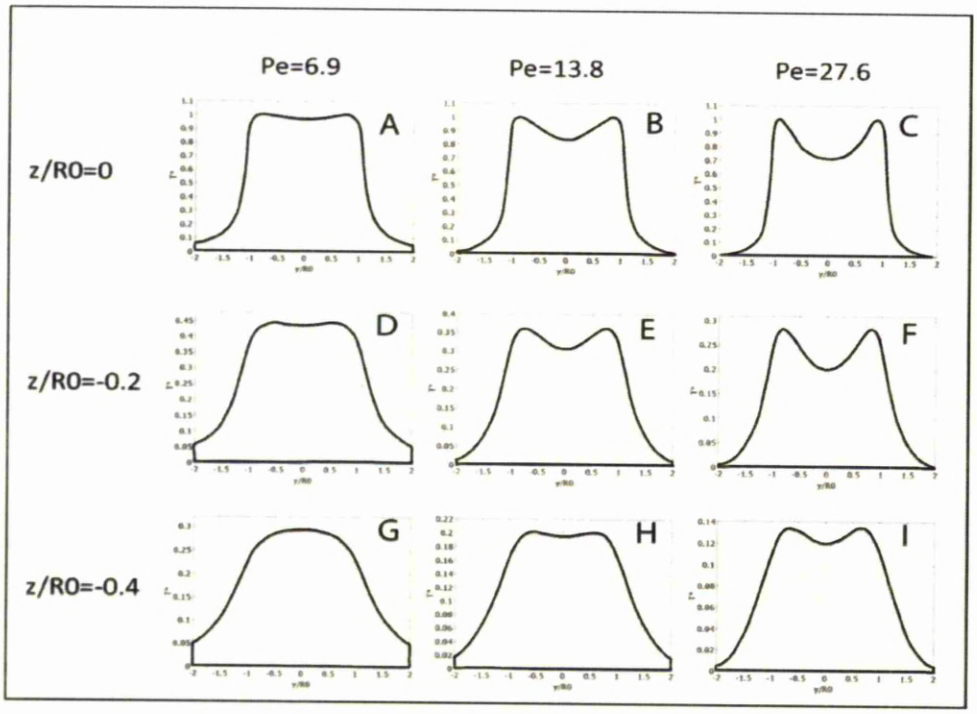

Figure 18: Selection of ΔTDP's at the surface and at depths below the surface created by an annular ring.

Due to the conduction of heat laterally as well as downwards through the material, the *ΔTDPs* change for each Péclet number through the depth of the material. The temperature distribution plots in Figure 17 highlight an important feature of *ΔTDPs* through the depth of a material created by the annular ring. If there is overheating at the outer edges at the surface as in plot B or C, the *ΔTDP* becomes more uniform at greater depths as in plots H and I. For the same reasons if the surface *ΔTDP* is uniform at the surface as shown in plot A then this can lead to the *ΔTDP* at greater depths becoming overheated in the centre as shown in plot G.

The uniformities achieved by the annular ring in Figure 15 at the surface and at two depths below the surface are shown in Figure 19. The uniformities were measured relative to the maximums in each *ΔTDP* rather than the maximum in the surface *ΔTDP*.

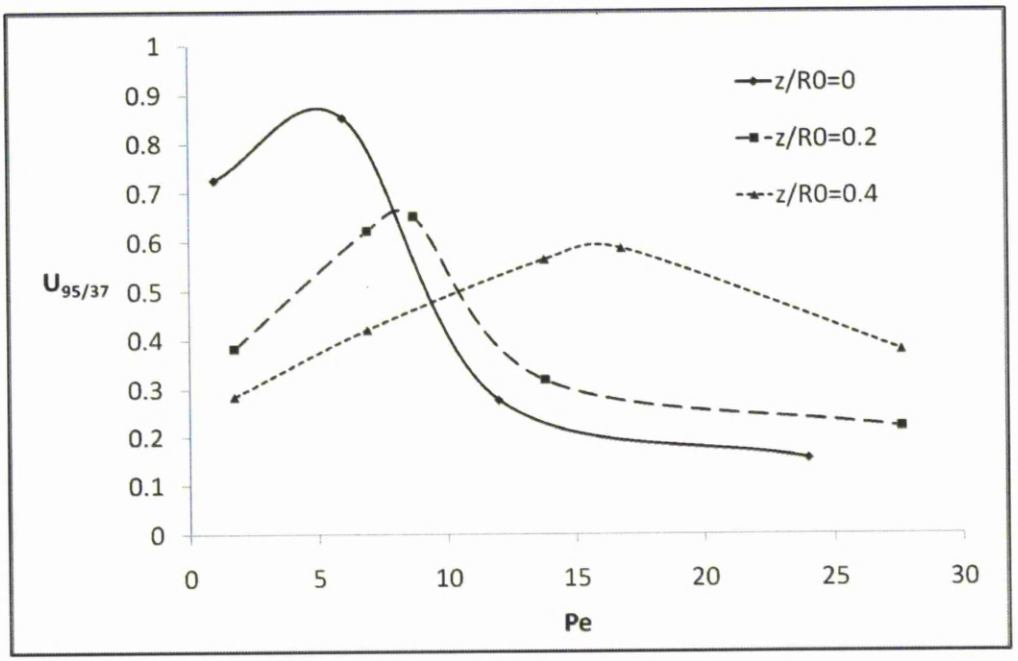

Figure 19: Uniformities in the ΔTDP at the surface (z/R0=0) and at depths z/R0=0.2 and z/R0=0.4 beneath the surface.

Figure 19 shows that if uniformity in the *ΔTDP* is required at a depth beneath the material then the *ΔTDP* at the surface must be made non-uniform by allowing overheating to occur at the outer edges.

2.5.1.2 Annular Rings

The annular ring shown in the previous section is obviously not the only type of annular ring imaginable. It must be categorised so that it can be compared to other forms of annular ring. The two categorisations which will be used to describe an annular ring intensity profile henceforth will be:

1. The shape of the annulus itself
2. The spread of the shape over the beam radius

The annular ring referred to in Figure 15 to Figure 17 is an FGAR (full Gaussian annular ring) which has a large difference between the ring thickness and the overall beam size. Full Gaussian refers to the shape of the annulus itself and the ring width to overall beam size refers to the spread of the annular ring Σ which will be expressed as follows:

$$\Sigma_{FGAR} = \frac{2w_{0FGAR}}{R_{0FGAR}} \quad [28]$$

Where w_{0FGAR} refers to the distance between the peak of the annulus and the radius at which the intensity falls to $1/e^2$ of its peak value. R_0 refers to the overall radius of the beam which is the distance from the centre of the beam to the furthermost point at which the intensity falls to $1/e^2$ of its peak value. In the case of an FGAR, R_0 is equal to the sum of the peak to centre distance b and ring width w_0.

Other types of annular ring shape include but are not limited to:

1. OHGAR - outer-half Gaussian annular ring
2. IHGAR – inner-half Gaussian annular ring

For OHGARs and IHGAR's, the factor of 2 is removed from the expression describing the spread since they are effectively only half Gaussian functions. Therefore:

$$\Sigma_{OHGAR} = \frac{w_{0OHGAR}}{R_{0OHGAR}} \quad [29]$$

$$\Sigma_{IHGAR} = \frac{w_{0IHGAR}}{R_{0IHGAR}} \quad [30]$$

This short list is by no means exhaustive but the $\Delta TDPs$ created by these annular rings (each with various spread values) will illustrate what is important in terms of the shape and spread of an annular ring at various Péclet numbers when it comes to achieving high uniformities.

The FGAR, OHGAR and IHGAR with Σ values of 0.15, 0.50 and 1.00 are shown in Figure 20. Increasing the spread of an FGAR reduces the definition at the edge of the intensity profile, shifts the annular peak towards the centre and increases the proportion of energy in the central areas compared with the edges.

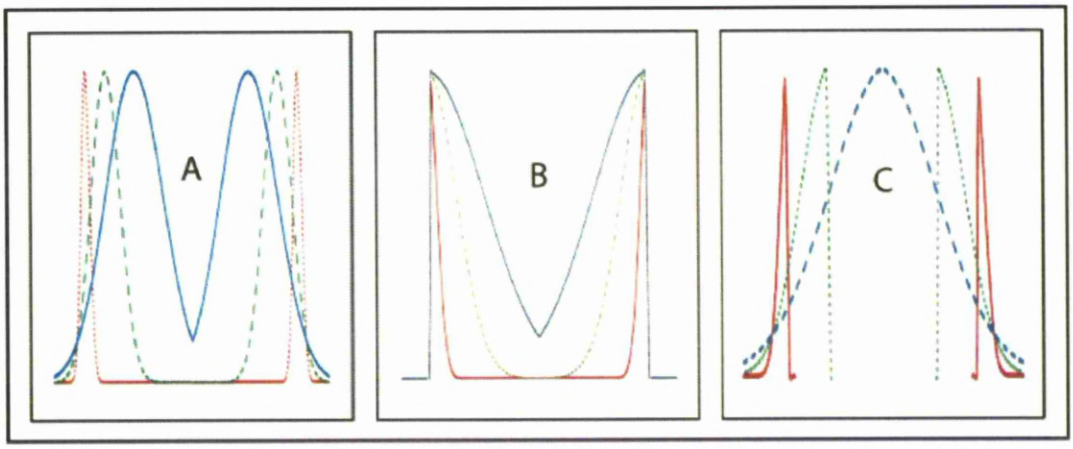

Figure 20: Various annular ring shapes and spreads: A- FGAR; B- OHGAR; and C- IHGAR with Σ values of 0.15 (red), 0.50 (green) and 1.00 (blue).

Each of the nine profiles shown in Figure 20 is simulated in the COMSOL[98] model to show the effect of shape and spread of an annular ring on the ΔTDP created.

First the FGAR profiles shown in Figure 20 plot A are tested. Example *ΔTDPs* are shown in Figure 21 for the three FGARs tested at various Péclet numbers.

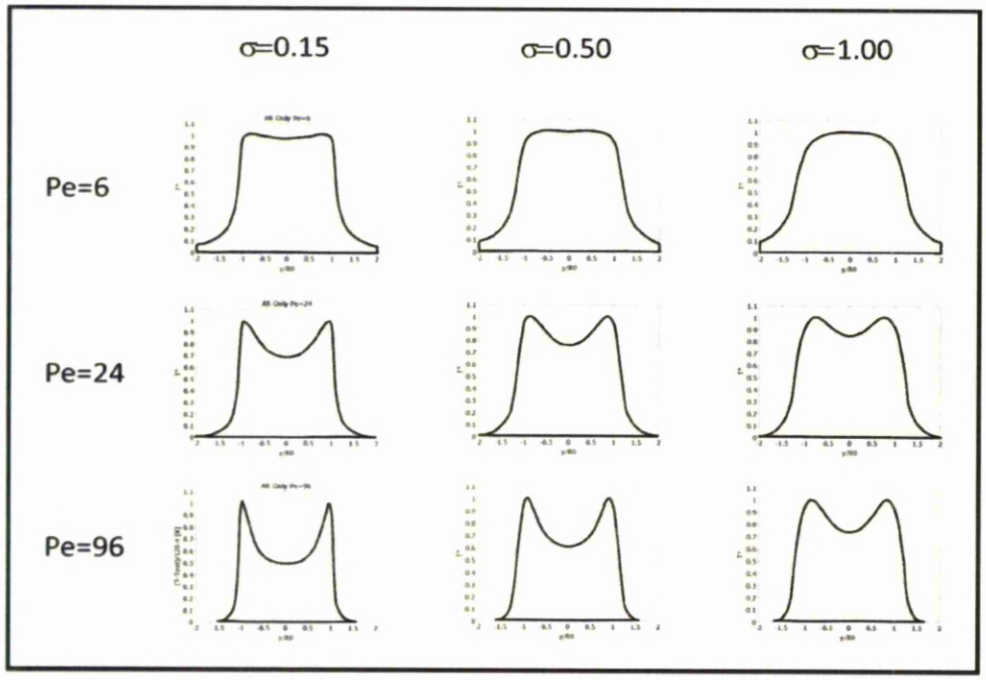

Figure 21: ΔTDPs created at various Péclet numbers (vertical labels) for FGARs with different spreads (horizontal labels)

A plot of Uniformity vs. Péclet number for FGARs is shown in Figure 22.

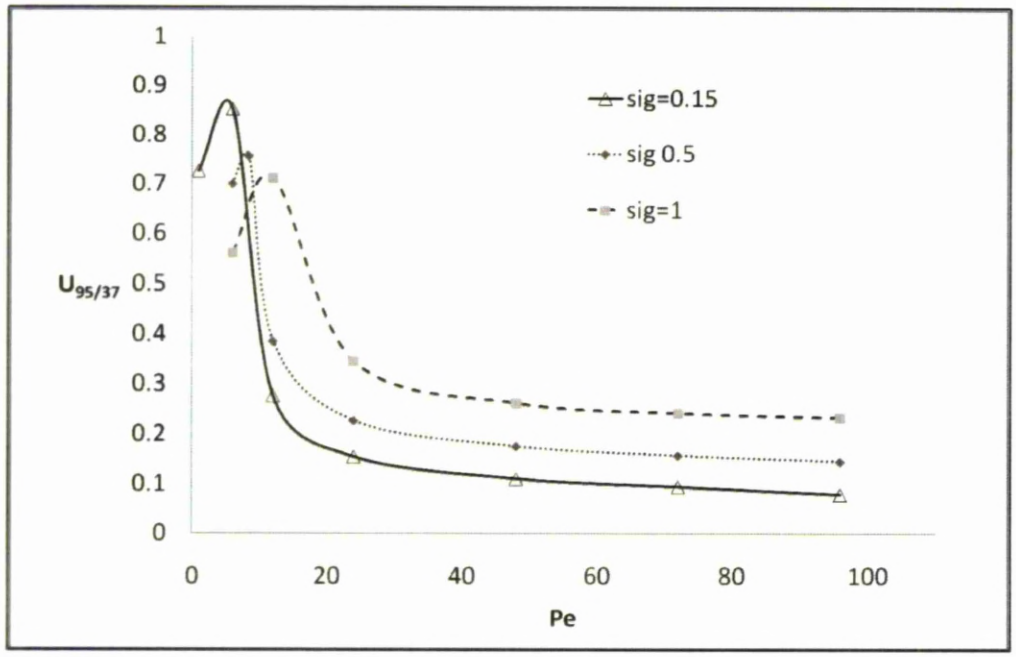

Figure 22: Uniformity vs. Péclet number for FGARs with various spreads.

This shows clearly the effect of increasing the spread of an FGAR on the maximum uniformity achievable with an FGAR. Increasing the spread in this case reduces the maximum uniformity achievable, increases the Péclet number at which the maximum uniformity occurs and increases the range of Péclet numbers around the optimum at which high uniformities are still achievable.

Next, each of the OHGAR intensity profiles shown in Figure 20 plot B are simulated in the model. A selection of the ΔTDPs created by these profiles at various Péclet numbers is shown in Figure 23.

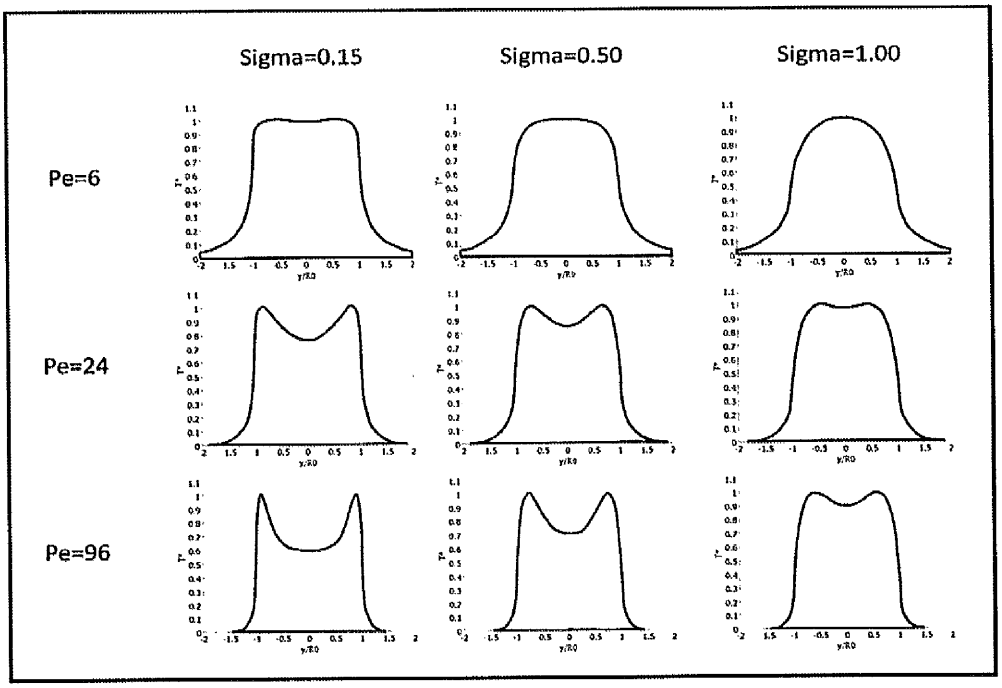

Figure 23: ΔTDPs created at various Péclet numbers (vertical labels) for OHGARs with different spreads (horizontal labels)

A plot of uniformity vs. Péclet number is shown for the OHGARs in Figure 24.

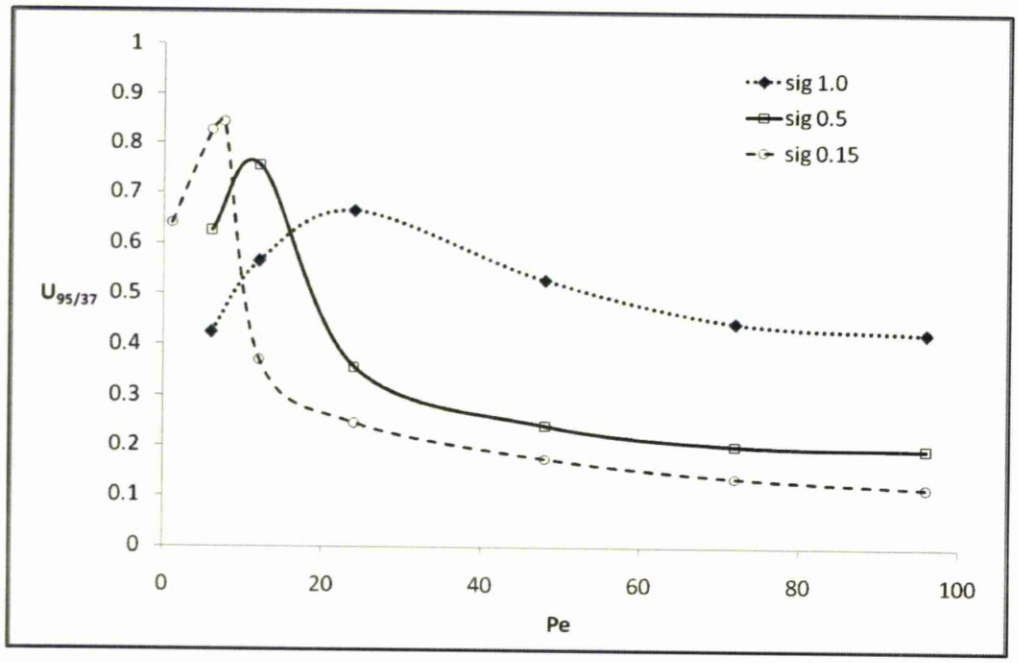

Figure 24: Uniformity vs. Péclet number for OHGARs with various spreads.

Finally for IHGARs a selection of the ΔTDPs (Figure 25) and a plot of Uniformity vs. Péclet number (Figure 26) follow.

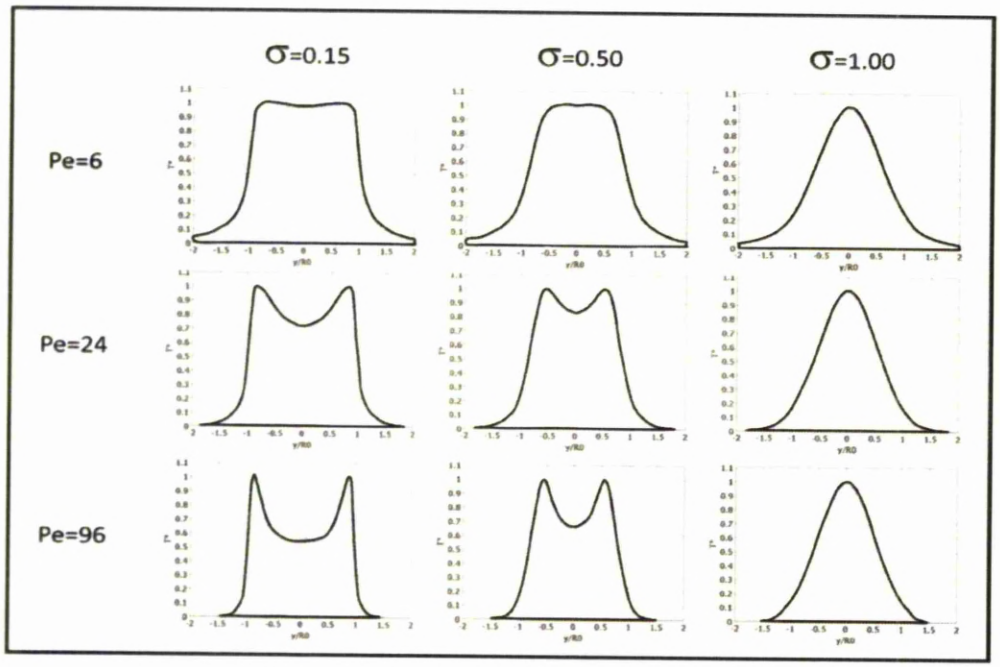

Figure 25: ΔTDPs created at various Péclet numbers (vertical labels) for IHGARs with different spreads (horizontal labels)

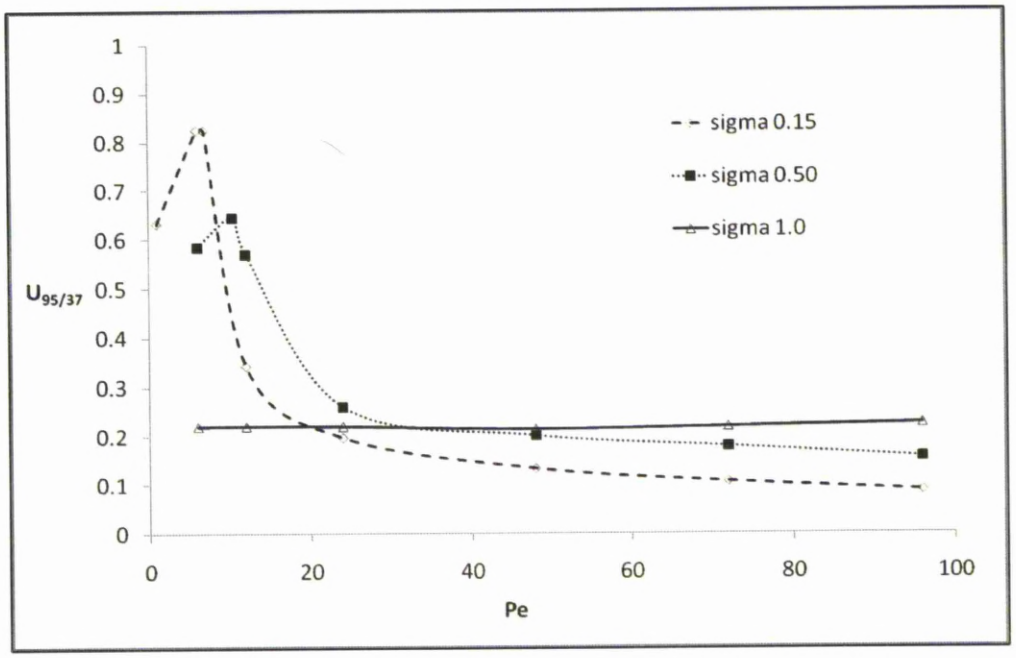

Figure 26: Uniformity vs. Péclet number for IHGARs with various spreads.

It is clear that definition at the radial edge of any annular ring profile is important in achieving a steep sided ΔTDP. Poor definition leads to shallow slopes in the ΔTDP created which is undesirable when attempting to achieve high uniformities.

No one fixed annular ring profile performs well over a wide range of Péclet numbers. This is unsurprising as the temperature distribution is not only a function of the profile itself but also of the Péclet number. Each profile has an optimum Péclet number at which they achieve their highest uniformity both sides of which uniformities decrease – steadily for lower Péclet numbers and markedly less steadily for higher Péclet numbers. The consequence of this is that any profile's usefulness is limited to specific applications under which the Péclet number matches or is close to the optimum one for that profile.

The only way to ensure high performance over a wide range of Péclet numbers is to modulate the intensity profile of the heat source to adjust for changes to the ratio of heat generated by the moving heat source to that conducted within the material.

2.5.2 Dynamic Intensity Profiles

It is hereby proposed that a fixed annular ring profile with an added central intensity feature of adjustable relative power could be a possible solution to the problem presented in the previous section.

If one annular ring is to be chosen on top of which another feature were to be added, the question of which annular ring to choose may appear subjective. However some objectivity can be introduced by considering that if it is a requirement that the intensity profile produce high uniformities in the ΔTDP across a wide range of Péclet numbers then the annular ring chosen as the base profile (to which another intensity feature will be added) needs to produce high uniformities at the lowest Péclet number possible when used on its own. It has already been shown that if the Péclet number is lowered beyond its optimum value for any annular ring, then the uniformity drops due to overheating in the centre of the treated area. Therefore any intensity feature addition inside or on top of the annular ring cannot serve to improve performance at Péclet numbers lower than the optimum value. Improvements to an annular ring profile's overall performance by adding a central intensity feature is only possible at Péclet numbers higher than the optimum one for that particular annular ring.

An FGAR with a low Σ achieves a relatively high uniformity at its optimum Péclet number. Its optimum Péclet number is also relatively very low which means it fulfils the previously dictated requirement for a base annular ring profile on which to add the central intensity feature.

Now that the base annular ring has been chosen a further question remains as to what shape the added central intensity feature should take. Three shapes will now be considered for the central intensity feature:

A. Gaussian
B. Plateau
C. Holey Gaussian

Each of which are shown along with the base annular ring in Figure 27.

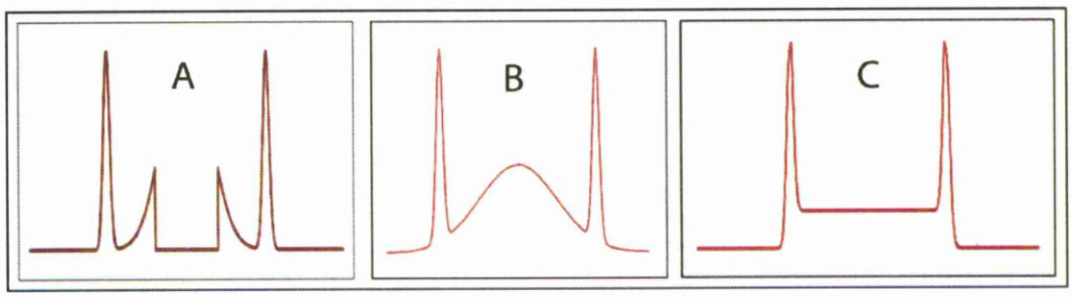

Figure 27: Comparison of central intensity profile feature additions to base annular ring. A- Gaussian; B- Plateau; C- Holey-Gaussian.

Each of these central intensity features is tested for its effectiveness in compensating for the energy deficit in the centre of the base annular ring profile. Beginning at the optimum Péclet number for the base annular ring, the central intensity feature is gradually increased with increasing Péclet number so as to optimally compensate for the reduction in heat conduction relative to the heat generated. Therefore at each Péclet number the relative power of the central intensity feature compared with that of the annular ring is optimised for highest uniformity values. The effect of each central intensity feature when combined with the base annular ring on the ΔTDP is shown at various Péclet numbers in Figure 28. A plot of uniformity vs. Péclet number is also shown in Figure 29 so that the performance of the three central intensity feature additions can be compared.

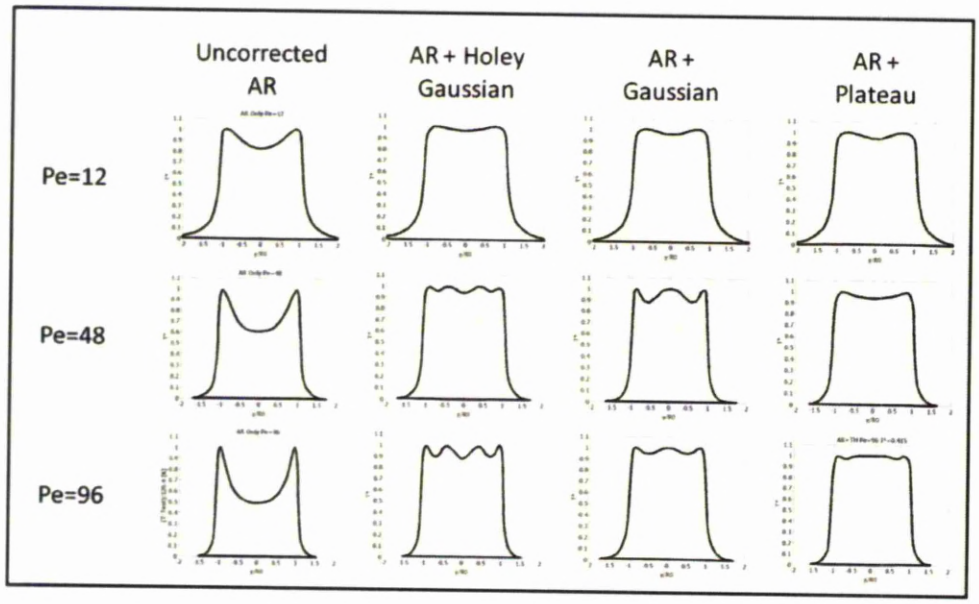

Figure 28: ΔTDPs at various Péclet numbers created by filled annular rings, those created by the unfilled annular ring are shown for comparison on the left.

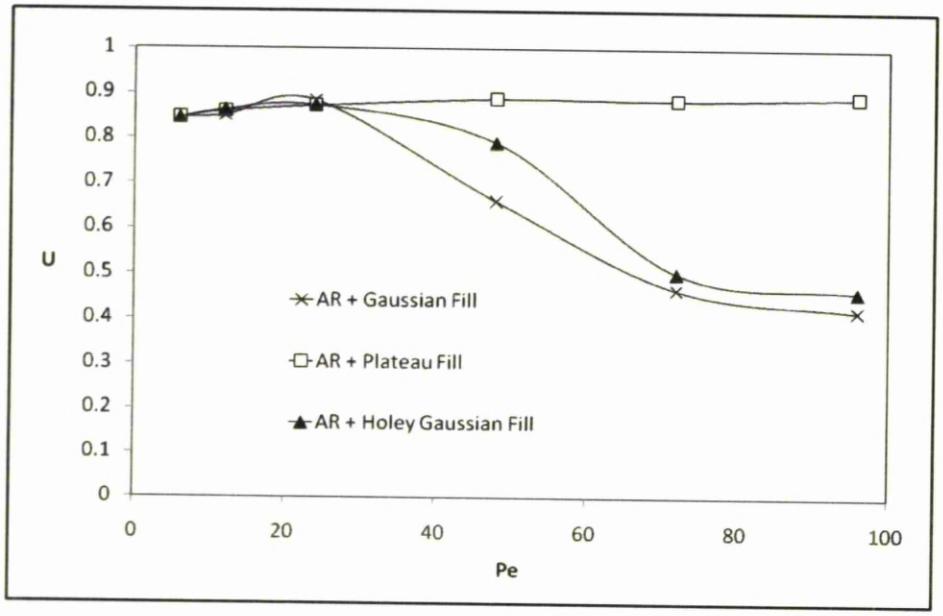

Figure 29: Uniformity vs. Péclet number for three different filled annular rings. As the Péclet number is increased, the size of each central intensity feature is increased to optimise the uniformity.

The Plateau fill clearly displays the best performance over the range of Péclet numbers shown in Figure 29. A fill of this type is therefore more desirable than the Gaussian or holey Gaussian features which have lower uniformities at higher Péclet numbers.

As yet uniformity has only been optimised at the surface using the plateau fill annular ring. As discussed earlier, a uniform *ΔTDP* at the surface does not give a uniform *ΔTDP* at a depth below the surface. To achieve uniformity at a depth beneath the surface the surface *ΔTDP* must be overheated at the outer edges. The size of the plateau fill should therefore be reduced from that used to optimise uniformity at the surface if uniformity is desired at a specific depth beneath the surface. Using a reduced plateau fill in the centre of the annular ring will cause the edges of the *ΔTDP* at the surface to become overheated but will increase uniformities at a given depth beneath the surface. The greater the depth at which uniformity is required, the greater degree of overheating required at the edges of the surface *ΔTDP*. This is illustrated in Figure 30 where the plateau fill has been adjusted to optimise uniformity at the surface and at two depths beneath the surface. The *ΔTDPs* at all three depths are given for each optimisation. Those overheated at the outer edges are highlighted in red; those overheated in the centre in blue; and those which are optimised at their given depth in black.

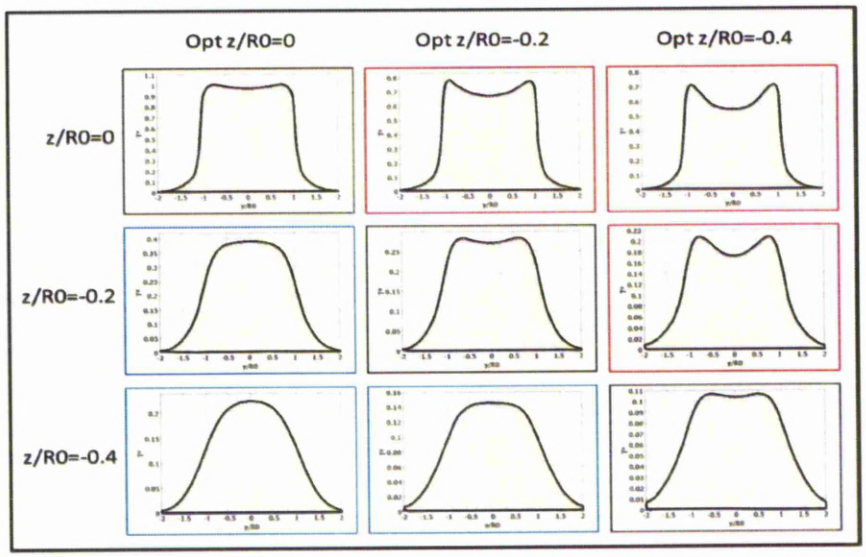

Figure 30: ΔTDP's at various dimensionless depths (z/R0) created using the plateau fill annular ring (at Pe=24).

The plateau fill can be adjusted to achieve optimal uniformities both at the surface and at various depths beneath the surface over a range of Péclet numbers. This is illustrated in Figure 31 to Figure 33 where the optimised uniformities at each depth are compared to those achieved at other depths using the same size of plateau fill. Each graph shows the both levels of uniformity achievable at a given depth and the level of sacrifice of uniformity which must be paid at the other depths.

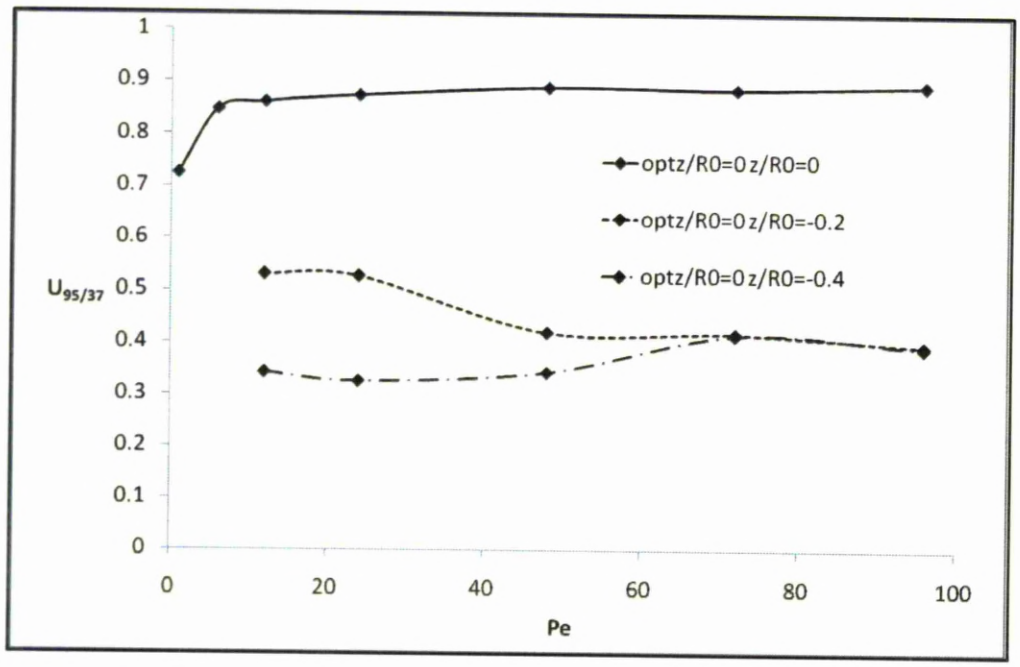

Figure 31: Uniformity vs. Péclet number optimised at the surface (z/R0=0)

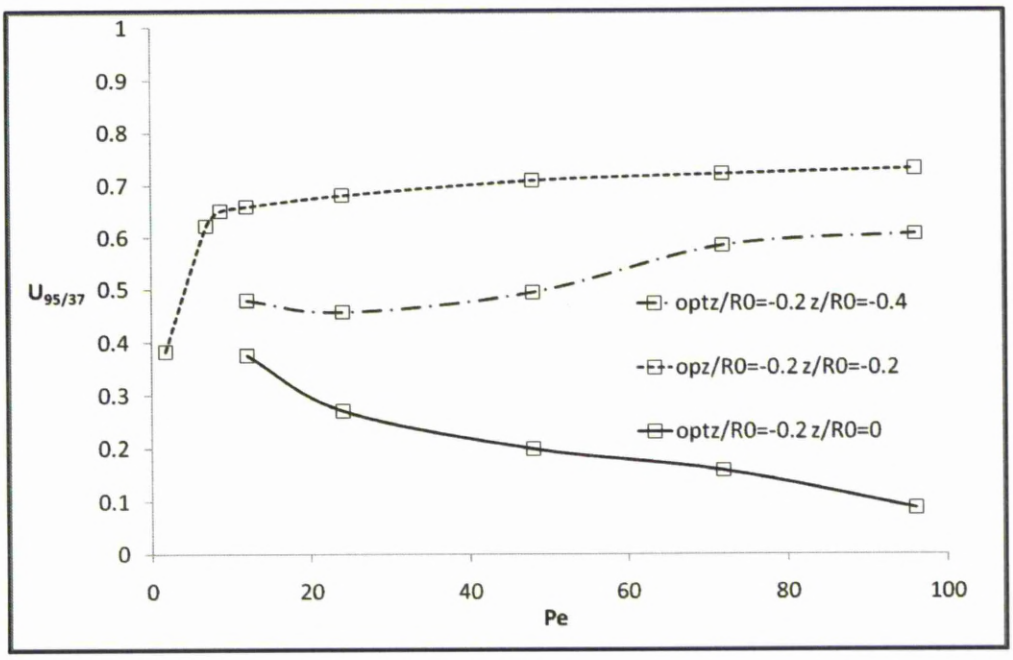

Figure 32: Uniformity vs. Péclet number optimised at z/R0=-0.2

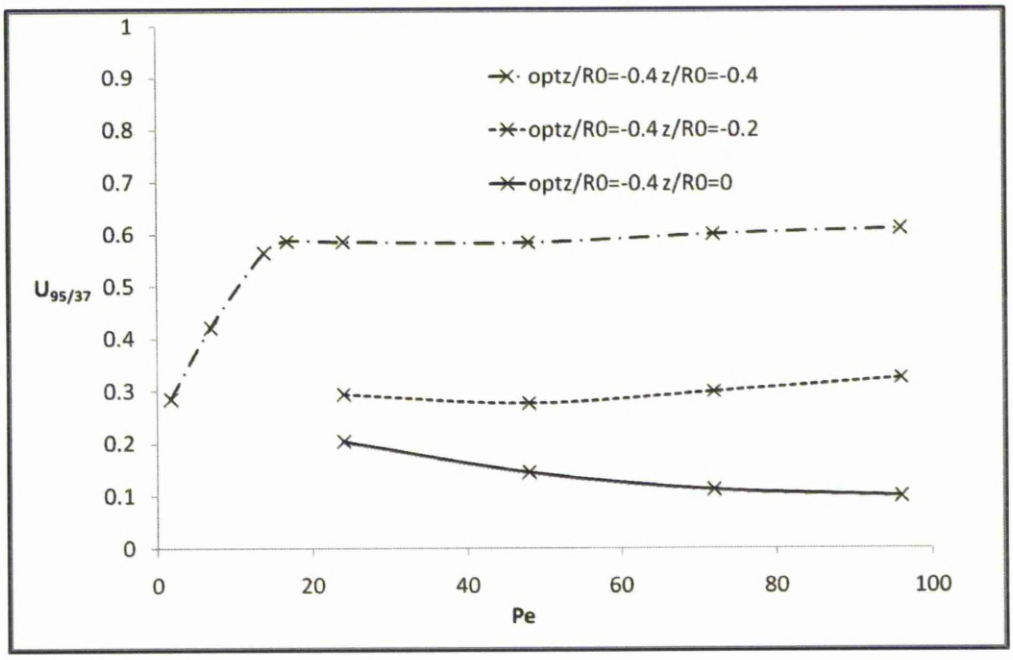

Figure 33: Uniformity vs. Péclet number optimised at z/R0=-0.4

It is clear from these results that optimising uniformity at multiple depths simultaneously may not be possible. The uniformity at depths higher than the depth which the optimisation is carried out for must be sacrificed by overheating the outer

edges, whereas uniformity at lower depths is sacrificed due to overheating in the centre of the treated area. Since most surface modification techniques require uniformity at some depth beneath the surface, it is quite likely that the optimum profile for that process will be one which causes overheating at the outer edges on the surface of the material.

The ratio of maximum intensity of the plateau fill compared with the annular ring is shown for each set of uniformities in Figure 31 to Figure 33.

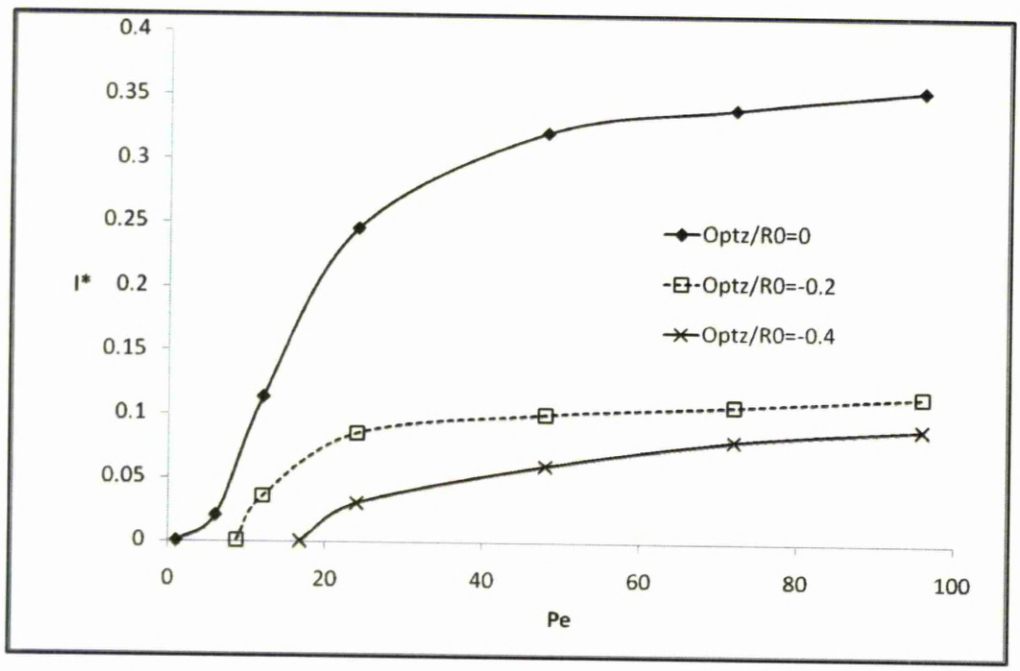

Figure 34: Ratio of plateau fill to annular ring maximum intensity vs. Péclet number for each of the depths for which uniformities were optimised for.

Now that uniformity in the maximum temperature reached has been achieved to a high level over a wide range of Péclet numbers at the surface and at depths below the surface, it is time to assess uniformity in the other temperature characteristics across the width of the treated area at the surface. This will be carried out by assessing the heating and cooling rates by studying the steady state temperature distribution in the x direction at various distances from the centre to the edge of the treated area. Since the Plateau filled annular ring has been most effective in achieving a uniform maximum temperature rise across the width of the treated area, it is the only intensity

profile to be investigated for uniformity in its temporal temperature characteristics. Adjustments[n] of the plateau-fill annular ring which were optimised for uniformity in the maximum temperature rise at the surface will be assessed for variation in heating and cooling rates across the width of the treated area.

The normalised steady state temperature distribution in the x-direction is taken at various distances from the centre of the treated area. The time dependence of this distribution is introduced by dividing the x-axis data by the traverse speed of the moving heat source which allows heating and cooling rates and other temporal temperature characteristics to be deduced. The time is then normalised by taking its ratio with a reference time of $t^*=R_0^2/\alpha$. A plot of this type is shown in Figure 35 for the plateau fill annular ring optimised for uniformity in the maximum temperature rise for *Pe=12*. y-displacements from the centre of the treated area shown in the key are shown as relative to the maximum radius R_0 of the moving heat source.

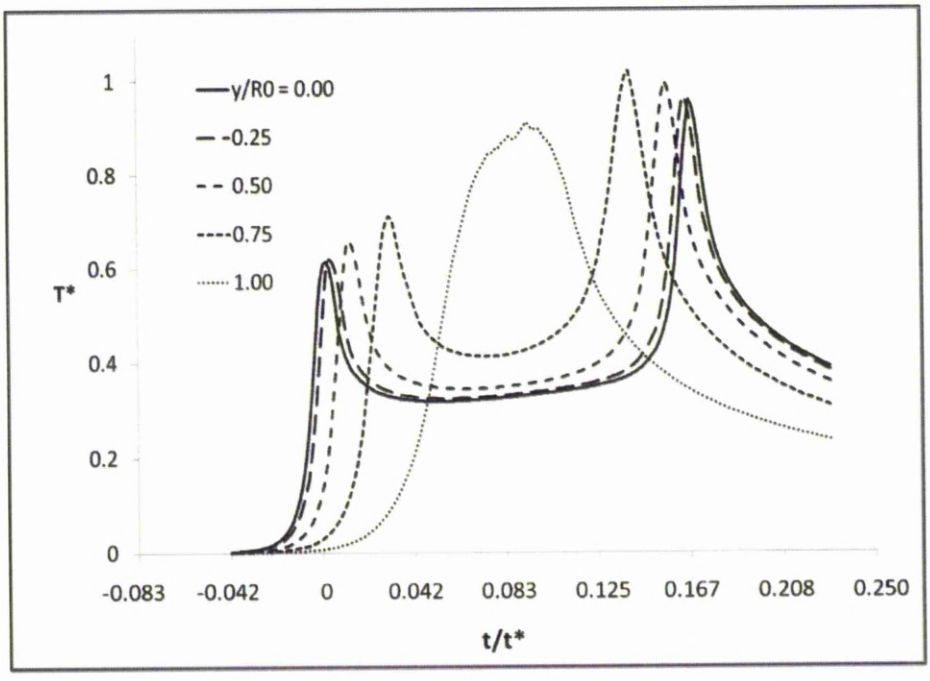

Figure 35: Temporal characteristics of the temperature distribution at various distances from the centre of the axis of movement for Pe=12.

[n] Adjustments refer to those of the relative maximum intensity of the annular ring and central feature

Although uniformity in the maximum temperature rise across the width of the treated area can be achieved to an extent using the plateau fill annular ring at this Péclet number, the heating and cooling characteristics are clearly very different between the edge and centre of the treated area. Central areas (e.g. 0.00<y<0.75) experience two stages of heating and cooling – the primary stage occurs as the first half of the heat source passes, with the main stage occurring after the centre of the heat source has passed and resulting in the material being brought up to its maximum temperature values. Peripheral areas (e.g. y=1.00) however experience only one prolonged heating and cooling stage. Furthermore the primary and main stage heating and cooling rates both reduce as the distance from the centre of the treated area is increased.

Similar plots are shown in Figure 36-Figure 39 for Péclet numbers 24, 48, 72 and 96.

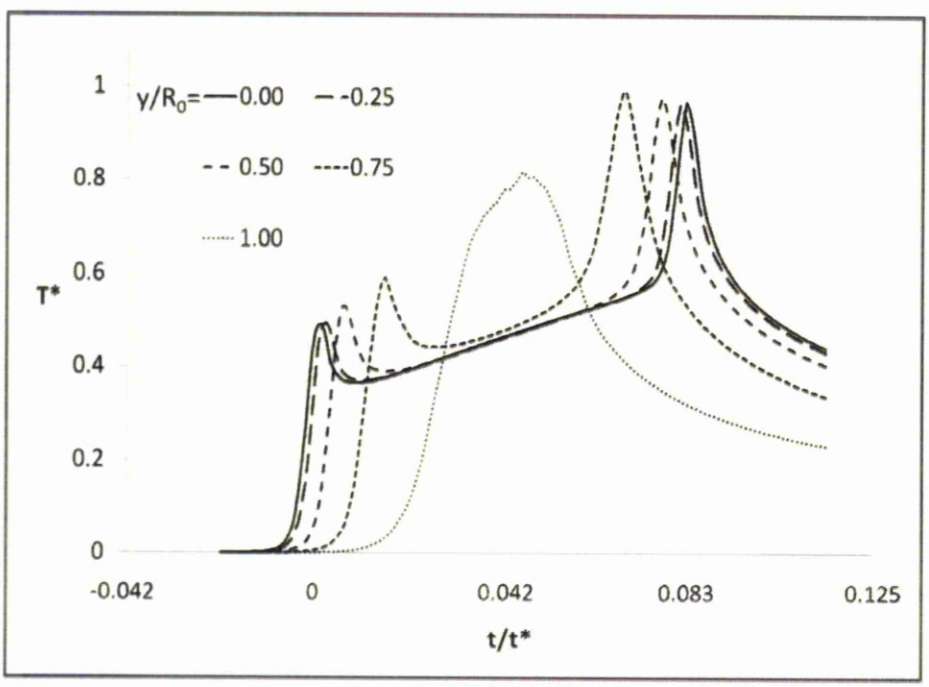

Figure 36: Temporal characteristics of the temperature distribution at various distances from the centre of the axis of movement for Pe=24.

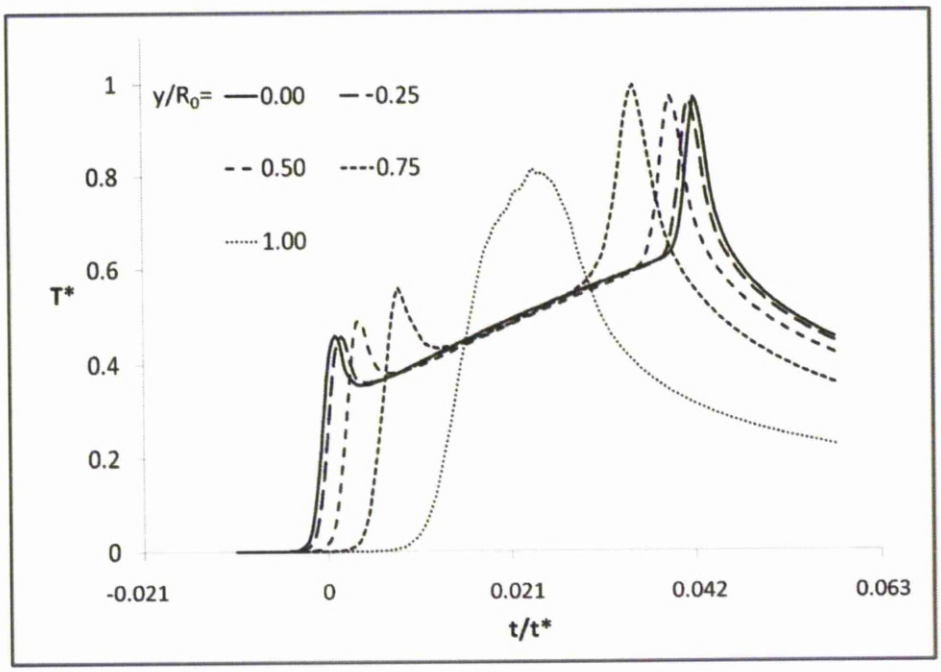

Figure 37: Temporal characteristics of the temperature distribution at various distances from the centre of the axis of movement for Pe=48.

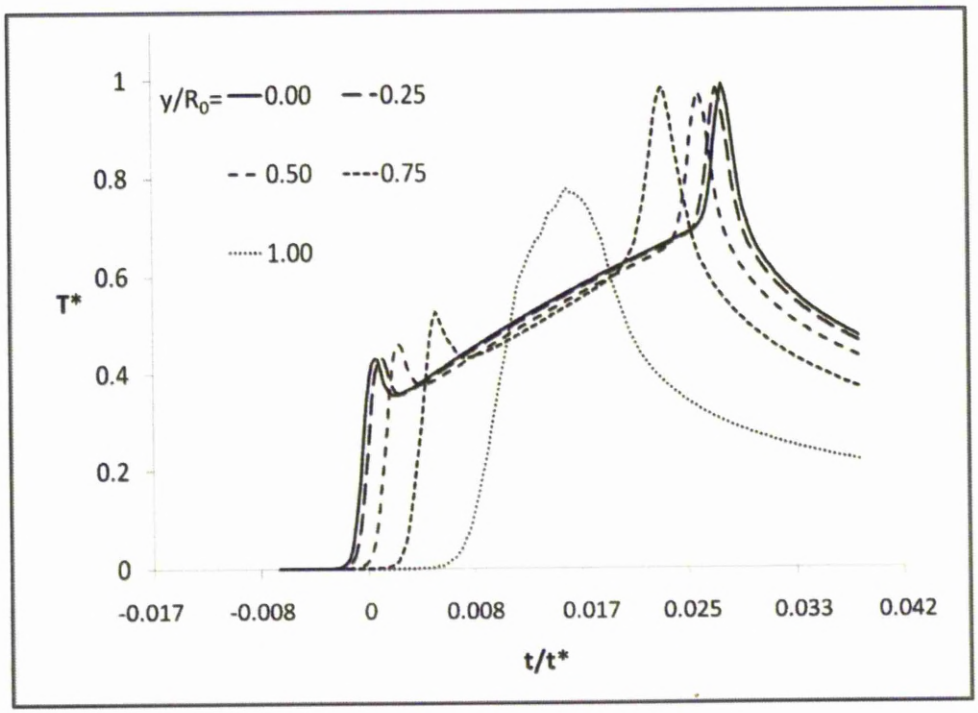

Figure 38: Temporal characteristics of the temperature distribution at various distances from the centre of the axis of movement for Pe=72.

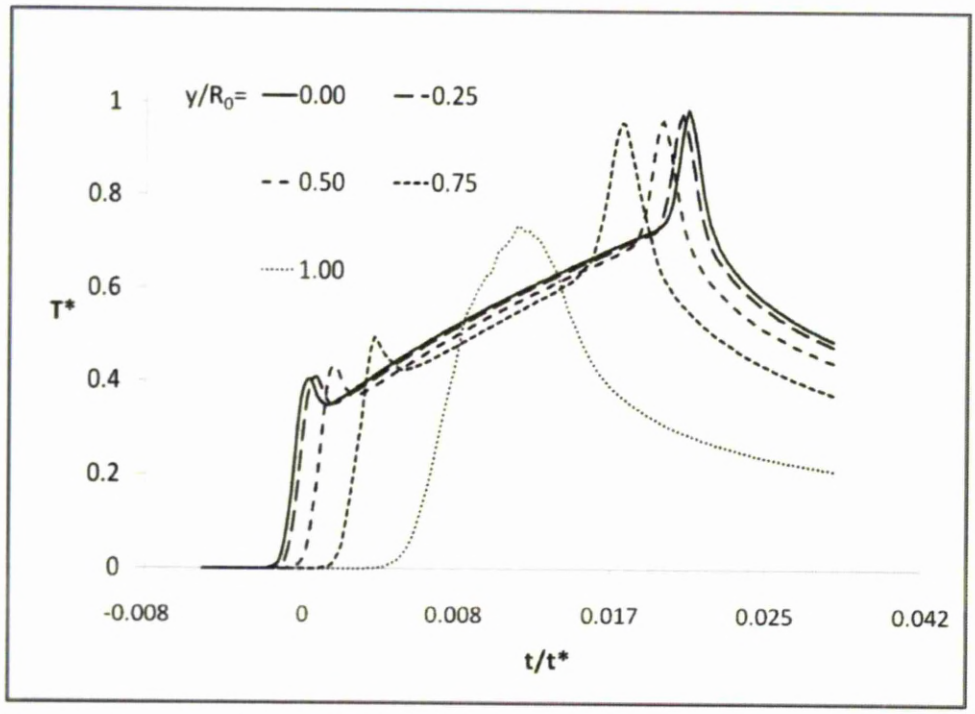

Figure 39: Temporal characteristics of the temperature distribution at various distances from the centre of the axis of movement for Pe=96.

The heating characteristics at higher Péclet numbers are similar to those shown in Figure 35 with a few key exceptions. As the Péclet number is increased and the level of fill in the centre of the annular ring is increased to compensate, the amount of cooling after the primary heating stage is reduced. The main heating stage also becomes less dramatic due to the increase in gradual heating between the two stages brought on by the higher intensity fill in the centre of the annular ring.

It is clear that high uniformity in the maximum temperature reached can be achieved over a wide range of Péclet numbers using a base annular ring with a variable central intensity feature. True uniformity in the heat treatment of surfaces however is not possible with a circular heat source. The heating and cooling characteristics across the width of the treated area differ too greatly and there is no way of mitigating for this. Although this is true, when considering the processing window for any application it is possible that a uniform effect can still be achieved using a circular heat source geometry. This may be unimportant for some applications where control of heating and cooling rates is not essential. However where they are essential, varying the

maximum temperature reached across the width of the treated area to compensate for the difference in heating and cooling rates may be a possible solution. By maintaining both edge and centre heating characteristics within the processing window (if it is large enough) achieving uniformity may be possible. For example heating the centre for longer (or causing a faster heating rate in the centre) at a lower maximum temperature may cause the same effect as heating the edge for a shorter period (or causing a slower heating rate at the edge) at a higher maximum temperature. This is merely conjecture however and clearly additional studies must be carried before any such conclusions can be validated.

2.6 Conclusions

There are several existing methods to heat treat a surface uniformly with a moving laser beam including using a rapidly scanning beam, using overlapping of adjacent passes of the beam and using various beam intensity profiles and geometries. By shaping the beam geometry the temperature distribution on the surface of a material can be controlled. A strip or line shaped geometry is shown by the literature to provide the most uniform maximum temperature rise and the most uniform change in the surface properties. By changing the orientation of the geometry a drastic change in the temperature distribution can be observed. For certain laser materials processing applications multidirectional or even omnidirectional processing may be desirable or even essential. The only heat source geometry capable of producing an effect which is independent of processing direction is a circle. The intensity profile within must also be circularly symmetric. Common problems arise when using a circularly symmetric heat source intensity profile to try to achieve a uniform temperature rise on the surface of a material. The reduced interaction time at the edge of the treated area must be compensated for by an increase in intensity toward the edges of the profile such as in an annular ring intensity profile. It has been shown that an annular ring with a low spread Σ is capable of achieving a uniform maximum temperature rise at low Péclet numbers and that increasing the spread of the annular ring can increase both the Péclet number and the Péclet number range for which the highest uniformities are achieved. Below the optimum Péclet number range for any

annular ring, the uniformity drops due to overheating in the centre of the *ΔTDP*. Above the optimum Péclet number range for any annular ring, the uniformity drops due to overheating at the edges of the *ΔTDP*. In order to achieve optimum uniformity in the maximum temperature rise at a depth below the surface however, the surface *ΔTDP* must be overheated at the edges.

Changes to the Péclet number have a drastic effect on the temperature distribution created by any fixed heat source intensity profile. Therefore any heat source intensity profile which is capable of creating a uniform maximum temperature rise at a given Péclet number will become ineffective if the Péclet number is altered. For laser surface treatments where uniformity is required this implies that if a different traverse speed is used other than that which the beam profile was designed for or if the material or material properties change between jobs or in during processing then the beam profile may become ineffective at completing its intended task. Therefore if any one laser system is to be effective over a wide range of traverse speeds or materials beam profile modulation capabilities must be built in to the beam delivery system. It has been shown that the optimum base on which to build a modulated beam intensity profile for uniform surface treatments is an annular ring with a small spread. This is due to the high uniformities achievable with such a profile at low Péclet numbers. A central intensity profile feature can then be added in measured quantity to compensate for the reduced thermal diffusion from the edges toward the centre of the treated area which occurs at higher Péclet numbers. It has been shown that the optimum central intensity feature addition is a plateau fill and that this type of intensity profile is capable of achieving a high uniformity in the maximum temperature reached across the width of the treated area across a wide range of Péclet numbers relevant to a large proportion of the target applications as per Ion et al's[91] chart (shown in section 2.1.3.8). The other central intensity feature additions tested - a Gaussian and a holey-Gaussian feature - were effective only in the low to mid Péclet number range. It was also shown that ensuring high uniformities at the surface results in lower uniformities at a depth beneath the surface and that to optimise uniformities at any depth below the surface, the *ΔTDP* must be overheated at the outer edges at the surface. The flexibility of a dynamic intensity profile such as a plateau fill annular

ring means it is possible not only to achieve overheating at the outer edges of the ΔTDP at the surface but also to control the level of overheating so that uniformity may be optimised at any given depth.

It has been shown that achieving uniformity with the plateau-fill annular ring in the maximum temperature has also led to a reasonable level of uniformity in the second of the three thermal history requirements, namely the relative amount of time spent above the threshold temperature. However the heating and cooling characteristics are so vastly different between the edge and the centre of the treated area that it cannot yet be said with any certainty that the dynamic plateau-fill intensity profile will be capable of achieving true uniformity in any real process.

3 Creating Dynamic Intensity Profiles by Laser Beam Shaping

3.1 Introduction

Beam shaping is the art and science of transforming the outline geometry and/or the intensity profile of a laser beam from one form to another. There are several methods of carrying out the transformation, all of which are based either on the principles of reflection, refraction, diffraction or a combination of these. Using any one of a variety of existing beam shaping methods it is theoretically possible to transform almost any conceivable input beam shape into any desired output beam shape. A sensible choice of beam shaping method for any beam shaping task is therefore generally not based on the shape or intensity profile of the desired output beam. In choosing a laser beam shaping method the influence of diffraction is the most important consideration. For beam shaping systems where diffraction effects are too great the beam shaping task becomes impossible, whereas for those where diffraction effects are small enough to be ignored the geometrical optics approximation can be used. The size of the diffraction effects for any beam shaping system can be determined with the radius of the input and output beams, the focal length of the focusing element° and the wavelength of the light passing through the system. This can be expressed as a dimensionless function β whose value will determine the likelihood that the geometrical optics approximation will produce accurate results.

$$\beta = \frac{2\sqrt{2\pi}w_{0in}r_{out}}{f\lambda} \qquad [31]$$

A high β will mean that the laws of geometrical optics will be a good approximation. Romero and Dickey[136] provide a rule of thumb for the value of β: for $\beta < 4$ a beam shaping system will not produce accurate results, for $4 < \beta < 32$ diffraction effects will be significant and should be factored into the design process and for $\beta > 32$ geometrical optics will be a good approximation. A caveat is that discontinuities in the first, second or third order derivatives of the surfaces of any of the optical elements will themselves introduce diffraction effects. Higher values of β will

° or the working distance from the surface of the last lens element for systems with no focussing element

therefore be needed for systems with such features in order for geometrical optics approximations to hold[136]. Other important considerations include the level of knowledge the designer has of the input beam, the reliability of the input beam and the amount of energy which the beam shaping system needs to be able to handle. For example if the input beam is unknown, unstable or likely to change in any way during normal operation then it is essential that a beam integrator is used over other methods. Refractive and diffractive methods rely on transmission of the beam through the optics and are therefore more susceptible to damage at higher laser powers than reflective optics.

A description of existing beam shaping techniques is now provided including a review of the state of the art for each technique.

3.2 Laser Beam Shaping Literature Review

3.2.1 Introduction

Laser beam shaping can be carried out either inside or outside the laser cavity. The transverse intensity profile of the raw beam created is categorised by laser 'mode'. A selection of laser modes categorised in by the TEM system is shown in Figure 40. The mode of a laser is a function of the size and shape of the laser optics (including any apertures) inside the cavity[137].

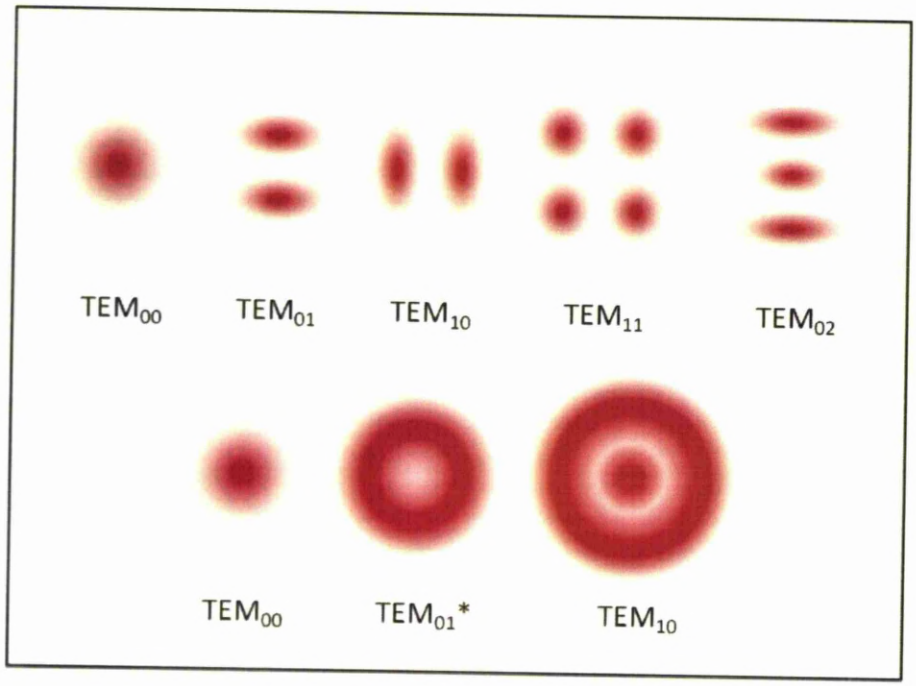

Figure 40: Hermite-Gaussian (top) and Laguerre-Gaussian Laser Modes

The design of a cavity optics system specifically for shaping the output beam intensity profile is reported by Pare and Belanger[138] where they use a graded-phase mirror to shape the wave front of the output beam. Forbes et al[126] build on Pare and Belanger's concept by designing a diffractive mirror whose shape can be modulated piezoelectrically to create the desired output beam. They report the use of the unimorph back mirror to enable selection of a flattened Gaussian mode inside the laser cavity. Tao and Yuan[139] report the use of a diffractive optical element to shape the output from the resonator into either a uniform circular beam or a ring shaped beam at a given distance outside the cavity.

Since the laser cavity itself can be fairly inaccessible and the laser often relatively expensive compared with the cost of a beam shaping system, it may seem unsurprising that the majority of laser beam shaping reported in the literature occurs outside the laser cavity. Beam shapers created for use outside the cavity can be designed and fabricated to be modular components of an overall laser system meaning that one laser can potentially be used to perform multiple tasks with or without the inclusion of any one of a number of laser beam shaping devices. The TEM_{00} mode is the output mode for the majority of lasers as it is the most useful mode

for many processes[21]. There are a great many and growing number of processes however that benefit from a uniformly illuminated beam. A large proportion of beam shapers have therefore been designed to shape a TEM_{00} (Gaussian) beam into uniformly illuminated beam with a square or circular beam geometry.

3.2.2 Intensity Apodisation

Intensity apodisation techniques can be used to shape the output intensity profile without affecting the phase front but at the cost of losing power in the output beam. In this case apodisation refers to the graduated attenuation of the input intensity profile in order to shape the output intensity profile. Karim et al[140] used a 2-dimensional binary filter configured with an image of the truncated input beam to create a coherent output beam with a uniform intensity across the central region. Earlier, Almarzouk[141] designed a binary filter to produce a uniform line shaped beam but with power losses of over 50%. Simmons et al[142] used both a glass rod and an electro-optic crystal within a radially varying magnetic field and an angled plane polariser to create smoothly varying transmission profiles to shape an input beam. Belvaux and Virdi [143] also designed a filter which produced a uniform profile but like other authors removed a considerable amount of energy (>60%) from the original beam due to the graduated attenuation of the beam power across the beam width.

3.2.3 Lossless Beam Shaping

The power losses incurred using intensity apodisation techniques may be trivial for some applications, however for processes where power losses and high inefficiency are unacceptable other techniques must be employed. The art of beam shaping with little or no power loss is known as lossless beam shaping.

Lossless beam shaping falls into two categories: field mapping and beam integration. Field mapping involves redistributing the input beam to form the desired intensity profile at an output reference plane whereas beam integration involves segmenting the input beam and recombining each segment at the output plane to form the desired intensity profile. Both techniques can be achieved using diffractive, reflective or refractive optics. Field mapping is best suited to situations where the input beam

intensity profile is constant and the output beam is required to be collimated. If the input intensity profile is unknown, fluctuates in time, or changes for any other reason during use of the system and the output beam is not required to be collimated, then field mapping is more suitable[136].

3.2.3.1 Geometrical Methods

One of the most popular and well reported lossless field mapping techniques involves using geometrical optics to design a combination of two aspheric lens surfaces to produce a collimated version of the desired output beam. Fermat's principle and the intensity law (explained later in section 3.4.2) are used in conjunction with the constant optical path length condition to shape any collimated input beam profile into a collimated output beam with the desired intensity profile. The first lens redistributes the intensity into the desired profile at the first surface of the second lens and the second lens then corrects the ray paths to collimate the output as shown in Figure 41.

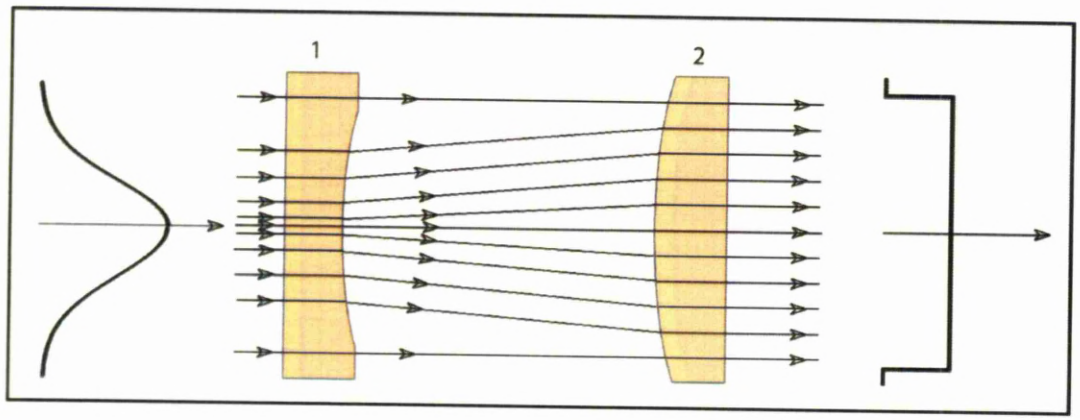

Figure 41: Schematic of a two lens refractive beam shaper designed using geometrical optics

It was Kreuzer[144] who originally patented this technique in 1969, his design transformed a Gaussian beam into a top-hat beam with no phase variation in the image plane. The design potentially could allow creation of any output beam given any input beam – a feature of the method remarked upon in Kreuzer's patent and by subsequent authors[136, 145]. Improvements and alterations to the design include two-surface single element systems[146] and systems based on spherical axial GRIN

(gradient of refractive index) lenses[147]. As a departure from the Keplarian design as seen in Figure 41, Hoffnagle and Jefferson[148] report a Galilean version with two convex surfaces designed using the same principles. A Galilean design is less expensive to manufacture due to the absence of any concave surfaces. Aspheric reflective systems also exist and perform much the same task using mirrored optics. McDermit and Horton[149] for example developed differential equations for the surfaces of one and two mirror beam shaping systems. They used the laws of reflection and differential radiant energy balance equations to arrive at the differential equations describing the appropriate gradient of the reflective surfaces. Reflective optics are considered to be better suited to high powered lasers than refractive optics which can be more susceptible to damage if overheated.

3.2.3.2 Beam Integrators

Multi-aperture beam integrators used for laser beam shaping are known as diffractive (or non-imaging) beam integrators and consist of an optical element split up into an array of smaller elements or lenslets followed by a focusing optic. The lenslets themselves can be diffractive, reflective or refractive and are generally designed with the same shape to simplify the manufacture of the lenslet array. The purpose of the focussing optic is to recombine the split beam elements on the target plane which is at the focal plane of the focusing optic. The resultant output intensity profile is the sum of the defocused[p] outputs from each lenslet in the array. A schematic representation of a diffractive beam integrator is shown in Figure 42.

[p] the lenslets themselves have their own optical power

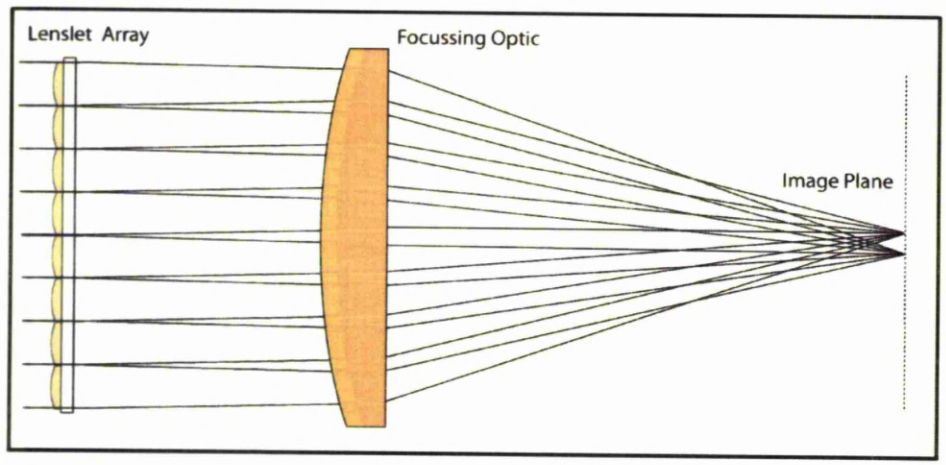

Figure 42: Multi-aperture diffractive beam integrator schematic

Beam integrators have the advantage of allowing an output intensity profile which is largely independent of the input intensity profile. This makes choice of this beam shaping method particularly suitable for multimode lasers such as excimer lasers and those in which the intensity profile varies in time due to mode instability[136]. For highly coherent beams the output intensity profile in a diffractive beam integrator can be calculated by considering both the diffraction pattern created by the individual micro-lens elements and the interference pattern created at the image plane due the overlap of images[136]. For many applications the intensity fluctuations caused by the interference of the overlapped beam portions is undesirable – this is highlighted for the case of laser surface treatments by Ocaña et al[150]. Weible et al[151] describe a method of smoothing the effects of interference in the far field (at the image plane) by generating a random design element to create a spatially random micro-lens array configuration. The design of diffractive beam integrators for partially coherent short wavelength beams, such as excimer laser beams, is possible by introducing a function which takes into account the degree of coherence across the beam whilst ignoring interference effects[152]. Multifaceted reflective beam integrators work on a similar principle to their refractive counterparts but the splitting and overlapping can be performed by a single element as reported by Dagenais et al[153]. Individual square flat facets whose centres are located on the inside of a sphere split the input beam and redirect the split portions to overlap at the image plane. Dagenais et al's design created a square shaped uniform intensity at the image plane but other beam

intensity profiles and geometries are certainly possible. Brown and Brown[154] for example point out some of the possibilities of using different lenslet shapes to create both hollow and multiple-spot output intensity profiles.

3.2.3.3 Diffraction Based Techniques

Diffractive field mapping (or Gaussian beam shaping) makes use of diffraction gratings in order to transform the phase, amplitude or polarisation of the input beam to create the desired output intensity and phase profile at the image plane. Complex diffraction gratings are created on an optical surface in the form of a split or multi-level surface relief. Intensity variation at the output plane is achieved in part by controlling the distribution of areas of constructive and destructive interference which is determined by the periodicity and gap size of the grating. Early diffraction based techniques were far from lossless with poor energy conversion efficiencies and it is only fairly recently that improvements in manufacturing technology have enabled diffractive optical elements to be fabricated with relatively high conversion efficiencies. The earliest use of diffractive techniques is recorded by Lee[155] where he used an iterative technique to develop a computer generated phase filter to shape an input Gaussian profile to a more uniform profile in 1 dimension but with a 15% loss in laser power. Veldkamp[156] reported the use of a binary diffraction grating and anamorphic beam compressor to reshape an input Gaussian beam into a flat-topped beam in one dimension with a 26% power loss. He commented on the potential that advances in grating fabrication would offer in terms of the ability of the technique to provide much greater control over the output intensity profile in more than one dimension. Aleksoff et al[157] reported the design of two holograph optical elements to transform an input Gaussian beam into a square uniform beam. Their design technique predicted maximum efficiency but manufacturing techniques used in the device fabrication were not well suited and experimental results showed low efficiencies (<30%). More recent examples of the use of diffractive optical elements have had greater success both in terms of conversion efficiency and the congruence of the output beam with that predicted in the model as well as the range of output intensity profiles created. Duparré et al[158] use computer modelling to design a diffractive optical element to shape a Gaussian input beam into a uniform intensity rectangle. They report a

theoretical efficiency of 100% and an experimentally achieved efficiency of 95% with good agreement between predicted and experimental output intensity profiles. Wang et al[159] report an experimentally obtained root mean squared percentage error of the top uniformity of less than 1.5% and an efficiency of over 96% with their integrated diffractive optical element. Modern diffractive optical elements are thinner and lighter than refractive or reflective components and can be used for high powered laser applications[160].

3.2.3.4 Dynamic Beam Shapers

Dynamic beam shapers are those which allow modulation of the output intensity profile by adjustment of the beam shaping optics in real time or between tasks. Crafer and Oakley[135] were among the first to suggest such a device in which a plano-convex lens is used in conjunction with a plano-conical (or Axicon) lens. A tightly focussed annular ring such as that shown in Figure 15 is created at the focal plane using their configuration. Beam profile modulation is achieved by moving the work piece in the z-direction. An outer half Gaussian annular ring (OHGAR) as described in section 2.5.1 is created by moving the image plane closer to the lens arrangement – the closer the image plane the greater the spread of the OHGAR. Although later withdrawn (Belanger and Rioux[161] had previously reported the configuration in their 1978 paper) their patent was still the first to suggest use of the profiles created with this configuration for different tasks. Schwede et al [162] provides a good summary of twin-spot laser beam shaping systems for laser welding including parabolic and split mirrors and refractive lenses. The relative power and position of the spots can be adjusted by moving the position of the optical elements relative to beam axis. Miyamoto and Maruo[8] developed their LSV (Linear-Polarised Shape Variable) optics to allow beam aspect-ratio modulation. They used cylindrical lenses, a pair of plate mirrors and a projection lens and were able to change the output intensity profile from an elliptical Gaussian to one where the x-profile is Gaussian and the y-profile is homogenous. Further alterations to the position of the components allowed the aspect ratio of the beam profile to be altered. They used the LSV design to control temperature distributions in surface transformation hardening and with it pioneered the laser joining of ceramics. Optical phased arrays or spatial light modulators are kinoform

diffractive optical elements capable of shaping an input intensity profile into almost any output intensity profile. As the optical phased arrays can be made with liquid crystal displays the output profile can be modulated in real time by rapid reconfiguration and optimisation of the diffraction pattern. Enguebard and Hatfield[163] report the use of such a device to create a complex intensity pattern which is rapidly optimised in real time by modulation of the diffraction pattern after feedback from an imaging system. In a much simpler design Passilli et al[164] use a variable diffraction slit created by two single-stepped optical elements which are configured to slide apart to create a method by which the output can be modulated in real time in 1-dimension only. The output profile is Gaussian in one dimension but can be modulated continuously between a Gaussian, a uniform and a hollow intensity profile in the other. The simplicity of the design means that although the design reported is for use with a wavelength of 532nm, a simple adjustment of the step height is all that is required for adaption to other wavelengths.

A dynamic beam shaper gives the advantage of being able to tune the output intensity profile and/or beam geometry to suit different processes. In the real world very often results obtained experimentally are different from those predicted in modelling or design stages – dynamic laser beam shapers give the process engineer a further degree of freedom to obtain the desired effect.

Dynamic intensity profile modulation in the case of this research is intended to allow a uniform maximum temperature rise on the surface of a material to be achieved over a wide range of Péclet numbers. It has been shown in Chapter 2 that intensity profile modulation is key to achieving this - the objective of this chapter is to obtain the required type and level of intensity profile modulation through novel optics design. The first section of this chapter will discuss a simple optical design consisting of an objective lens in combination with a 'sombrero lens' with a split section surface profile. Both inner and outer sections of the sombrero lens have conventional surfaces making its design possible using well known, basic lens equations and simple geometric constructions of the beam path. The lens is then manufactured and tested on a CO_2 laser system to provide proof of concept of the beam profile modulation mechanism. The subsequent section introduces the geometrical optics concepts

needed to develop the design, using instead an aspheric surface for the outer section which is essential for creating the plateau fill intensity feature in section 2.5.2. The design method is discussed in detail and a step by step methodology is provided for others to design their own device. An example is designed for use with a CO_2 laser and the output profiles are obtained for various input beam diameters in a ray tracing model. The same output profiles are then used in the heat transfer model as described in section 2.2 and a graph of the performance of the optics system is provided in the form of a uniformity vs. Péclet number plot.

3.3 Design of a Simple Prototype Optical System for Dynamic Beam Profile Modulation

3.3.1 Introduction

A prototype beam modulator for uniform surface heat treatments is now designed to shape a Gaussian input into an annular ring with a holey-Gaussian central intensity feature at the image plane. Modulation of the relative power of the central intensity feature compared with that of the annular ring is achieved by simply adjusting the input beam diameter. The design consists of an objective lens combined with a sombrero (split section Axicon/concave) lens and was designed for use with a collimated beam from a high powered CO_2 laser. The output profile at the image plane is optimised to produce the intensity profiles used to obtain the annular ring with holey-Gaussian results shown in section 2.5.2. The output profile was determined using basic lens equations, simple geometric constructions of the beam path and basic conservation of energy equations. The optimum output profile was obtained through trial and error at different input beam magnifications through an iterative process of adjusting various lens design parameters and testing the resultant output profile in COMSOL[98] as described in section 2.2. The prototype design for the sombrero lens has been manufactured by ULO Optics Ltd and a basic system is built for use with a high powered CO_2 laser. The output profile at various input beam magnifications is tested by taking beam prints in Perspex to provide verification of the effectiveness of the beam profile modulation mechanism.

3.3.2 The Design Concept

The prototype design consists of an objective plano-convex lens in combination with a sombrero lens with a circularly symmetric surface shape. The first surface of the lens is split into two concentric sections, the second surface is flat. The central section of the first surface is a shallow conic shape and is surrounded by a concentric outer section which is slightly concave. At the image plane the central section produces an FGAR (Full Gaussian Annular Ring) with a small spread and the outer section produces a holey-Gaussian feature (a Gaussian profile with the centre removed) within the annular ring. The purpose of designing and building the prototype is to provide proof of concept for the beam profile modulation mechanism. The modulation mechanism itself is simple: the relative intensity of the central intensity feature is controlled by the proportion of the beam which passes through the outer section of the sombrero lens. Thus to increase the relative intensity of the central feature, the input beam is expanded; to reduce its intensity, the input beam is contracted; and to eliminate it completely the beam is contracted further so that there is no significant power transmission through the outer section. The beam expansion can be carried out continuously by placing a zoom telescope before the objective lens. In the case of the system reported in the experimental section, the beam is expanded in stages using different combinations of lenses in a Keplarian telescope configuration.

3.3.3 Prototype Design Methodology

The basic lens equations and Rayleigh limit method for determining the output profile at the image plane is now described. The method makes one assumption which will affect the accuracy of the output profile predicted – that there are no diffraction effects in the holey-Gaussian feature at the image plane brought about by the discontinuity between the sections of the sombrero lens. The diffraction effects in the Rayleigh limit for the annular ring are taken into account however.

The images created by the outer and inner sections of the sombrero lens are dealt with separately in these calculations. The combination of the objective lens and the central Axicon section causes a focused annular ring to be formed at a focal distance determined primarily by the power of the objective lens. The peak-to-centre distance

of the annular ring at the focal plane is determined primarily by both the conic constant of the Axicon and the spacing between the objective and sombrero lens. The spread of the FGAR (full Gaussian annular ring) is determined by the diffraction limited spot size at the image plane. The combination of the objective lens and the outer section of the sombrero lens causes a defocused holey-Gaussian feature to be formed at the focal plane of the annular ring. The hole[q] radius at the image plane is determined by the combined power of the objective and outer section, the lens spacing and the radius of the central section. Since the objective and outer section of the sombrero lens have a longer combined focal length than the objective lens, the holey-Gaussian feature is outside of the Rayleigh limit when imaged at the focal plane of the annular ring. Thus a linear approximation can be made as to its spread and shape - in other words the profile can be approximated to be the same as that which enters the outer section of the sombrero lens, reduced in dimensions by a scale factor proportional to the image distance from the lens.

The intensity profile created by this arrangement can be shown in Figure 43. The parameters for each part of the intensity profile as labelled in Figure 43 are calculated in subsequent sections.

[q] in the holey-Gaussian feature

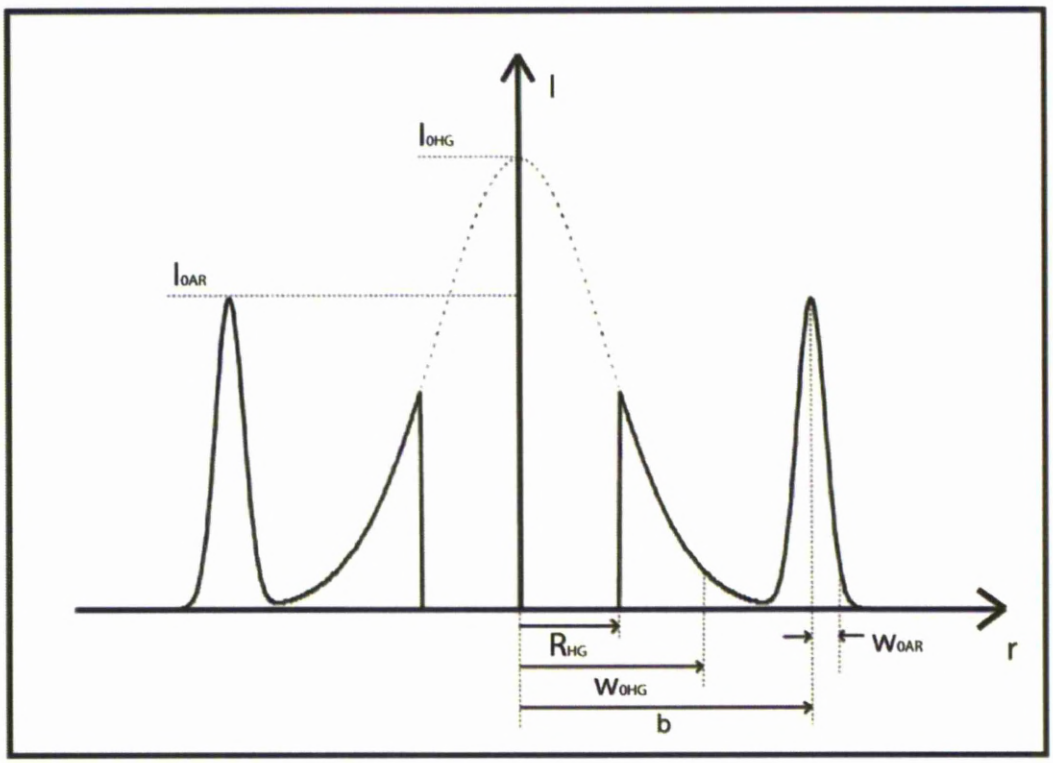

Figure 43: Intensity profile at image plane created by combination of the objective and sombrero lenses.

3.3.3.1 Method for Creating the Base Annular Ring Intensity Feature

For small Axicon angles θ_{AX} the annular ring radius b (peak to centre) can be approximated as follows:

$$b = u\theta_{AX}(n-1) \qquad [32]$$

Where u is the image distance determined by:

$$u = f_o - d - \tau_s \qquad [33]$$

Where f_o is the effective focal length of the objective lens, d is the separation between the objective and the sombrero lens and τ_s is the thickness of the sombrero lens. The spread of the FGAR w_{0AR} created at the image plane is limited by diffraction and is determined as follows:

$$w_{0AR} = \frac{2M^2\lambda f_0}{\pi r_{AX}} \quad [34]$$

Where M^2 refers to the divergence of the laser beam, λ is the wavelength of the laser light and r_{AX} is the radius of the aperture (i.e. the radius of the central section). This is similar to the diffraction limited spot size of a focussed single spot from a Gaussian beam with a factor of 2 to take account of the fact that the aperture is halved in an Axicon lens due to the discontinuity in the surface at the apex of the cone.

The intensity of the annular ring can be calculated using the principle of conservation of energy within a bundle of rays. Put simply, the total power entering the central section of the sombrero lens will be equal to the power contained within the annular ring at the image plane – the remainder of the power (passing through the outer section) will be equal to the power contained within the holey-Gaussian feature at the image plane.

Integrating the Gaussian function gives us the total power entering the objective lens

$$P_{IN}(\infty) = \frac{\pi I_{0IN} w_{0IN}^2}{2} \quad [35]$$

Appendix A contains its derivation.

The Gaussian intensity profile incident on the first surface of the second lens can be described by the same mathematical expression but with a smaller beam radius and subsequently, since there is no power loss, a higher maximum intensity.

The beam radius w_{0s} at this point can be approximated by:

$$w_{0s} = \frac{w_{0IN}(f_o - d)}{f_0} \quad [36]$$

The new maximum intensity at this surface I_{0s} can be found by remembering the energy conservation principle equating the total power of the input beam with the total power of the beam at the first surface of the second lens, therefore:

$$I_{0s} = \frac{2P_{IN}(\infty)}{\pi w_{0s}^2} \quad [37]$$

The Power $P(r_{AX})$ contained within a radius r_{AX} is given by:

$$P(r_{AX}) = 2\pi \int_0^{r_{AX}} I_{0s} e^{\left(\frac{-2r^2}{w_{0s}^2}\right)} r dr \quad [38]$$

$$P(r_{AX}) = \frac{\pi I_{0s} w_{0s}^2}{2}\left(1 - e^{\left(\frac{-2r_{AX}^2}{w_{0s}^2}\right)}\right) \quad [39]$$

The intensity distribution of an annular ring shaped beam can be shown as:

$$I_{AR}(r) = I_{0AR} e^{\left(\frac{-2(r-b)^2}{w_{0AR}^2}\right)} \quad [40]$$

Where $I_{AR}(r)$ is the intensity at a radius r from the centre of the profile, I_{0AR} is the maximum intensity of the annular ring, b is the offset of the maximum from the centre and w_{0AR} is the distance from b along r at which the intensity falls to $1/e^2$ (~13.5%) of its maximum value.

To find an expression for the total power under the annular ring the annular ring function must be integrated. This gives:

$$P_{AR}(\infty) = \frac{2\pi\sqrt{\pi} I_{0AR} w_{0AR} b}{\sqrt{2}} \quad [41]$$

Appendix B contains a full derivation of this integration.

Using the principle of the conservation of energy which equates the total power entering the central section of the sombrero lens with the total power in the annular ring, the maximum intensity of the annular ring is simply:

$$I_{0AR} = \frac{\sqrt{2} P(r_{AX})}{2\pi\sqrt{\pi} w_{0AR} b} \quad [42]$$

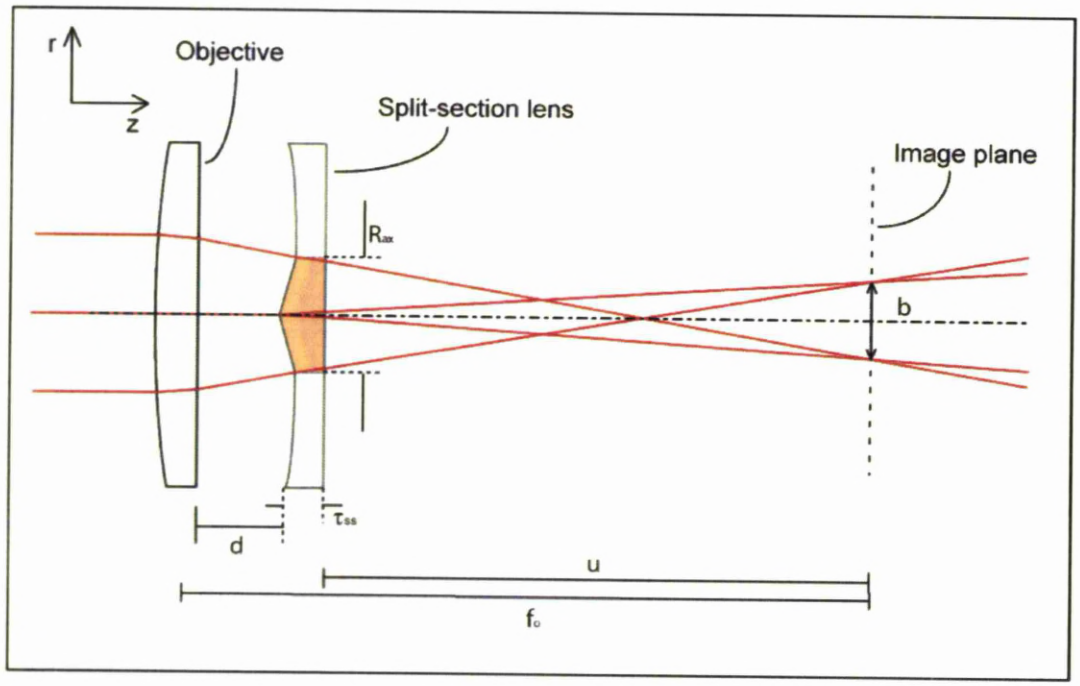

Figure 44: Formation of annular ring from objective and central section of sombrero lens.

3.3.3.2 Method for Creating the Holey-Gaussian Central Intensity Feature

The radius w_{0HG} of the holey-Gaussian is described as the radius at which the intensity falls to $1/e^2$ of the maximum intensity[r] and can be determined by calculating the combined focal length of the objective lens and concave outer section of the sombrero lens.

The focal length of any diverging or converging lens is given by the lens maker's formula:

$$\frac{1}{f} = (n-1)\left\{\frac{1}{R_1} - \frac{1}{R_2} + \frac{(n-1)\tau}{nR_1R_2}\right\} \qquad [43]$$

Where n is the refractive index of the glass at the relevant wavelength, τ is the thickness of the lens and R_1 & R_2 are the radii of curvature of the first and second surfaces respectively. In the case of the plano-concave outer section of the lens, the radius R_{2s} of the second surface is infinity and the focal length f_s can be expressed simply as:

[r] As if the feature was a full Gaussian with no hole removed

$$f_s = \frac{R_{1s}}{(n-1)} \quad [44]$$

The back focal distance *BFD* of the objective and outer section of the sombrero lens is given as:

$$BFD = \frac{f_s(d - f_0)}{d - (f_o + f_s)} \quad [45]$$

Where f_o and f_s are the focal lengths of the objective and sombrero lenses, *d*, is the distance between the second surface vertex of the first and first surface vertex of the second lens - the *BFD* is measured from the second surface of the combination lens. The focal positions of the annular ring and the holey-Gaussian will be separated by a distance *p* given by:

$$p = BFD - u \quad [46]$$

Since *p* is much larger than the Rayleigh range for this lens combination, the holey-Gaussian (HG) beam diameter and HG hole size will vary linearly with *p*. The HG beam width at the image position w_{0HG} will vary according to the beam diameter at the second lens w_{0S}, the *BFD* and *p* as follows:

$$w_{0HG} = \left(\frac{w_{0s}}{BFD}\right)p \quad [47]$$

The HG hole size r_{HG} will depend on both the *BFD* and the semi-diameter of the central Axicon region of the combination lens r_{AX}.

$$r_{HG} = \left(\frac{r_{AX}}{BFD}\right)p \quad [48]$$

A schematic of the dimensions used in the above calculations is shown in Figure 45.

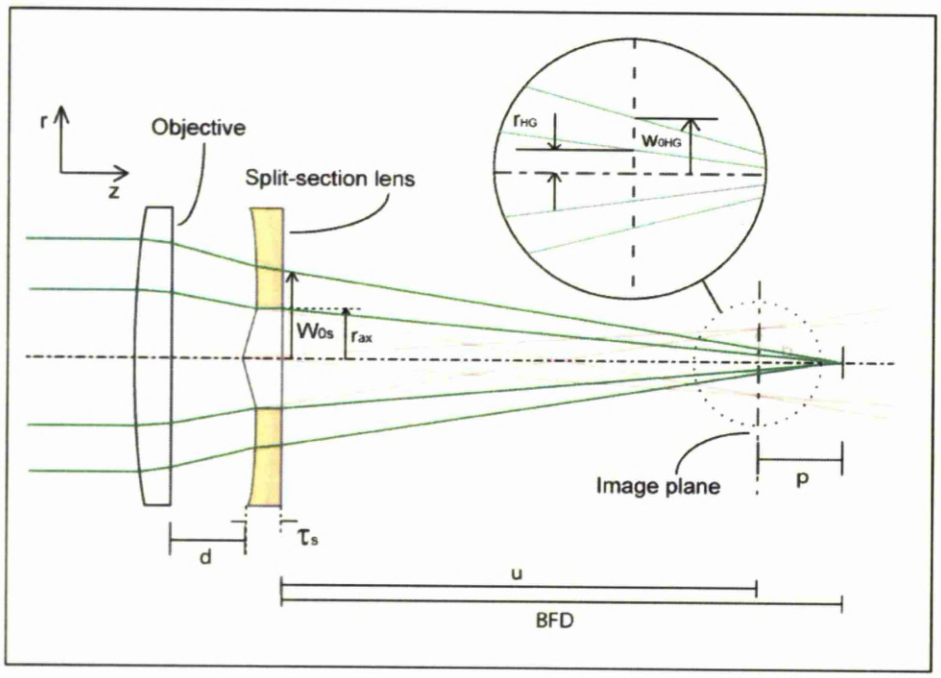

Figure 45: Schematic showing formation of holey-Gaussian feature from outer section of sombrero lens.

The power $P(r_{AX}, \infty)$ transmitted through the outer section is:

$$P(r_{AX}, \infty) = \frac{\pi I_{0s} w_{0s}^2}{2} e^{\left(\frac{-2r_{AX}^2}{w_{0s}^2}\right)} \quad [49]$$

Equating this with the power contained in the holey-Gaussian feature allows the maximum intensity of the holey-Gaussian feature[5] to be calculated, explicitly:

$$P(r_{AX}, \infty) = P(r_{HG}, \infty) \quad [50]$$

$$I_{0HG} = \frac{2P(r_{AX}, \infty)}{\pi w_{0HG}^2 e^{\left(\frac{-2r_{HG}^2}{w_{0HG}^2}\right)}} \quad [51]$$

The complete intensity profile can then be described by the following Boolean algebraic expression:

[5] This is the maximum intensity as if there were no hole removed as illustrated in Figure 43: Intensity profile at image plane created by combination of the objective and sombrero lenses.

$$I(r) = IF\left(r < r_{HG}, 0, I_{0HG}e^{\left(\frac{-2r^2}{w_{0HG}^2}\right)} + I_{0AR}e^{\left(\frac{-2(r-b)^2}{w_{0HG}^2}\right)}\right) \quad [52]$$

Which is a sum of the holey-Gaussian and annular ring intensity features at the image plane.

3.3.4 Design, Building and Testing of a Prototype Dynamic Beam Shaper for use with a CO_2 Laser

A prototype dynamic beam shaper now designed for use with a CO_2 laser using the calculations discussed in the previous section. A mathematical formula for the output beam was obtained in the form of equation [52] and input into the finite element modelling software used in the heat transfer analysis discussed in section 2.2. The lens design parameters were adjusted until the output profile gave the most uniform temperature rise across the width of the treated area. The final design was that which performed best over a range of Péclet numbers. There was a small element of compromise as the design which performed best at low Péclet numbers was not optimal at higher Péclet numbers and vice-versa. The final design was a compromise between the designs which performed best at both ends of the Péclet number range. It should be noted however that the compromise was minimal resulting in a decrease in uniformity values (at $U_{95/37}$) of no more than 2.5% at either end of the Péclet number scale tested.

A 2mm (peak to centre) annular ring was created from a Gaussian beam input by adjusting the angle of the Axicon central section of the lens according to equation [32]. Sensible values were chosen for the focal length of the objective lens, the lens spacing and the sombrero lens thickness to obtain a reasonable image plane distance. Next the semi-diameter of the central section and the surface radius of the outer section were adjusted to create the ideal properties of the holey-Gaussian feature at the focal plane of the annular ring. The spread of the annular ring will be governed by the semi-diameter of the central section. There is therefore a trade-off in choosing an appropriate semi-diameter for the central section. A sharp annular ring must be formed to give a steep side ΔTDP (by keeping the semi-diameter of the central section sufficiently large) whereas enough room must be left within the limits of the overall

lens diameter for a sufficiently large proportion of power to fill the centre of the annular ring at the highest intended Péclet number. Since the peak-to-centre width of the annular ring was decided first, the design constraints for creating the holey-Gaussian feature are restricted to the semi-diameter of the central section and the surface radius of the outer section of the sombrero lens. The other lens design parameters have been fixed in creating the annular ring or are fixed due to the characteristics and constraints of the CO_2 laser system the optics are designed for. The effect of adjusting r_{AX} is a proportional change in r_{HG} whereas adjusting R_{1S} affects both r_{HG} and w_{0HG} for any given input beam size. The effect of changing r_{AX} and R_{1S} on the relative size and shape of the holey-Gaussian feature compared with the annular ring is illustrated in Figure 46. The highlighted plot mid-centre (r_{AX}=*0.008m*, R_{1S}=*-2.8m*) shows the profile created by the design chosen after several iterations of lens design adjustments and finite element modelling of the output intensity profile at different Péclet numbers.

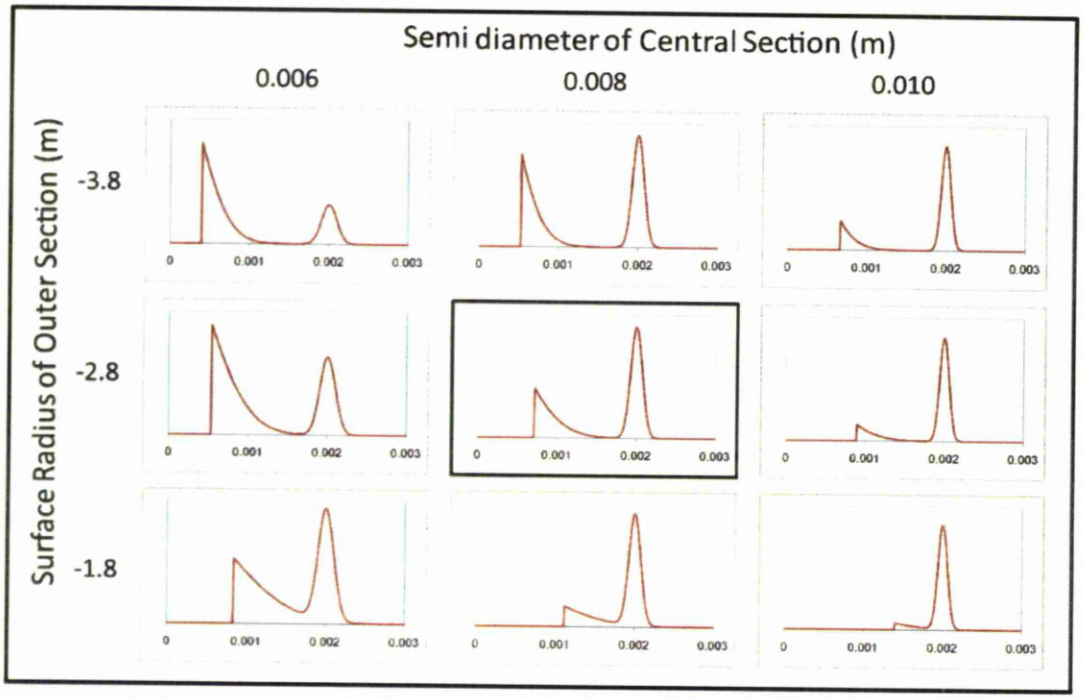

Figure 46: holey-Gaussian and annular ring features created using various sombrero lens design parameters. Individual plots show intensity (vertical axis) vs. radial distance from optical axis (horizontal axis).

The design parameters for the prototype lens system are shown in Table 1:

Table 1: Design parameters for prototype lens system

Parameter	Symbol	Value
objective focal length	f_o	190mm
semi-diameter of central section	r_{ax}	8mm
radius of curvature of outer section	R_{1s}	-2800mm
central section Axicon angle	θ_{ax}	0.008085rad
objective lens- sombrero lens separation	d	12mm
edge thickness of objective lens	τ_o	4mm
edge thickness of sombrero lens	τ_s	4mm
full semi-diameter of objective, sombrero lens	$D_o/2$, $D_s/2$	19mm
input beam radius range	w_{0in}	8-16mm

The intensity profile created by the chosen design can be modulated by adjusting the input beam diameter. Increasing the input beam diameter increases the proportion of the beam which passes through the outer section of the sombrero lens – this creates a higher intensity holey-Gaussian feature with a larger radius in the centre of the annular ring. Increasing the power of the holey-Gaussian feature in this way has benefits for uniform surface heat treatments. As discussed in chapter 2, use of an annular ring becomes problematic at higher Péclet numbers where the heat generated by the moving heat source dominates over the heat conduction within the material. This is compensated for by increasing the relative power of the holey-Gaussian feature. Figure 47 shows the output intensity profile as a function of the input beam diameter at the first surface of the sombrero lens.

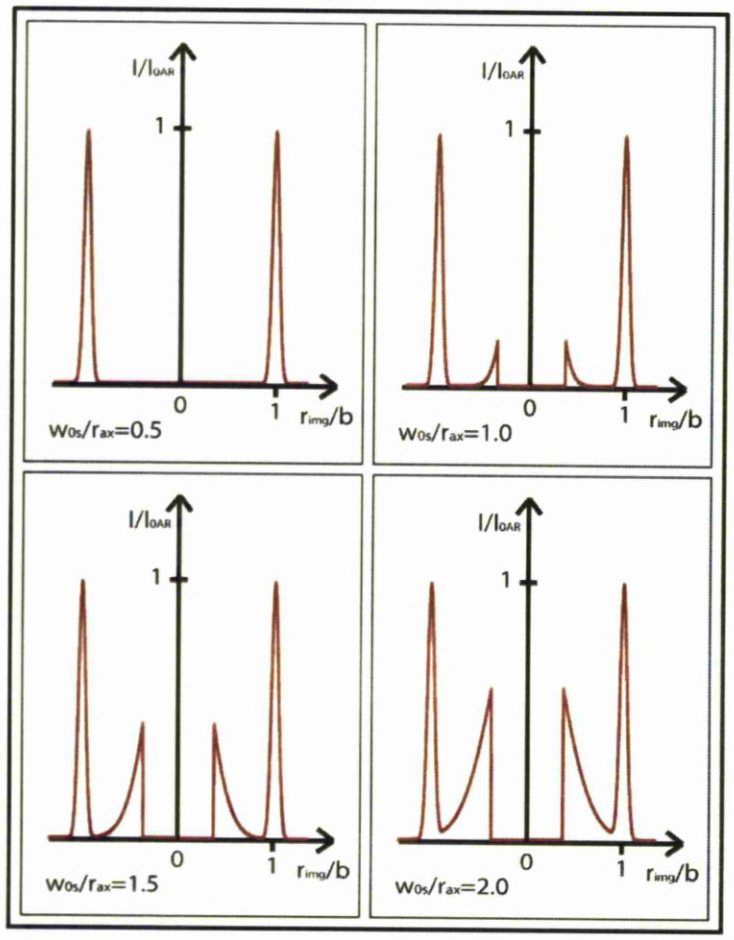

Figure 47: Intensity profile for various input beam radii (measured at r_{1s} relative to r_{AX})

The prototype design for the sombrero lens has been manufactured by ULO Optics, Stevenage, UK. The full system, including the input beam expander, was built with off-the-shelf lenses as well as a custom built prototype sombrero lens. The output beam profile was tested using 3 different input beam magnifications by taking beam prints in Perspex at the focal plane of the annular ring. The laser used was a 10.6 micron wavelength 1.5kW fast axial flow CO_2 laser operated at a reduced power of 300W. The output raw beam radius was measured by taking a deep beam print in Perspex. The dimensions of the print were taken using a micrometer and taken as the width from the centre at which the intensity fell to $1/e^2$ of its maximum value. The basic setup can be seen in Figure 48.

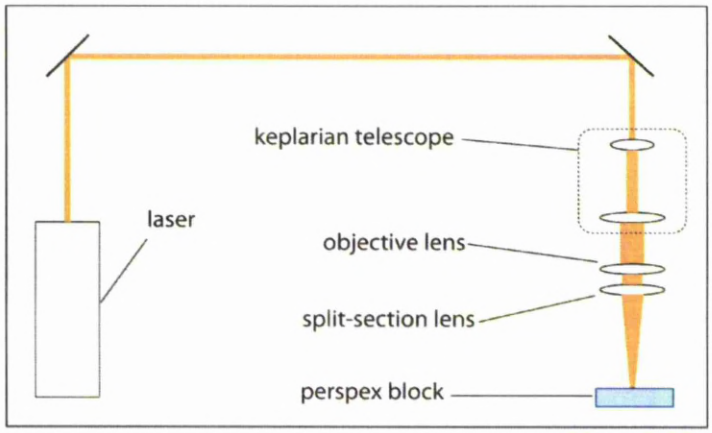

Figure 48: Basic experimental setup for assessment of the intensity profile by beam printing at the image plane.

It was essential to keep the beam collimated through the system before the objective lens as any significant divergence or convergence in the beam entering the objective/ sombrero lens combination would cause the output intensity profile at the image plane to become distorted.

The Keplarian telescope (Figure 49) was set up using two different combinations of lenses – a 50mm/75mm combination.

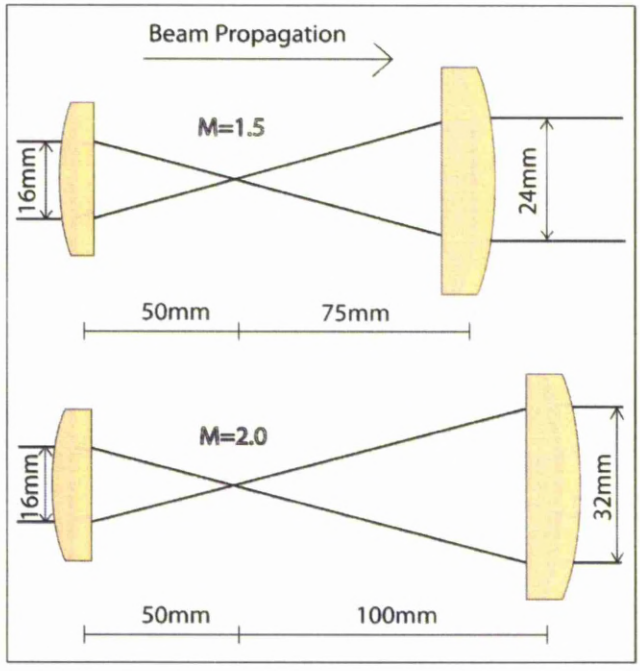

Figure 49: Two Keplarian telescope configurations used in prototype optical system.

This gave an input beam magnification of 1.5 and a 50mm/100mm combination giving a magnification of 2.0. The three input beam diameters tested were therefore 16mm (raw beam), 24mm and 32mm.

Beam prints were taken at the focal position of the annular ring 174.5mm from the second surface of the sombrero lens. Printing of the output intensity profile was carried out by manually pulsing the shutter to ensure a deep print in the Perspex whilst taking care not to scorch or ignite to reduce the possibility of printing distortions. The predicted and experimental output profiles are shown for comparison in Figure 50.

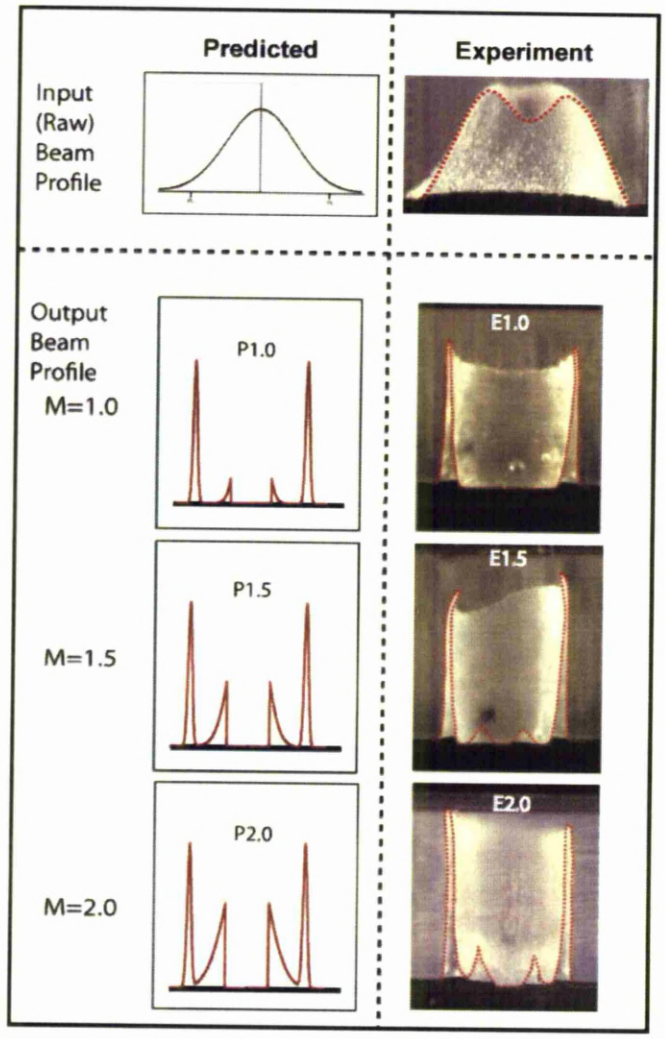

Figure 50: Experimental vs. predicted input and output beam profiles for the prototype optics design.

Although the input beam profile in the predicted output profile is a pure Gaussian shape, the input beam used to obtain the experimental results was mixed-mode as is shown at the top right hand side of Figure 50.

The beam prints clearly show that the relative size of the central feature can be adjusted simply by changing the diameter of the input beam. The absence of the central feature in E1.0 can be attributed to the difference in input beams. For both the input beams the definition of the beam width is the same (the point at which the intensity falls to $1/e^2$ of its maximum value) this implies that the only portion of the beam entering the outer portion of the lens is outside this point For the Gaussian beam used in the predictions this represents the point outside which falls around 11% of the total power whereas for the real beam used in the experiments this represents the point outside which a much smaller proportion of the total power exists. The difference in the maximum intensity of the holey-Gaussian feature can be explained by diffraction effects in the experimental results which were not accounted for in the calculations made in the predicted results.

A feature of this type of optical design is that the output intensity is a function of z as well as r as the output beam is not collimated. It is important therefore to control the z-position of the workpiece in order that the desired intensity profile is present on the surface of the material. Any image position other than that which is chosen in the design stage may therefore be undesirable for the purposes of uniform surface treatments. To illustrate this point and for the reader's interest Figure 51 shows the beam prints over 3 different input beam magnifications at two other image positions other than the one intended for use in uniform surface treatments.

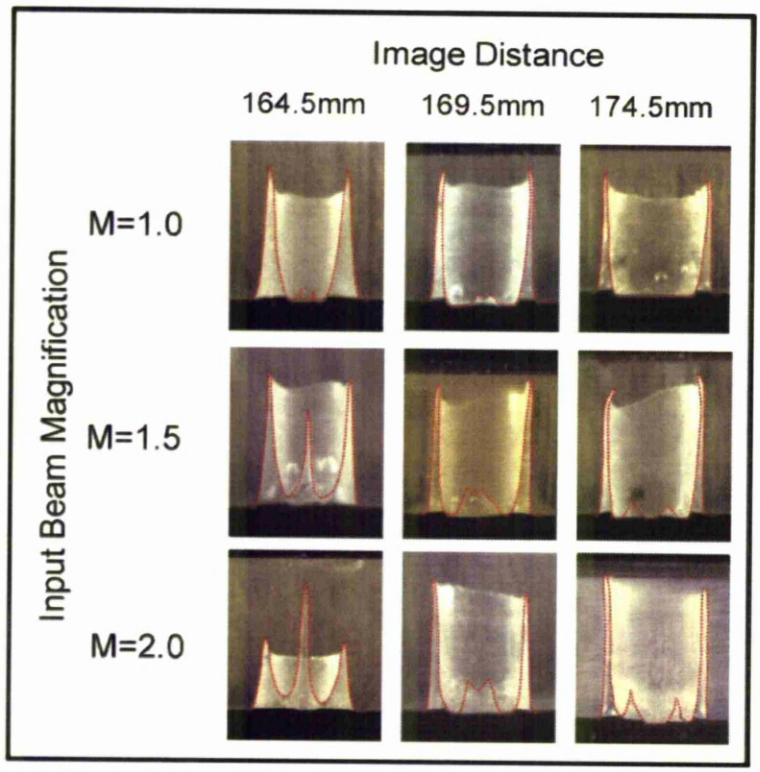

Figure 51: Effect on intensity profile at the image plane for different input beam magnifications when the image plane position is altered.

The size of the intensity feature in the centre of the annular ring can apparently also be altered at other image plane positions. The author will leave it open to readers to imagine applications for these slightly different profiles – and will comment only to say that they are less than optimal for uniform surface treatments.

3.4 Optimising the Dynamic Beam Shaper

3.4.1 Introduction

It has been shown that it is possible to create a base annular ring intensity profile into the centre of which another intensity feature can be added in controlled amounts by using an optical design of the type discussed in the preceding section of this chapter. The prototype optical system created a holey-Gaussian feature in the centre of the base annular ring profile which could be altered in size by altering the beam diameter entering the objective/sombrero lens combination. In the heat transfer section of this

thesis however it has already been concluded that the optimum central feature addition to the base annular ring is a plateau rather than holey-Gaussian fill. The holey-Gaussian feature does not adequately compensate for reduced influence of heat conduction at higher Péclet numbers. It may be possible to create a base annular ring with a plateau fill by altering the surface of the outer section of the sombrero lens.

3.4.2 Optical Theory

In this section the design of the outer section of the sombrero lens is optimised to give an annular ring with a plateau fill output. For the understanding of the methods used in the design process it is important to introduce a number of optics concepts, namely Fermat's principle and its relation to Snell's law, the intensity law and a detailed description of ray tracing through a two lens system.

3.4.2.1 Fermat's Principle and Snell's Law

Fermat's principle states that the path taken by light travelling between two points in space is the path which takes the least time. More specifically it is the path with the shortest optical path length. Using Fermat's principle it is possible to calculate the change in direction of a ray as is passes from one medium to another. The relationship between the speed of light in the two media and the angles of incidence and refraction is given by Snell's Law:

$$\frac{\sin\theta_1}{c_1} = \frac{\sin\theta_2}{c_2} \qquad [53]$$

More commonly found in the following form:

$$n_1 \sin\theta_1 = n_2 \sin\theta_2 \qquad [54]$$

Where c and n are the speed of light and the refractive indices respectively of the material and θ is the angle the ray makes with the surface normal.

3.4.2.2 The Intensity Law.

The principle of conservation of energy within a bundle of rays (known as the intensity law) is derived by Shealy and Chao[165] by expressing the optical field *u(**r**)* as a solution of the scalar wave equation as follows:

The optical field can be described as:

$$u(\mathbf{r}) = u_0(\mathbf{r})e^{ik_0 S(\mathbf{r})} \quad [55]$$

Where $k_0=\omega/c=2\pi/\lambda_0$ is the wave number in free space and $u_0(\mathbf{r})$ and $S(\mathbf{r})$ are the amplitude and waveform vectors respectively. For $u(\mathbf{r})$ to satisfy the scalar wave equation the following conditions must be satisfied:

$$(\nabla S)^2 = n^2 \quad [56]$$

$$2u_0 \nabla S \cdot \nabla u_0 + u_0^2 \nabla^2 S = 0 \quad [57]$$

Where *n* is the index of refraction. A unit vector **a** normal to the wave front specifying the direction of propagation of rays within a medium can be expressed as follows:

$$\mathbf{a} = \frac{\nabla S(\mathbf{r})}{|\nabla S(r)|} \quad [58]$$

As a consequence of equation [56] and rearranging equation [58] the following can be obtained:

$$\nabla S(r) = n\mathbf{a} \quad [59]$$

Now using the vector identity:

$$u_0 \nabla \cdot S + S \cdot \nabla u_0 = \nabla \cdot (u_0 \nabla S) \quad [60]$$

And using equation [59], equation [57] can now be written:

$$\nabla \cdot (u_0^2 n\mathbf{a}) = 0 \qquad [61]$$

The energy density (the square of the field amplitude) is equal to the product of the intensity *I* and the speed of propagation in the medium, therefore:

$$\nabla \cdot (I\mathbf{a}) = 0 \qquad [62]$$

Equation [62] is the intensity law for the propagation of energy and expresses the conservation of radiant energy within a bundle of rays, multiplying by the constant ($c/4\pi$) gives the correct units of *I*.

Integration of equation [62] over reference planes normal to the input and output beams and subsequently applying Gauss' theorem, the following is obtained:

$$I_1 dA_1 = I_2 dA_2 \qquad [63]$$

Where I_1 and I_2 are the intensities of the input and output beams respectively and the dA_1 and dA_2 represent infinitesimally small area elements on the input and output reference planes. A schematic representation of this is shown in Figure 52.

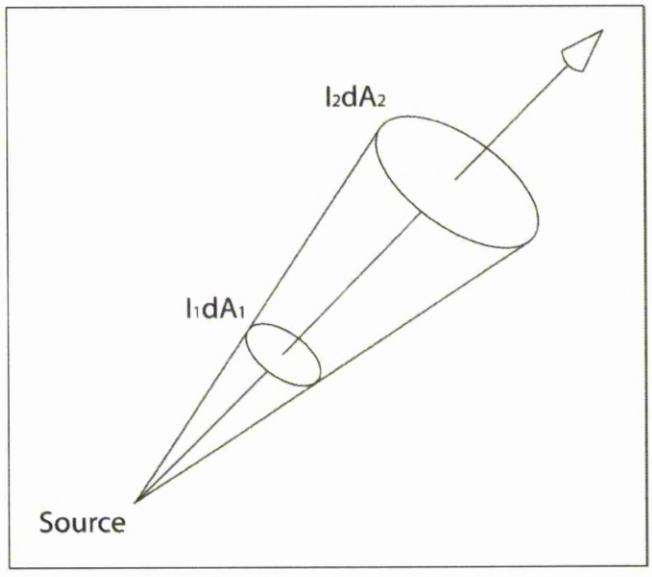

Figure 52: The Intensity Law as applied to geometrical optics.

This derivation is taken from Chapter V of Laser Beam Shaping and Techniques, reference [136].

For lossless beam shaping the intensity law can be applied to the total energy passing through the system by integrating over the input and output reference planes as follows:

$$2\pi \int_0^\infty I_{in} r dr = 2\pi \int_0^\infty I_{out} R dR \qquad [64]$$

3.4.2.3 Ray Tracing through the Two Lens System

Snell's Law can be applied at the surface of each component of an optical system to trace a ray of light as it passes through a system. Tracing a ray of light from an infinite source through an array of surfaces to an image plane is made fairly simple by the application of Snell's Law. If there are more than a few optical components ray tracing can be rather tedious however, hence why most optical engineers will use optical design software to complete ray tracing calculations. For the purposes of this research it is worthwhile showing analytically how the ray tracing calculations are carried out as this will assist in the understanding of some of the stages in the design process. Using Snell's law the angle of any ray with respect to the optical axis (and hence the rays displacement from the optical axis, known as the ray height) is recorded as it travels through a two lens system. A schematic of the path of a single ray is shown in Figure 53. Input ray height shown is rather arbitrary and serves only as an example to illustrate the angles and other measurements used in the calculations.

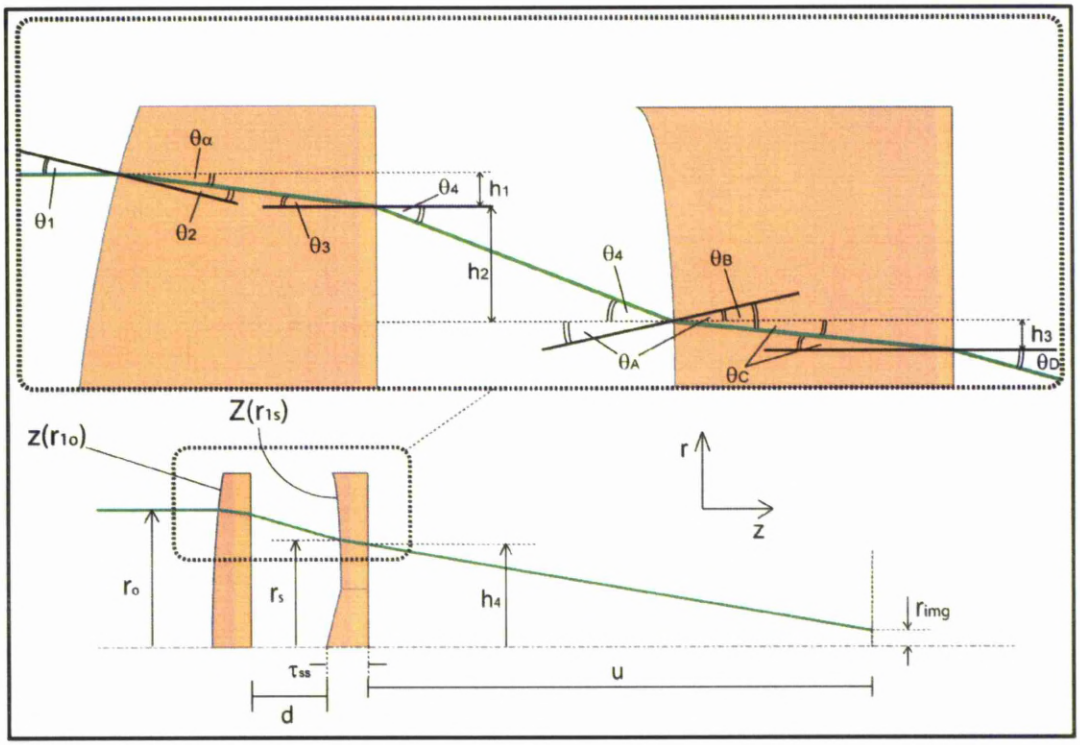

Figure 53: Ray tracing through a two lens system schematic.

The value of each of the angles shown in Figure 53 can be calculated using trigonometry and by using Snell's law. The convention chosen here is that the angle is positive where it is swept out by the ray or normal in the anticlockwise direction relative to the horizontal. z is positive from right to left. The angles in Figure 53 can be written in terms of the surface gradients of $z(r_{1o})$ and $Z(r_{1s})$, the refractive index n of the lens material, the lens spacing d and the lens thicknesses τ_o and τ_s.

The incoming ray meets the first surface of the objective lens parallel to the optical axis. The angle θ_1 is simply the angle the normal of surface $z(r_{1o})$ makes with the horizontal:

$$\theta_1 = \tan^{-1}\left(\frac{dz(r_{1o})}{dr_{1o}}\right) \qquad [65]$$

θ_2 is found from θ_1 using Snell's Law:

$$\theta_2 = \sin^{-1}\left\{\frac{1}{n}\sin\left[\tan^{-1}\left(\frac{dz(r_{1o})}{dr_{1o}}\right)\right]\right\} \quad [66]$$

θ_3 is found by subtracting θ_2 from θ_1:

$$\theta_3 = \tan^{-1}\left(\frac{dz(r_{1o})}{dr_{1o}}\right) - \sin^{-1}\left\{\frac{1}{n}\sin\left[\tan^{-1}\left(\frac{dz(r_{1o})}{dr_{1o}}\right)\right]\right\} \quad [67]$$

θ_4 is found from θ_3 using Snell's Law:

$$\theta_4 = \sin^{-1}\left[n\sin\left(\tan^{-1}\left(\frac{dz(r_{1o})}{dr_{1o}}\right) - \sin^{-1}\left\{\frac{1}{n}\sin\left[\tan^{-1}\left(\frac{dz(r_{1o})}{dr_{1o}}\right)\right]\right\}\right)\right] \quad [68]$$

Similar to θ_1 the angle θ_A is simply the angle the normal of surface $Z(r_{1s})$ makes with the horizontal:

$$\theta_A = \tan^{-1}\left(\frac{dZ(r_{1s})}{dr_{1s}}\right) \quad [69]$$

θ_B is found using Snell's Law after combining θ_A and θ_4 and remembering that the sign convention requires that θ_4 be subtracted from θ_A:

$$\theta_B = \sin^{-1}\left(\frac{1}{n}\sin\left\{\sin^{-1}\left[n\sin\left(\tan^{-1}\left(\frac{dz(r_{1o})}{dr_{1o}}\right) - \sin^{-1}\left\{\frac{1}{n}\sin\left[\tan^{-1}\left(\frac{dz(r_{1o})}{dr_{1o}}\right)\right]\right\}\right)\right] - \tan^{-1}\left(\frac{dZ(r_{1s})}{dr_{1s}}\right)\right\}\right) \quad [70]$$

θ_C can be found by adding (due to the sign convention) θ_A and θ_B:

$$\theta_C = \sin^{-1}\left(\frac{1}{n}\sin\left\{\sin^{-1}\left[n\sin\left(\tan^{-1}\left(\frac{dz(r_{1o})}{dr_{1o}}\right) - \sin^{-1}\left\{\frac{1}{n}\sin\left[\tan^{-1}\left(\frac{dz(r_{1o})}{dr_{1o}}\right)\right]\right\}\right)\right] - \tan^{-1}\left(\frac{dZ(r_{1s})}{dr_{1s}}\right)\right\}\right) + \tan^{-1}\left(\frac{dZ(r_{1s})}{dr_{1s}}\right) \quad [71]$$

θ_D is found from θ_C, again using Snell's Law:

$$\theta_D = \sin^{-1}\left\{n\sin\left[\sin^{-1}\left(\frac{1}{n}\sin\left\{\sin^{-1}\left[n\sin\left(\tan^{-1}\left(\frac{dz(r_{1o})}{dr_{1o}}\right)\right.\right.\right.\right.\right.$$
$$\left.\left.\left.\left.\left.-\sin^{-1}\left\{\frac{1}{n}\sin\left[\tan^{-1}\left(\frac{dz(r_{1o})}{dr_{1o}}\right)\right]\right\}\right)\right] - \tan^{-1}\left(\frac{dZ(r_{1s})}{dr_{1s}}\right)\right\}\right)$$
$$\left.+\tan^{-1}\left(\frac{dZ(r_{1s})}{dr_{1s}}\right)\right]\right\}\sin^{-1}\left\{n\sin\left[\sin^{-1}\left(\frac{1}{n}\sin\left\{\sin^{-1}\left[n\sin\left(\tan^{-1}\left(\frac{dz(r_{1o}}{dr_{1o}}\right.\right.\right.\right.\right.\right. \quad [72]$$
$$\left.\left.\left.\left.\left.-\sin^{-1}\left\{\frac{1}{n}\sin\left[\tan^{-1}\left(\frac{dz(r_{1o})}{dr_{1o}}\right)\right]\right\}\right)\right] - \tan^{-1}\left(\frac{dZ(r_{1s})}{dr_{1s}}\right)\right\}\right)$$
$$\left.+\tan^{-1}\left(\frac{dZ(r_{1s})}{dr_{1s}}\right)\right]\right\}$$

The heights h_1, h_2, h_3 and h_4 in Figure 53 can be calculated with the angles given above using trigonometry and the dimensions shown in the same figure.

$$h_1 = z(r_{1o})\tan\left(\tan^{-1}\left(\frac{dz(r_{1o})}{dr_{1o}}\right) - \sin^{-1}\left\{\frac{1}{n}\sin\left[\tan^{-1}\left(\frac{dz(r_{1o})}{dr_{1o}}\right)\right]\right\}\right) \quad [73]$$

$$h_2 = \left(d + \tau_s - Z(r_{1s})\right)\tan\left\{\sin^{-1}\left[n\sin\left(\tan^{-1}\left(\frac{dz(r_{1o})}{dr_{1o}}\right)\right.\right.$$
$$\left.\left.-\sin^{-1}\left\{\frac{1}{n}\sin\left[\tan^{-1}\left(\frac{dz(r_{1o})}{dr_{1o}}\right)\right]\right\}\right)\right]\right\} \quad [74]$$

$$h_3 = Z(r_{1s})\tan\left[\sin^{-1}\left(\frac{1}{n}\sin\left\{\sin^{-1}\left[n\sin\left(\tan^{-1}\left(\frac{dz(r_{1o})}{dr_{1o}}\right)\right.\right.\right.\right.$$
$$\left.\left.\left.\left.-\sin^{-1}\left\{\frac{1}{n}\sin\left[\tan^{-1}\left(\frac{dz(r_{1o})}{dr_{1o}}\right)\right]\right\}\right)\right]\right. \quad [75]$$
$$\left.\left.-\tan^{-1}\left(\frac{dZ(r_{1s})}{dr_{1s}}\right)\right\}\right) + \tan^{-1}\left(\frac{dZ(r_{1s})}{dr_{1s}}\right)\Bigg]$$

$$h_4 = u\tan\left(\sin^{-1}\left\{n\sin\left[\sin^{-1}\left(\frac{1}{n}\sin\left\{\sin^{-1}\left[n\sin\left(\tan^{-1}\left(\frac{dz(r_{1o})}{dr_{1o}}\right)\right.\right.\right.\right.\right.$$
$$\left.\left.\left.\left.\left.-\sin^{-1}\left\{\frac{1}{n}\sin\left[\tan^{-1}\left(\frac{dz(r_{1o})}{dr_{1o}}\right)\right]\right\}\right)\right]\right. \quad [76]$$
$$\left.\left.\left.-\tan^{-1}\left(\frac{dZ(r_{1s})}{dr_{1s}}\right)\right\}\right) + \tan^{-1}\left(\frac{dZ(r_{1s})}{dr_{1s}}\right)\right]\right\}\Bigg)$$

The height of any ray at the image plane r_{img} can be calculated as a function of the height of the input ray r_o. The position of the ray at the image plane can be calculated using:

$$r_{img} = r_o + h_1 + h_2 + h_3 + h_4 \quad [77]$$

Since it is predicted that the lens thickness variation will only differ by less than 2 % for the combination lens, the expressions for h_2 and h_3 can be simplified as:

$$h_2 = d\tan\left\{\sin^{-1}\left[n\sin\left(\tan^{-1}\left(\frac{dz(r_{1o})}{dr_{1o}}\right)\right.\right.\right.$$
$$\left.\left.\left.-\sin^{-1}\left\{\frac{1}{n}\sin\left[\tan^{-1}\left(\frac{dz(r_{1o})}{dr_{1o}}\right)\right]\right\}\right)\right]\right\} \quad [78]$$

$$h_3 = \tau_s\tan\left[\sin^{-1}\left(\frac{1}{n}\sin\left\{\sin^{-1}\left[n\sin\left(\tan^{-1}\left(\frac{dz(r_{1o})}{dr_{1o}}\right)\right.\right.\right.\right.$$
$$\left.\left.\left.\left.-\sin^{-1}\left\{\frac{1}{n}\sin\left[\tan^{-1}\left(\frac{dz(r_{1o})}{dr_{1o}}\right)\right]\right\}\right)\right]\right\}\right)\right] \quad [79]$$
$$\left.-\tan^{-1}\left(\frac{dZ(r_{1s})}{dr_{1s}}\right)\right\}\right) + \tan^{-1}\left(\frac{dZ(r_{1s})}{dr_{1s}}\right)\Bigg]$$

Therefore:

$$r_{img}$$
$$= r_o + z(r_{1o})\tan\left(\tan^{-1}\left(\frac{dz(r_{1o})}{dr_{1o}}\right) - \sin^{-1}\left\{\frac{1}{n}\sin\left[\tan^{-1}\left(\frac{dz(r_{1o})}{dr_{1o}}\right)\right]\right\}\right)$$
$$+ d\tan\left\{\sin^{-1}\left[n\sin\left(\tan^{-1}\left(\frac{dz(r_{1o})}{dr_{1o}}\right) - \sin^{-1}\left\{\frac{1}{n}\sin\left[\tan^{-1}\left(\frac{dz(r_{1o})}{dr_{1o}}\right)\right]\right\}\right)\right]\right\}$$
$$+ \tau_s\tan\left[\sin^{-1}\left(\frac{1}{n}\sin\left\{\sin^{-1}\left[n\sin\left(\tan^{-1}\left(\frac{dz(r_{1o})}{dr_{1o}}\right)\right.\right.\right.\right.$$
$$\left.\left.\left.\left.-\sin^{-1}\left\{\frac{1}{n}\sin\left[\tan^{-1}\left(\frac{dz(r_{1o})}{dr_{1o}}\right)\right]\right\}\right)\right]\right\}\right)\right] - \tan^{-1}\left(\frac{dZ(r_{1s})}{dr_{1s}}\right)\right\}\right) \quad [80]$$
$$+ \tan^{-1}\left(\frac{dZ(r_{1s})}{dr_{1s}}\right)\Bigg]$$
$$+ u\tan\left(\sin^{-1}\left\{n\sin\left[\sin^{-1}\left(\frac{1}{n}\sin\left\{\sin^{-1}\left[n\sin\left(\tan^{-1}\left(\frac{dz(r_{1o})}{dr_{1o}}\right)\right.\right.\right.\right.\right.$$
$$\left.\left.\left.\left.\left.-\sin^{-1}\left\{\frac{1}{n}\sin\left[\tan^{-1}\left(\frac{dz(r_{1o})}{dr_{1o}}\right)\right]\right\}\right)\right]\right\}\right)\right] - \tan^{-1}\left(\frac{dZ(r_{1s})}{dr_{1s}}\right)\right\}\right)$$
$$\left.+\tan^{-1}\left(\frac{dZ(r_{1s})}{dr_{1s}}\right)\right]\right\}\right)$$

3.4.2.4 Advances in Geometrical Methods for Laser Beam Shaping

Snell's law for the propagation of rays through an optical system and the intensity law as applied to geometrical optics provide the basis for designing the outer surface of the sombrero lens to form a plateau fill in the centre of the annular ring at the image (output) plane. Shealy and Chao[166] comment on the need to also set a constant optical path length constraint in their optical design. This is due to the nature of the design which makes use of aspheric lenses to transform a collimated input Gaussian profile to a collimated uniform output profile. This requires that the input and output wave fronts are both planar and that there is a constant optical path length between input and output reference planes for all rays. The constraints and concepts used for designing the surfaces in Shealy and Chao's paper[166] are similar to designs detailed by

Kreuzer's 1969 patent[144] and in an earlier paper by Frieden[167]. Kreuzer[144] commented on the ability of a two lens system such as this to transform any input irradiance profile into any desired output profile provided both input and output beams were collimated (i.e. both input and output wave fronts are planar). Later Rhodes and Shealy[168] developed a set of differential equations which allow the aspherical surface profiles of the two lenses in such a system to be computed numerically. Cornwell[169] produced a seven step procedure by which to design any aspherical two lens laser beam shaping system successfully provided that the input and output beams are collimated. Cornwell's paper[169] is not readily available in the literature but the seven step procedure he gave is summarised in Shealy and Chao's paper[166] and in reference [136]. Shealy and Wang[170] used parallel methods to those employed by Shealy and Chao[166] to design a two lens GRIN (Gradient of Refractive Index) system to perform the same beam transformation. In another collaborative paper Shealy and Chao[171] use optimisation based techniques in ZEMAX along with their own merit function to design an identical system. GRIN beam shapers of this type have the advantage of having spherical rather than aspherical surfaces simplifying the manufacture process somewhat. Where aspherical surfaces are difficult and hence expensive to manufacture, gradient index glasses are available off the shelf and require only spherical surface machining.

3.4.3 Design Methodology

The design objective in the next section of this thesis is to shape the outer section of the sombrero lens to create a uniform irradiance profile in the centre of an annular ring from the outer portion[t] of an input Gaussian beam. There are several reasons why employing the designs detailed in the literature would not be sensible. The first is that it is only the outer portion rather than the whole of the Gaussian input intensity profile which is used to construct the uniform profile at the output reference (image) plane. The second is that the shape of the first lens is predetermined to allow the annular ring created by the central section of the second lens to be focussed at the image plane. Shaping of only the outer section of the second lens is permitted in this

[t] The inner portion of the input beam is used to create the annular ring itself just as in the prototype design

design. The final motive is that no part of the output beam from the second lens is collimated which disqualifies the constant optical path length condition from being used in the design process. The methods used in the design of the optical elements in the next section of this thesis are similar however in some respects to the methods used in the literature. Although the constant optical path length constraint is not present here, the use of both Snell's Law and the Intensity Law are central to obtaining a solution to the beam shaping problem. A summary of the four design steps is as follows:

- Method for Determining the Focal Length of the Objective Lens and Lens Separation.
- Method for Determining the Axicon Angle of the Sombrero Lens Central Section
- Method for Determining the Semi-Diameter of the Central and Outer Sections
- Method for Determining the Surface of the Sombrero Lens Outer Section.

Each step will now be explained in detail.

3.4.3.1 Method for Determining the Focal Length of the Objective Lens and Lens Separation.

Choosing the focal length of the objective lens and the lens separation of the objective and sombrero lenses is about using common sense rather than conforming to exact formulae. It requires knowledge of the consequences of making these values too large or too small to choose them appropriately. The focal length of the objective lens will determine the workpiece stand-off and the annular ring spread as well as the depth of field at the focal region of the annular ring. The focal length of the lens must therefore be long enough to avoid an impracticable stand-off and too shallow a depth of field yet short enough that the annular ring spread is sufficient to give the sharp drop-off in intensity at the edge of the ring essential for achieving a steep sided surface temperature distribution pattern. The lens separation will determine the width and hence intensity of the beam entering the sombrero lens as well as determining the stand-off distance between the second surface of the sombrero lens and the focal position of the annular ring. Too great a beam intensity at the sombrero

lens may cause it to fail[u] and too small a stand-off distance may cause obstruction to processing of some surfaces[v]. For these reasons the separation cannot be too large. Aside from these practical reasons there is a also an important design motivation for keeping the separation small – the design relies on there being a large spread of energy over the first surface lens in order to easily proportion the energy passing through each section of the lens. The separation should therefore be chosen to be as small as is practicable.

3.4.3.2 Method for Determining the Axicon Angle of the Sombrero Lens Central Section

After choosing a suitable objective lens focal length and setting an appropriate lens separation, the angle of the Axicon central section of the lens must be chosen to determine the semi-diameter of the annular ring. Determining the annular ring diameter will lay the foundations on which the rest of the output profile will be built. The ring diameter will govern the overall footprint size of the beam and therefore must be chosen carefully so that it is suitable for the application.

The angle of the Axicon section can be calculated using equation [32].

3.4.3.3 Method for Determining the Semi-Diameter of the Central and Outer Sections

The semi-diameter of the central section must now be determined. This is accomplished by considering both the overall size of the lens and the upper limit of the proportion of the laser power which needs to be transmitted through the outer section in order to make up the plateau fill in the centre of the annular ring. A sensible additional point to remember in this step of the design process is to remember that the beam width which enters any lens should be no more than around 70% of the overall diameter of the lens. This will ensure that there is no clipping of the beam as it passes through the optical system thus reducing the risk of interference effects or power loss. The upper limit of the proportion of the power which must pass

[u] The high thermal gradient may cause the lens to crack or the lens or coating may simply burn out
[v] A lens placed too close to the workpiece may cause access to some surfaces to become difficult for example

through the outer section of the lens is determined by assessing the approximate relative intensity of the plateau fill compared with the maximum intensity of the base annular ring profile. To calculate the proportion of power needed through the outer section of the sombrero lens to give this maximum intensity differential the functions describing both the plateau fill and the annular ring must be defined and then integrated.

The annular ring function and its integral are given by equations [40] and [41].

The function describing the plateau fill is that of a top-hat function:

$$I_{PL}(r_{img}) = I_{0PL} \quad [81]$$

This intensity can be described as a proportion of the maximum intensity of the annular ring:

$$I_{0PL} = kI_{0AR} \quad [82]$$

Where k is an experimentally obtained constant of proportionality. The constant k is determined by assessing the maximum intensity of the plateau fill (relative to the intensity of the annular ring) required to achieve a uniform ΔTDP at the highest Péclet number the beam shaping system will be used at. Here this is chosen to be 0.355 as this was the relative intensity of the plateau fill required to achieve a uniform ΔTDP at a Péclet number of 96 in chapter 2 of this thesis. The constant k would be increased if a higher Péclet number dictated so for any application. However, a Péclet number of 96 is deemed sufficient at present as the overwhelming majority of the target applications operate below this Péclet number.

Integrating the plateau fill with respect to r and θ up to a maximum of r_{PL} (the maximum radius of the central intensity feature which we shall set as the ring diameter of the annular ring) gives the power contained within:

$$P_{PL}(\infty) = P_{PL}(r_{PL}) = \pi I_{0PL} r_{PL}^2 \quad [83]$$

If the following ratio is made:

$$\frac{P_{PL}(\infty)}{P_{AR}(\infty)+P_{PL}(\infty)} \qquad [84]$$

Then this allows us to calculate the proportion of power required through the outer section of the lens independently of the absolute maximum intensities of the annular ring and plateau fill. Substituting equations [80], [82] and [83] into equation [84] and cancelling terms gives:

$$\frac{P_{PL}(\infty)}{P_{AR}(\infty)+P_{PL}(\infty)}=\frac{kr_{PL}^2}{\frac{2\sqrt{\pi}w_{0AR}b}{\sqrt{2}}+kr_{PL}^2} \qquad [85]$$

Assuming the maximum semi-diameter of the lens is fixed as per the earlier recommendation its size compared with the maximum width of the beam is:

$$r_{maxS}=\frac{w_{0S}}{0.7} \qquad [86]$$

The semi-diameter of the central section can now be calculated.

This is completed by first making the same ratio from the expressions describing the power through the outer section and the total power of the Gaussian function at the sombrero lens and then equating this with the right hand side of equation [85]. After cancelling terms and rearranging for r_{AX}:

$$r_{AX}=\sqrt{-\frac{0.49r_{maxS}^2}{2}ln\left\{\frac{kr_{PL}^2}{\frac{2\sqrt{\pi}w_{0AR}b}{\sqrt{2}}+kr_{PL}^2}\right\}} \qquad [87]$$

Since w_{0AR} is dependent on r_{AX}, equation [65] needs to be solved simultaneously with equation [34].

Alternatively, the maximum radius of the sombrero lens may be kept open, specifying instead the radius of the central section first so as to ensure the maximum ring width w_{0AR} of the annular ring is controlled. In this case: the following equation can be obtained for the full semi-diameter of the sombrero lens:

$$r_{maxS} = \frac{1}{0.7}\sqrt{\frac{-2r_{AX}^2}{ln\left\{\frac{kr_{PL}^2}{\frac{2\sqrt{\pi}w_{0AR}b}{\sqrt{2}} + kr_{PL}^2}\right\}}} \quad [88]$$

3.4.3.4 Method for Determining the Surface of the Sombrero Lens Outer Section.

Now that the central-section and overall semi-diameter of the sombrero lens have been determined, all that is left to determine is the surface sag of its outer-section. The surface must be such that it transforms the input intensity profile into the desired shape at the image plane. This is accomplished by splitting the input intensity profile into a number of concentric ring shaped elements each containing equal amounts of energy. Rays can then be constructed along the boundary between the elements. Since the proximity and position of consecutive rays determines the intensity at a given position, redirecting them to cross the image plane at a different position will re-determine the intensity at that position. Once the position of the rays at the image plane has been determined to give the desired output intensity profile, the surface of the outer section can then be calculated. By calculating the gradient of the surface required to redirect a given ray to its new position at the image plane, a map of the gradient $dZ(r_{1S})/dr_{1S}$ vs. radial position r_{1S} can be built up. This can then be numerically integrated to determine the actual surface $Z(r_{1S})$.

The intensity profile entering the outer surface of the sombrero lens is split up into a predetermined number of ring shaped elements by the following method:

Integrating the relevant portion of the profile and dividing it by the number of elements desired N determines the power contained within each element. Equating the power contained within each element with the integral of the input profile from a radius r_n to a larger radius r_{n+1} and rearranging for r_{n+1} gives the position of the boundary between elements 1 and 2 - the starting position of element 1 (r_1) is determined by the inner radius of the outer section of the lens (r_{AX}):

$$\frac{P(r_{AX},\infty)}{N} = 2\pi \int_{r_n}^{r_{n+1}} I_{0S} e^{\left(\frac{-2r^2}{w_{0s}^2}\right)} r dr \qquad [89]$$

After carrying out the integration and rearranging for r_2:

$$r_{n+1} = \sqrt{-\frac{w_{0s}^2}{2} \ln\left\{e^{\left(\frac{-2r_n^2}{w_{0s}^2}\right)} - \frac{1}{N} e^{\left(\frac{-2r_{AX}^2}{w_{0s}^2}\right)}\right\}} \qquad [90]$$

For each r_{n+1} calculated this value can be used as the new r_n in the consecutive calculation, allowing construction of all the elements after a sufficient number of repeat calculations.

The boundaries between the elements can each be viewed as a ray[w]. Since the intensity of each element at the first surface of the sombrero lens, the position of the rays and the power contained in each element can be quantified, the new positions of any two consecutive rays further along the optical axis will redefine the intensity of the element between them. Using this information, the desired intensity at the image plane can be used to calculate the position of each ray at the image plane required to achieve that intensity. Thus the rays are remapped onto the image plane in a prescribed manner in order to reshape the intensity profile. In this case the desired intensity at the image plane is uniform (or independent of r_{img}). This makes the calculations of the new ray positions much simpler than for a complex output intensity profile which is dependent on r_{img} where there would be a co-dependence of I_{img} and r_{img}. The intensity of a uniform profile at the image plane can be calculated by considering the total power of the intensity distribution which is equal to the power entering the outer section of the lens. The total power of a uniform distribution (or plateau fill in our annular ring) with a maximum radius r_{PL} can be calculated by integrating the intensity from 0 to r_{PL} as follows:

$$P_{PL}(\infty) = 2\pi \int_0^{r_{PL}} I_{0PL} r dr \qquad [91]$$

[w] The geometrical construction of the path of light through a medium.

This yields:

$$P_{PL}(\infty) = \pi I_{0PL} r_{PL}^2 \qquad [92]$$

For a single element this becomes:

$$\frac{P_{PL}(\infty)}{N} = \frac{\pi I_{0PL} r_{PL}^2}{N} \qquad [93]$$

For the first element entering the sombrero lens (from r_1 (r_{AX}) to r_2), r_1 is mapped to $r_{1(img)}=0$ to ensure the profile at the image plane is continuous across the optical axis. The remapped position of r_2 can be calculated to give $r_{2(img)}$ by considering its position to give an intensity of I_{0PL} for the element between these rays. This can be achieved by integrating the function from $r_{1(img)}$ to $r_{2(img)}$ or in more general terms from $r_{n(img)}$ to $r_{n+1(img)}$ as follows:

$$2\pi \int_{r_{n(img)}}^{r_{n+1(img)}} I_{0PL} r dr = \pi I_{0PL} \left(r_{n+1(img)}^2 - r_{n(img)}^2\right) \qquad [94]$$

Equating this with the power contained within a single element and rearranging for $r_{n+1(img)}$ gives:

$$r_{n+1(img)} = \sqrt{\frac{r_{PL}^2}{N} - r_{n(img)}^2} \qquad [95]$$

Each ray is mapped onto the image plane in this way beginning with r_1 and continuing to the final (outermost) ray, r_{N+1}[x].

Now that the rays have been remapped the gradient of the surface of the outer section of the lens can be calculated. This is accomplished by calculating the gradient of the slope required to remap the rays at the first surface of the sombrero lens to their new positions at the image plane. To do this the ray tracing equations can be used to calculate gradient of the slope of the sombrero lens required at each ray position.

[x] There need to be N+1 rays to ensure the last element is enclosed

If $dz(r_{1o})/dr_{1o}$, u, d, $z(r_{1o})$, τ_S and n are given, then any incoming ray r_{1o} can be directed to a position r_{img} at the image plane by adjusting the value of the derivative of the outer surface of the sombrero lens $dZ(r_{1S})/dr_{1S}$ at r_{1S}. This can be completed numerically using equation [80]. The function for the actual surface $Z(r_{1S})$ can be found by numerically integrating $dZ(r_{1S})/dr_{1S}$

It is important to note at this point that the calculated surface of the sombrero lens is dependent amongst other things on w_{0S}. Therefore if this is altered after the lens surface design has been fixed as would happen during use of this system, the output intensity profile will be altered in ways which may not be ideal. To illustrate this point and the workings of the design a real beam shaping system has been designed for use with a laser system similar to that used in the testing of the prototype beam shaping system.

3.4.4 Design and Modelling of Optimal Dynamic Beam Shaper for Use with a CO2 Laser

The design will transform a circular Gaussian input beam of radius 4.5mm and wavelength 10.6μm into an output ring shaped beam with a ring radius of 2mm and a plateau fill central intensity feature as shown in Figure 27, plot C in section 2.5.2. The beam profile will be modulated by controlling the magnification M of the input beam between M=1.12 and M=3.69. A summary of the lens design parameters, input beam parameters and resultant calculated image related parameters is given in Table 2.

Table 2: Lens, input beam and image related parameter summary

Lens Design Parameters								
f_o(mm)	R_o(mm)	n	τ_o(mm)	τ_s(mm)	d(mm)	θ_{AX}(rad)	r_{AX}(mm)	r_{minS}(mm)
190	266.6	2.40	7.87	4.0	12.0	-0.0084	7.11	19.0
Input Beam Parameters			**Output Image Parameters**					
M^2	λ(μm)	w_{0in}(mm)	b(mm)	w_{0AR}(mm)	r_{PL}(mm)	u(mm)	β	k
1	10.6	14.45	2	0.180	1.820	170.7	33.3	0.355

The gradient of the outer surface required to give a uniform fill at the maximum input beam radius in the centre of the annular ring (up to an image radius of r_{PL}) is calculated solving equation [80] numerically for $dZ(r_{1S})/dr_{1S}$ using equation [95] where r_{img} appears. A plot of the calculated $dZ(r_{1S})/dr_{1S}$ is shown in Figure 54.

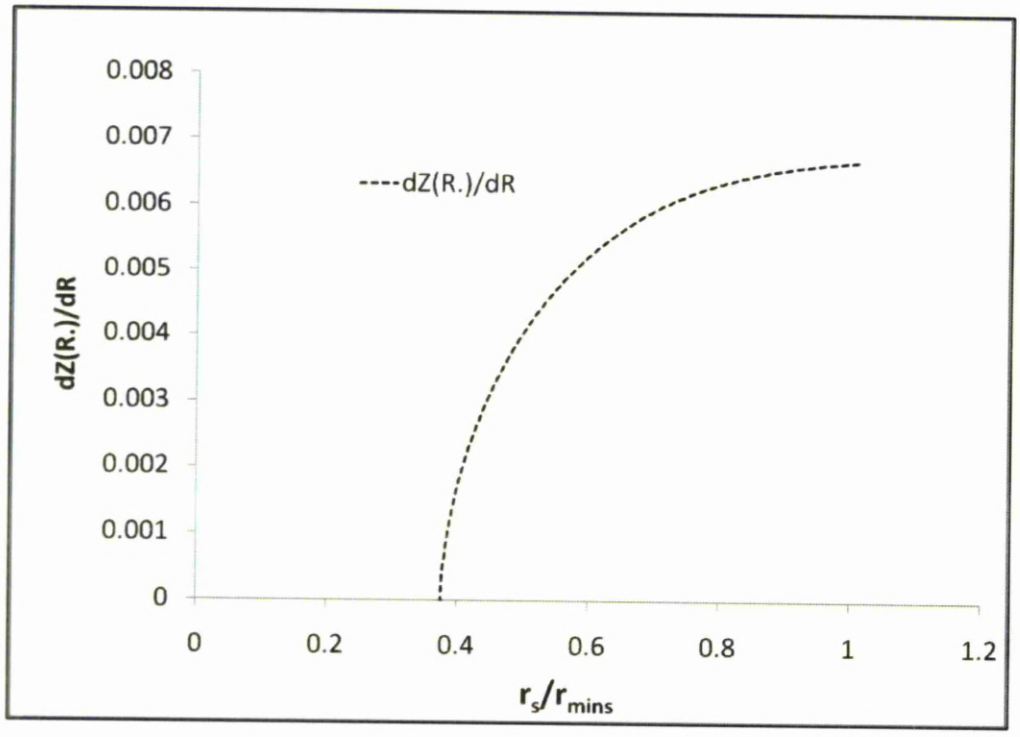

Figure 54: plot of calculated gradient of outer surface of the sombrero lens.

The gradient is calculated to give a uniform fill in the centre of the annular ring when the beam at the first surface of the sombrero lens is at the maximum allowable radius calculated using equation [88]. This ensures that any power loss due to the size of the maximum aperture is less than 1.5%. The surface sag can be calculated by numerically integrating dZ(r)/dr. This is completed by splitting the area under Figure 54 into trapezia. The first value, $Z(r)_1$, is chosen. Subsequent values $Z(r)_{N+1}$ are calculated from their preceding values $Z(r)_N$ using the following formula:

$$Z(r)_{N+1} = Z(r)_N + \frac{1}{2}(r_{N+1} - r_N)\left(\frac{dZ(r_N)}{dr_N} + \frac{dZ(r_{N+1})}{dr_{N+1}}\right) \qquad [96]$$

A dimensionless plot of the actual lens surface including the Axicon central section is shown in Figure 55.

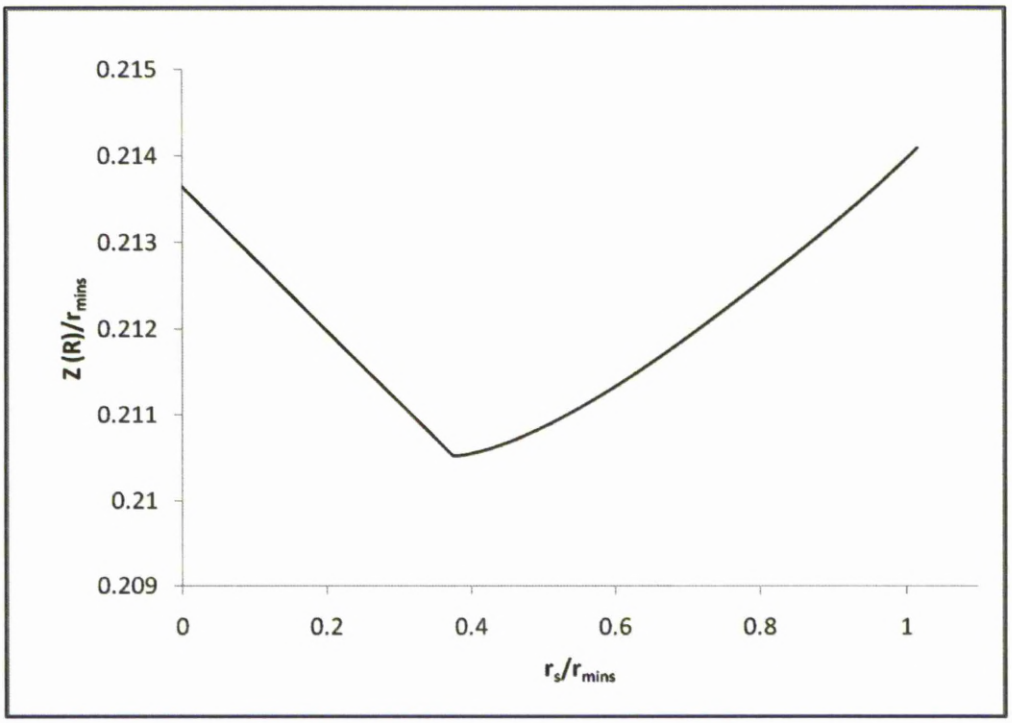

Figure 55: Calculated dimensionless lens surface profile.

The ray tracing program uses equation [80] to calculate the position of any input ray at the image plane after it has passed through the objective and sombrero lenses. The rays are separated at regular intervals as they enter the objective lens and the power contained between any two rays is calculated by carrying out the following integral of the Gaussian input beam between r_n and r_{n+1}:

$$P(r_n, r_{n+1}) = 2\pi \int_{r_n}^{r_{n+1}} I_{0in} e^{\left(\frac{-2r^2}{w_{0in}^2}\right)} r dr$$
$$= \frac{\pi I_{0in} w_{0in}^2}{2} \left\{ e^{\left(-\frac{2r_n^2}{w_{0in}^2}\right)} - e^{\left(-\frac{2r_{n+1}^2}{w_{0in}^2}\right)} \right\} \quad [97]$$

Position of each ray at the image plane is given by equation [80] and the intensity of the output ray between any two rays can be calculated by considering the power between them from equation [97] and their positions. This is made possible by considering that the integral of the output beam between two rays can be carried out as follows:

$$2\pi \int_{r_{n(img)}}^{r_{n+1(img)}} I_{out} r dr = \pi I_{out}\left(r_{n+1(img)}^2 - r_{n(img)}^2\right) \qquad [98]$$

This makes the approximation that the portion of the beam between r_n and r_{n+1} has uniform intensity. I_{out} between any two rays can then be calculated by combining equations [97] and [98] to give:

$$I_{out} = \frac{I_{0in} w_{0in}^2}{2\left(r_{n+1(img)}^2 - r_{n(img)}^2\right)} \left\{ e^{\left(-\frac{2r_n^2}{w_{0in}^2}\right)} - e^{\left(-\frac{2r_{n+1}^2}{w_{0in}^2}\right)} \right\} \qquad [99]$$

A reasonable plot of the output intensity profile can be obtained by completing this sequence numerically provided that the spacing between input rays is sufficient to give adequate resolution in both the input and output intensity profiles. Here the rays were separated at the objective by splitting the beam entering the outer section of the sombrero lens into 200 elements. The output intensity profile obtained for the maximum input beam radius w_{0in} of 13.78mm is shown in Figure 56.

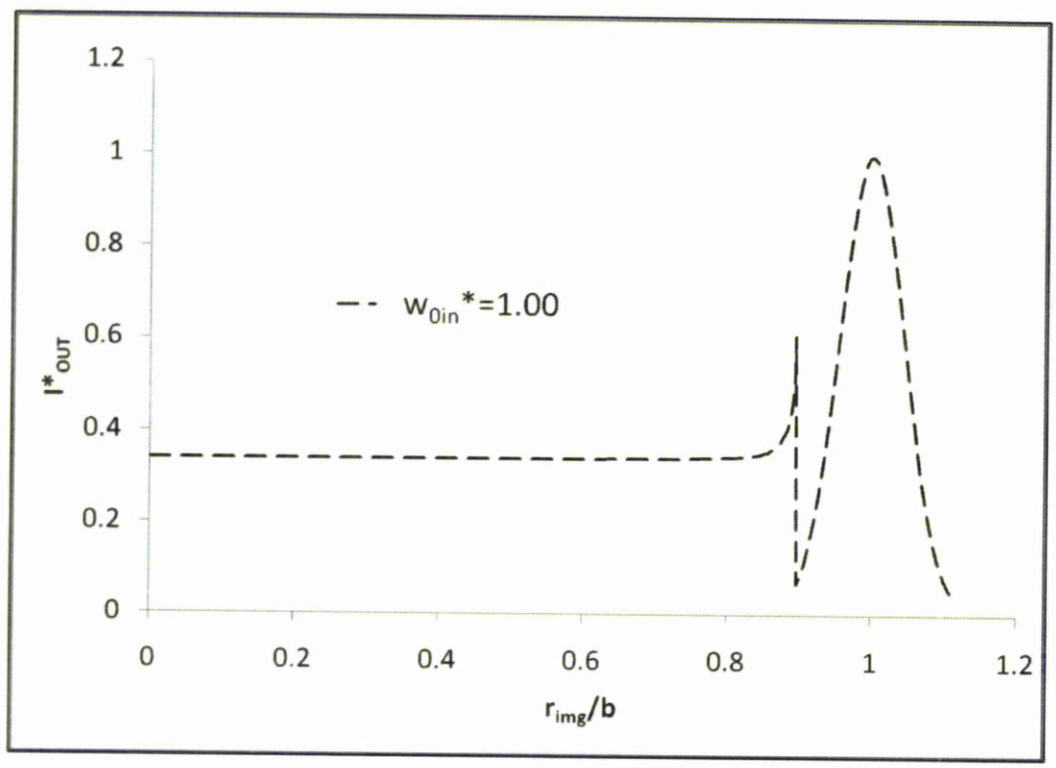

Figure 56: Output intensity profile at w_{0in}=1.00.*

The discontinuity in the output profile is due to the sudden curtailment of the central intensity feature brought about by the finite aperture. The increase in the intensity at $r_{img}/b \approx 0.88$ is due to the overlap with the annular ring. The effect on the output intensity profile brought about by changing the input beam diameter can be seen in Figure 57 below.

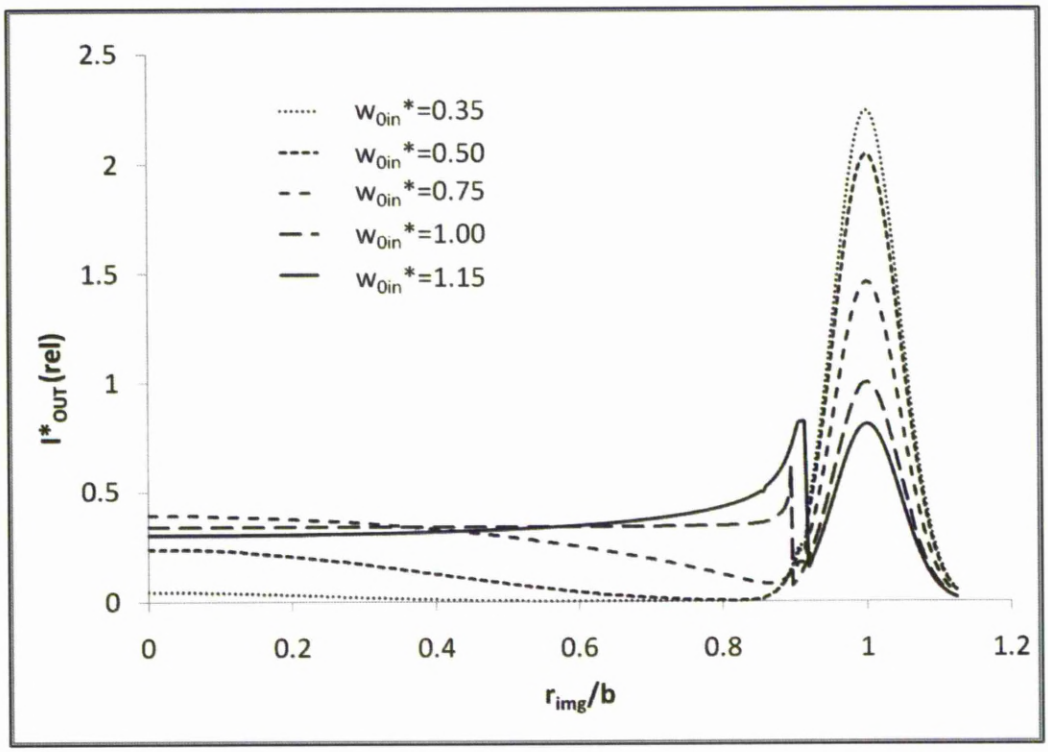

Figure 57: Output intensity (normalised to I_{0AR} at w_{0in}=1.00) calculated for a variety of w_{0in}*.*

The lens in this case is designed to give a uniform fill in the centre of the annular ring at an input beam radius w_{0in}*=1.00. If the beam diameter is reduced from this value the maximum intensity of the annular ring increases due to a greater proportion of power being directed through the central (Axicon) section of the sombrero lens. The shape of the central intensity feature is altered due to the adjusted input beam radius. Perhaps a little surprising is that the maximum intensity of the central feature actually increases when w_{0in}* is reduced to 0.75. This is due to power conservation which leads to the increase in maximum intensity I_{0in} of the input beam when w_{0in} is decreased. As w_{0in}* is decreased yet further to w_{0in}*=0.50 the central intensity feature changes again in both shape and size. At w_{0in}*=0.35 the central intensity

feature almost disappears completely as the power transmitted through the outer section of the sombrero lens approaches zero.

The goal of designing the outer section in this way was to attempt to produce a uniform central intensity feature which could be adjusted in magnitude to adjust for different Péclet numbers when using the beam for uniform surface heating. The change in beam diameter needed to bring about the modulation of the relative size of the central intensity feature has caused a secondary effect in that the intensity profile of the central feature is also changed. It may seem that this is an indication of the failure of the design to live up to its objective. This could be a serendipitous discovery however - the change in intensity profile using an input beam radius other than the one the lens is designed for could be advantageous. The relative beam profiles shown in Figure 57 are tested using the heat transfer model as detailed in section 2.2. A plot of the uniformities achieved over a range of Péclet numbers is shown below in Figure 58 along with the dynamic intensity profiles studied in section 2.5.2.

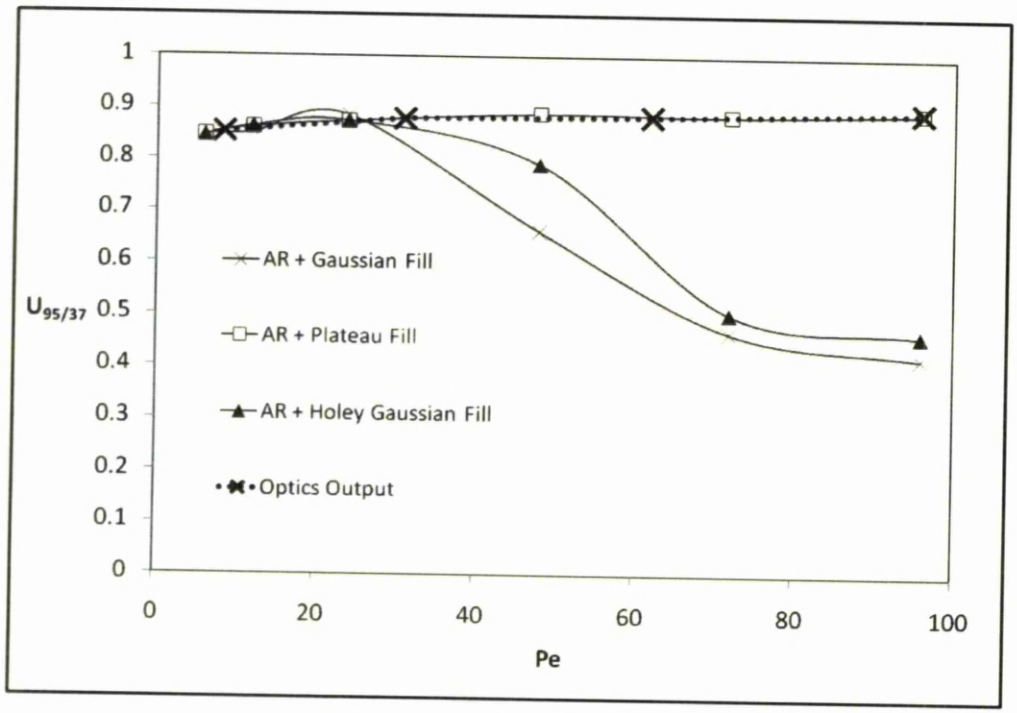

Figure 58: Uniformity vs. Péclet number for the output profiles created by the optimised optics. The dynamic intensity profiles studied in section 2.5.2 are included for comparison.

The output profiles from obtained from the optics design are clearly well suited to achieving high uniformities. Indeed they are on a par with (though no better than) the plateau fill dynamic intensity profiles even at higher Péclet numbers.

3.4.5 Conclusions

It has been shown in section 3.3 that it is possible to create an annular ring output intensity profile which contains a central intensity feature whose relative size can be modulated by adjusting the input beam diameter. This is made possible by adjusting the input beam diameter entering a two lens system comprised of a focussing lens and sombrero lens. The sombrero lens has a split section surface comprised of an Axicon central section and a concave outer section. The design of the prototype was completed using simple lens equations and a set of basic energy conservation equations for the power through the central and outer sections to predict the output intensity profile of an annular ring with a holey-Gaussian central intensity feature. As discussed in section 2.5.2, a variable holey-Gaussian central intensity feature is less than ideal for uniform surface treatments in the conduction limited region (at higher Péclet numbers). Also discussed in 2.5.2 is a variable plateau fill central intensity feature which is much more effective in the conduction limited region. This finding provided the motivation for the use of geometrical optics approximations to shape an aspheric outer section for the sombrero lens in order to create this type of feature. A method was described using Snell's Law for the propagation of rays through the lens system and the intensity law for conservation of energy within a bundle of rays to design the outer surface to give a plateau fill central intensity feature at a set input beam magnification. An example lens system with a maximum aperture radius of 19mm was designed for use with a CO_2 laser to create an output intensity profile with an annular ring (peak to centre) radius of 2mm. The output intensity profile created by the lens was modelled using a basic ray tracing program which was based on Snell's law and the intensity law. At the input beam diameter used in the design of the lens, the modelled profile showed good agreement with the intended profile (an annular ring with a plateau fill). Any change in the beam diameter did adjust the relative size of the central intensity feature as desired – the shape of this feature was also changed. The output profiles obtained at 5 different input beam magnifications

(including that which was used in the design of the lens) were modelled and tested in the heat transfer model as detailed in section 2.2. It was shown that the lens was able to produce the range of intensity profiles required to give a uniform maximum temperature rise on the surface of a material over a wide range of Péclet numbers producing uniformities on a level with those achieved with the plateau-fill profiles in section 2.5.2.

4 Summary and Recommendations for Future Work

4.1 Summary

This thesis has provided a solution to a laser surface heating problem which has implications for a number of laser surface heat treatments including laser transformation hardening and laser surface annealing and a limited number of laser surface melting treatments including laser surface melting, laser surface alloying and laser cladding. The problem can be summarised as follows:

- In laser surface treatments uniformity in the material properties obtained after heating is often highly desirable.
- In order to achieve uniformity, there are several existing solutions which fall into three main categories:
    - i Rapidly scanning the beam and/or overlapping adjacent passes
    - ii Shaping the transverse beam intensity profile
    - iii Shaping the transverse beam outline geometry
- For non-circular beam geometries and circularly asymmetric beam intensity profiles, processing directionality is important in determining the temperature distribution pattern in the material. Therefore for any beam to have an effect which is independent of processing direction, it must be circular and have a circularly symmetric intensity profile.
- Overheating of the centre of the treated area under the path of the moving beam occurs when using a circular beam with a Gaussian or top-hat shaped intensity profile. This is due to lateral conduction losses and the reduction in interaction time for areas further from the centre of the path of the moving beam.
- The reduction in interaction time and lateral conduction losses at the edge of the treated area can be compensated for by using an annular ring intensity profile. The annular ring profile must have a sharply defined outer edge. The

highest uniformities in the maximum temperature rise across the width of the treated area achievable are those using a low spread annular ring at a low Péclet number. If high uniformities are to be achieved at higher Péclet numbers then increasing the spread of an annular ring is a possible solution. This decreases the level of uniformity achievable however.

- If the Péclet number is altered (by altering the beam traverse speed or thermal diffusivity of the material) then the effectiveness of any fixed beam intensity profile in achieving a uniform maximum temperature rise on the surface of a material is also altered. Therefore the beam profile must be modulated to accommodate for changes to the Péclet number if it is to be effective over a wide range of Péclet numbers.

A successful solution to this problem is investigated in chapter 2 and can be summarised as follows:

- Using a base annular ring intensity profile to which a plateau fill central intensity feature is added in controlled amounts can create a dynamic intensity profile which is capable of achieving high uniformities in the ΔTDP over a wide range of Péclet numbers. This is due to the following factors:

    i The base annular ring – a full-Gaussian annular ring with a small spread - by itself is optimal for achieving high uniformities at low Péclet numbers.

    ii Increases to the Péclet number can be accommodated by introducing the plateau fill intensity feature in the centre of the annular ring and increasing the relative size of this feature at higher Péclet numbers. This compensates for the reduced conduction from the edges to the centre of the treated area which occurs under these conditions.

    iii The presence of the base annular ring ensures the outer edges of the intensity profile remain sharp over all Péclet numbers.

iv The plateau fill in the centre of the annular ring is superior to the other fills investigated (Gaussian and holey-Gaussian) as it has the ability to maintain high uniformities at higher Péclet numbers.

- The central intensity feature can be varied in order to control the temperature distribution at a depth beneath the surface as well as at the surface itself. Under-sizing of the central intensity feature can cause overheating of the edges of the treated area at the surface. However overheating the outer edges of the treated area on the surface can lead to higher uniformities at a depth beneath the surface.

- Although the heating and cooling rates across the width of the treated area cannot be controlled when using a circular beam, the maximum temperature reached can be controlled using the dynamic beam intensity profile. This may provide the extra flexibility needed to fulfil the thermal history required to execute some of the surface transformations the research is aimed at.

Creating the ideal dynamic intensity profile in a heat transfer modelling environment is sufficient for theoretical studies of solutions to existing laser surface heat treatment problems. If these problems are to be solved in the real world, however, then an appropriate optics solution must be devised. Chapter 3 has dealt with this issue in two ways:

- A prototype optical system has been devised, built and tested to replicate the annular ring with variable holey-Gaussian intensity profile discussed in Chapter 2 and to provide proof of the beam profile modulation mechanism;

- A method is devised for designing an optimised optical system to replicate the annular ring with variable plateau fill intensity profile discussed in Chapter 2 for any laser system. An example of such a system is designed for a CO_2 laser beam.

The prototype optical system consists of an objective lens combined with a sombrero lens and is designed for use with a CO_2 laser using basic lens equations, geometric constructions of the beam path and conservation of energy principles. The sombrero

lens is a split-section lens with an Axicon central section and a concave outer section. When combined with the objective lens it creates a focussed annular ring with holey-Gaussian central intensity feature. The beam profile is modulated by adjusting the beam diameter entering the objective lens. This adjusts the power ratio between the portion of the beam entering the outer section and that entering the central section which has the effect of adjusting the relative size of the holey-Gaussian feature compared with the annular ring at the image plane. The prototype optical system is built using zinc-selenide components and is tested on a CO_2 laser system by taking beam prints of the output intensity at the image plane. The tests showed successful modulation of the relative size of the holey-Gaussian intensity feature compared with the annular ring although the holey Gaussian feature was noticeably distorted due to diffraction effects.

The optimised optical system is similar to the prototype but has an aspheric outer section to create a plateau fill in the centre of the annular ring. A method has been devised for designing such an optical system for any laser system provided that geometrical approximations remain a reasonable approximation. The method can be summarised as follows:

- Selection of the objective lens, Axicon angle of the central section of the sombrero lens and lens separation is carried out to form an annular ring with the desired peak to centre radius and spread and an appropriate depth of field and working distance.

- The semi-diameter of the central and outer sections of the sombrero lens are determined using the principle of conservation of energy to allow a sufficient proportion of the beam to pass through the outer section of the lens when operating the system at higher Péclet numbers.

- The surface shape of the outer section is then designed using the intensity law and geometrical ray tracing to determine the derivative of the surface required to give a plateau fill in the centre of the annular ring at the largest possible input beam magnification.

An optimised system for use with a CO_2 laser beam has been analysed using a numerical ray tracing procedure built on geometrical optics approximations. The analysis concluded the following:

- At the input beam diameter used in the design process, the lens system gives the predicted output profile of an annular ring with a plateau fill in the centre.
- When the input beam diameter is reduced from this value, the shape and relative size of the central intensity feature are altered. The size reduces as intended – but the shape is also altered so that the intensity is higher in the centre of the profile than at the inner edge of the annular ring.
- When the input beam diameter is increased from that used in the design process, the relative size of the central intensity feature is increased and the shape is distorted such that the intensity at the inner edge of the annular ring becomes greater than that at the centre of the profile.

The output profiles for a number of different input beam magnifications were then fed into the finite element heat conduction model and tested in the same way as the dynamic profiles suggested in chapter 2. The outcome of the tests showed that despite the distortion of the central intensity feature the output profiles from the optical system were as effective in achieving high uniformities over a range of Péclet numbers as the plateau fill dynamic beam intensity profile suggested in chapter 2.

4.2 Limitations of the Research

The methodology employed in this research limited somewhat the reach and scope of the findings. Firstly uniformity was only optimised for the first of the three thermal history requirements set out by Davis et al[90]. The time spent above the threshold temperature and the heating and cooling rates across the width of the treated area were represented graphically. However further analysis needs to be completed in this area, namely the quantification of the uniformity obtained in these the second and third thermal history requirements. Any uniformity in these temporal characteristics is a by-product of the uniformity obtained in the maximum temperature achieved since no attempt was made to optimise uniformity in this way. With uniformity in the

temporal characteristics left to the consequence of optimising uniformity in the maximum temperature, it has yet to be determined whether true uniformity in the finished surface properties could be achieved using the techniques and designs detailed in this thesis. However it may well be possible to achieve a high degree of uniformity using the optical system reported due to the extent to which the optical system allows control of the intensity profile. By adjusting the intensity profile within the limits allowed by the optical system and with careful control of other parameters such as the laser power or traverse speed, it may be possible to remain within acceptable limits for all three of the thermal history requirements set out by Davis et al[90].

Melting was not considered in the finite element model employed this thesis. Therefore contributions to the temperature field by heat and mass convection are not taken into account and this limits the findings predominantly to laser heating processes. As shown in Figure 2 convection plays a significant role in determining the temperature distribution in the material in most of the melting processes in the literature. Therefore the findings of this thesis cannot be applied to the majority of laser melting processes with the exception of very low Prandlt number materials where the process Ch^2 is high enough. A caveat to including even these exceptions within the sphere of relevance of this research is that the latent heat of melting is not taken into account. This may produce significant differences in the temperature field obtained to that modelled which would reduce the usefulness of the findings contained here. The flexibility of the optical system in controlling the intensity profile may mean that changes to the temperature distribution brought about by convection and the latent heat of melting could be accommodated. However although it is not inconceivable that the optical system may be able to achieve the same for melting processes that it has for heating processes, this has yet to be determined and is a subject for future research.

As the optical system was designed using geometrical optics approximations, the effects of diffraction are ignored in the calculations. This is normally fine for laser wavelengths as geometrical optics approximations are essentially short wavelength approximations. However at CO_2 laser wavelengths, which are an order of magnitude

greater than that of most other lasers, it can become easy to fall in to the region where Romero and Dickey[136] advise that diffraction effects must be taken into account. The value of β for the system designed for a CO_2 laser in section 3.4.4 is already close to the lower limit of 32 set by Romero and Dickey[136] but if the size of the input output beam is reduced by even a small amount then the system is in the limit where diffraction effects need to be taken into account in order that the intended intensity profile(s) are obtained. This is much less of a concern for systems designed for lasers with shorter wavelengths due to the effect this has on the value of β.

4.3 Building and Testing the Optimised Optics System

Although tested in a modelling environment the optimised optics system as yet to be built and tested in the real world. Proof of concept of the beam profile modulation mechanism has already been provided however in section 3.3.4. The sombrero lens can be manufactured accurately using diamond-point turning techniques whereas the focussing (objective) lens is available off-the-shelf. The variable beam expander (zoom lens) used to change the input beam diameter can be built using off-the-shelf lenses to construct a Donder's telescope. A Donder's telescope is an afocal zoom lens system which allows graduated magnification of a collimated beam. Ideally the output beam profile from the sombrero lens should be analysed using a beam analyser such as a camera for visible/near IR wavelengths or a spinning needle for mid IR wavelengths. The effect of the moving beam on the surface temperature distribution should be tested using high resolution thermal analysis equipment such as a thermal camera (as opposed to a pyrometer). Finally the effectiveness of the output intensity for laser surface treatments should be assessed. This could include processes such as laser transformation hardening and laser surface annealing. The flexibility of the output intensity profile will undoubtedly provide the potential for improvement in uniformity of achieved surface properties in these processes.

4.4 Building a Dynamic Beam Shaper for Non Circular Beam Geometries

To control uniformity in all three of the thermal history requirements set out by Davis et al[90], a square or line shaped beam geometry with elevated intensity at the edges has been shown by other authors to be highly effective[4, 131]. The intensity profiles created by these authors however are nonetheless only designed for use at one Péclet number. To be effective over a range of Péclet numbers it would be necessary to modulate the relative intensity of the edges of the profiles in relation to the intensity of the centre just as in the case of the dynamic profiles investigated in this thesis. Completing this task using a dynamic beam shaping system similar to those discussed in Chapter 3 of this thesis is not beyond the realms of possibility. Using beam integration techniques as discussed in section 3.2.3 could be one solution. If the lenslets in the centre of the array were prism-like to form a double line pattern then the surrounding lenslets could be shaped so as to form a uniform square or rectangle between the lines to simulate the 'rugby posts' beam shape by Gibson et al[4] shown in Figure 12 in section 2.4.2. The proportion of power through the outer lenslets could be varied in the same way as in the optical design in this thesis – by adjusting the diameter of the beam entering the lenslet array. Increasing the beam diameter would increase the proportion of power through the outer lenslets - thus increasing the relative power of the uniform fill in the centre of the high intensity lines.. The ideal dynamic beam shaping system for uniform surface treatments would recreate Burger's armchair beam as shown in Figure 14 in section 2.4.2 with the ability to adjust both the relative intensity at the edges compared with the centre and the rate of drop-off in power towards the trailing edge of the beam. This has the potential to allow creation of a square or strip of highly uniform surface temperature on almost any material over a range of Péclet numbers.

Bibliography

1. Chen, B.T., D.R. Huang, and S. Lee, *Transient temperature profiles in a rectangular thin film due to a scanning uniform strip heat source.* Journal of Physics D-Applied Physics, 2001. **34**(6): p. 985-992.
2. D. Triantafyllidis, L.L., F.H. Stott, *The Effect of Beam Shape in Laser Surface Treatment of Ceramics*, in *21st ICALEO*. 2002, Laser Institute of America.
3. Dubovskii, P.E., et al., *Surface Hardening Of Steels With A Strip-Shaped Beam Of A High-Power Co2-Laser.* Kvantovaya Elektronika, 1994. **21**(12): p. 1183-1185.
4. Gibson, M.T.J.H., R, *Novel Computer Generated Diffractive Optics Modifying Beam Characteristics To Improve The Microstructures Of Directly Deposited Inconel*, in *27th ICALEO*. 2008, Laser Institute of America: Temecula, CA.
5. Kar, A., J.E. Scott, and W.P. Latham, *Effects of mode structure on three-dimensional laser heating due to single or multiple rectangular laser beams.* 1996. p. 667-674.
6. Kell, J.T., J; Higginson, R; Thomson, R; Jones, J; Noden, S, *Holographic Diffractive Optical Elements Allow Improvements In Conduction Laser Welding Of Steels*, in *25th ICALEO*. 2006, Laser Institute of America.
7. Leung, M.K.H., H.C. Man, and J.K. Yu, *Theoretical and experimental studies on laser transformation hardening of steel by customized beam.* International Journal of Heat and Mass Transfer, 2007. **50**(23-24): p. 4600-4606.
8. Miyamoto, I.M., H, *Novel Laser Beam Shaping Optics: LSV Optics Applications to Transformation Hardening and Ceramic Joining*, in *11th ICALEO*. 1992, Laser Institute of America.
9. Safdar, S., L. Li, and M.A. Sheikh, *Numerical analysis of the effects of non-conventional laser beam geometries during laser melting of metallic materials.* Journal of Physics D-Applied Physics, 2007. **40**(2): p. 593-603.
10. Safdar, S., et al., *An analysis of the effect of laser beam geometry on laser transformation hardening.* Journal of Manufacturing Science and Engineering-Transactions of the Asme 2006. **128**(3): p. 659-667.
11. Safdar, S., et al., *Thermal history analysis of surface heating of mild steel with different laser beam geometries.* Proceedings of the Institution of Mechanical Engineers Part C-Journal of Mechanical Engineering Science 2006. **220**(10): p. 1549-1557.
12. Safdar, S.L., L; Sheikh M, A; Liu, Z, *The Effect Of Beam Geometry On Stress Distribution In Laser Bending Of Tubes*, in *24th ICALEO*. 2005, Laser Institute of America.
13. Triantafyllidis, D., L. Li, and F.H. Stott, *Investigation of the effects of nonconventional beam geometries in laser surface treatment of ceramics: Theoretical analysis.* Journal of Laser Applications, 2006. **18**(2): p. 161-168.
14. Zeng, D., W.P. Latham, and A. Kar, *Shaping of annular laser intensity profiles and their thermal effects for optical trepanning.* Optical Engineering, 2006. **45**(1).
15. Safdar, S., et al., *An analysis of the effect of laser beam geometry on laser transformation hardening*. 2006. p. 659-667.

16. Safdar, S., et al., *Thermal history analysis of surface heating of mild steel with different laser beam geometries.* 2006. p. 1549-1557.
17. Gratzke, U., P.D. Kapadia, and J. Dowden, *Heat-Conduction in High-Speed Laser-Welding.* Journal of Physics D-Applied Physics, 1991. **24**(12): p. 2125-2134.
18. Leung, M., *Phase-change heat transfer in laser transformation hardening by moving Gaussian rectangular heat source.* Journal of Physics D-Applied Physics, 2001. **34**(24): p. 3434-3441.
19. Postacioglu, N., P. Kapadia, and J. Dowden, *A Mathematical-Model of Heat-Conduction in a Prolate Spheroidal Coordinate System with Applications to the Theory of Welding.* Journal of Physics D-Applied Physics, 1993. **26**(4): p. 563-573.
20. Robert, A. and T. Debroy, *Geometry of laser spot welds from dimensionless numbers.* Metallurgical and Materials Transactions B-Process Metallurgy and Materials Processing Science, 2001. **32**(5): p. 941-947.
21. Steen, W.M., *Laser Material Processing.* 3rd ed. 2003, London: Springer-Verlag.
22. Tobar, M.J., et al., *Laser transformation hardening of a tool steel: Simulation-based parameter optimization and experimental results.* Surface & Coatings Technology, 2006. **200**(22-23): p. 6362-6367.
23. Yang, L.J., S. Jana, and S.C. Tam, *The Effects of Pre-Hardening on the Laser Transformation-Hardening of Tool-Steel Specimens.* Journal of Materials Processing Technology, 1991. **25**(3): p. 321-332.
24. Shang, H.M., *On the Width and Depth of Hardened Zones During Laser Transformation Hardening of Tool Steels.* Journal of Materials Processing Technology, 1990. **23**(1): p. 65-72.
25. Yang, L.J., S. Jana, and S.C. Tam, *The Effects of Overlapping Runs in the Laser-Transformation Hardening of Tool-Steel Specimens.* Journal of Materials Processing Technology, 1990. **23**(2): p. 133-147.
26. McKeown, N., W.M. Steen, and D.G. McCartney, *Laser Transformation Hardening of Engine Valve Steels,* in *Icaleo 90 : Laser Materials Processing,* S.L. Ream, F. Dausinger, and T. Fujioka, Editors. 1991, Laser Inst America: Orlando. p. 469-479.
27. Androsov, A.P., et al., *Laser Hardening of Diesel-Engine Valve.* Metal Science and Heat Treatment, 1988. **30**(1-2): p. 67-70.
28. Lin, Y.C., et al., *Studies on Chip Control in Turning by Partially Laser Hardening of Carbon Steel.* Journal of Advanced Mechanical Design Systems and Manufacturing, 2009. **3**(1): p. 13-21.
29. Kito, T., et al., *Prevention of Burr Formation in Face Milling of Carbon Steel by Laser Hardening,* in *Progress of Machining Technology,* R. Fan, et al., Editors. 2009, Trans Tech Publications Ltd: Stafa-Zurich. p. 672-675.
30. Selvan, J.S., K. Subramanian, and A.K. Nath, *Effect of laser surface hardening on En18 (AISI 5135) steel.* Journal of Materials Processing Technology, 1999. **91**(1-3): p. 29-36.
31. Mavi, H.S., et al., *Raman-Study of Stress-Relieved Silicon-on-Sapphire Films Prepared by Cw-Laser Annealing.* Journal of Applied Physics, 1991. **69**(11): p. 7815-7819.

32. Chou, C.F., H.C. Pan, and C.C. Chou, *Electrical properties and microstructures of PbZrTiO3 thin films prepared by laser annealing techniques.* Japanese Journal of Applied Physics Part 1-Regular Papers Short Notes & Review Papers, 2002. **41**(11B): p. 6679-6681.
33. Liou, B.H., C.C. Yu, and C.C. Chou, *Low temperature preparation of PZT thin films on different substrates by CO2 laser annealing.* Ferroelectrics, 2007. **357**: p. 792-+.
34. Tsai, S.D., M.B. Suresh, and C.C. Chou, *Improvement in ferroelectric properties of PZT thick films prepared by a modified sol-gel technique using low temperature laser annealing.* Physica Scripta, 2007. **T129**: p. 175-179.
35. Stultz, T.J. and J.F. Gibbons, *The Use of Beam Shaping to Achieve Large-Grain Cw Laser-Recrystallized Polysilicon on Amorphous Substrates.* Applied Physics Letters, 1981. **39**(6): p. 498-500.
36. Sameshima, T., *Laser crystallization for large-area electronics.* Applied Physics a-Materials Science & Processing, 2009. **96**(1): p. 137-144.
37. Edited by Mazumder, J.C., O; Villar, R; Steen, W, *Laser Processing: Surface Treatment and Film Deposition.* Series E: Applied Science. Vol. 307. 1994, Dordrecht/ Boston/ London: Kluwer Academic Publishers.
38. Lee, S.Z. and K.H. Zumgahr, *Surface Treatments of Al2o3-Ceramics by Co2-Lasers.* Materialwissenschaft Und Werkstofftechnik, 1992. **23**(4): p. 117-123.
39. Strutt, P.R., et al., *Laser Surface Melting of High-Speed Tool Steels.* Materials Science and Engineering, 1978. **36**(2): p. 217-222.
40. Colaco, R. and R. Vilar, *Laser surface melting and post-heat treatment of AISI 420 stainless tool steel*, in *Surface Modification Technologies Xi*, T.S. Sudarshan, M. Jeandin, and K.A. Khor, Editors. 1998, Inst Materials: London. p. 600-606.
41. Dahotre, N.B., A. Hunter, and K. Mukherjee, *Laser Surface Melting of W2 Tool Steel - Effects of Prior Heat-Treatment.* Journal of Materials Science, 1987. **22**(2): p. 403-406.
42. Kwok, C.T., et al., *Laser surface melting of martensitic stainless steel 440C for enhancing corrosion resistance*, in *First International Symposium on High-Power Laser Macroprocessing*, I. Miyamoto, et al., Editors. 2003, Spie-Int Soc Optical Engineering: Bellingham. p. 493-498.
43. Akkurt, A.S., O.V. Akgun, and N. Yakupoglu, *The effect of post-heat treatment of laser surface melted AISI 1018 steel.* Journal of Materials Science, 1996. **31**(18): p. 4907-4911.
44. Wade, N., T. Koshihama, and Y. Hosoi, *Improvement of Oxidation Resistance of Stainless-Steels by Laser Surface Melting.* Scripta Metallurgica, 1985. **19**(7): p. 859-864.
45. Kaul, R., et al., *A Novel Preweld Laser Surface Treatment for Enhanced Intergranular Corrosion Resistance of Austenitic Stainless Steel Weldments.* Welding Journal, 2009. **88**(12): p. 233S-242S.
46. Akgun, O.V., et al., *Effect of Laser Surface Melting on Tensile Properties of Type-304l Stainless-Steel.* Scripta Metallurgica Et Materialia, 1992. **27**(2): p. 191-194.
47. Baptista, M.O.S. and R. Vilar, *Laser surface melting of a mottled cast iron.* Lasers in Engineering, 1999. **9**(1): p. 57-75.

48. Blarasin, A., et al., *Development of a Laser Surface Melting Process for Improvement of the Wear-Resistance of Gray Cast-Iron.* Wear, 1983. **86**(2): p. 315-325.
49. Tomlinson, W.J. and M.G. Talks, *Shot Peening, Laser Surface Melting and the Cavitation Erosion of an Austenitic Gray Iron.* Journal of Materials Science, 1991. **26**(3): p. 804-808.
50. Biswas, A., et al., *Laser surface treatment of Ti-6Al-4V for bio-implant application.* Lasers in Engineering, 2007. **17**(1-2): p. 59-73.
51. Nowak, K.M., H.J. Baker, and D.R. Hall, *Efficient laser polishing of silica micro-optic components.* Applied Optics, 2006. **45**(1): p. 162-171.
52. Gaffet, E., J.M. Pelletier, and S. Bonnetjobez, *Laser Surface Alloying of Ni Film on Al-Based Alloy.* Applied Surface Science, 1989. **43**: p. 248-255.
53. Draper, C.W., et al., *Laser Surface Alloying of Gold-Films on Nickel.* Applied Surface Science, 1981. **7**(3): p. 276-280.
54. Kumar, D., et al., *Laser surface alloying of Ni-Mo into stainless steel 304 substrates.* Lasers in Engineering, 1998. **7**(2): p. 103-117.
55. Suh, J.H., et al., *Laser surface alloying on alloy 600 to improve its resistance to corrosion.* Proceedings of the Eighth International Symposium on Environmental Degradation of Materials in Nuclear Power Systems - Water Reactors, Vols 1 and 2, 1997: p. 475-482.
56. Garcia, I. and J.J. De Damborenea, *Corrosion properties of TiN prepared by laser gas alloying of Ti and Ti6Al4V.* Corrosion Science, 1998. **40**(8): p. 1411-1419.
57. deDamborenea, J., et al., *Hard coatings by laser gas alloying of Ti6Al4V.* International Journal of Materials & Product Technology, 1996. **11**(3-4): p. 301-309.
58. Babu, S.S., et al., *Reactive gas shielding during laser surface alloying for production of hard coatings.* Surface & Coatings Technology, 2006. **200**(8): p. 2663-2671.
59. Klimpel, A., A. Lisiecki, and D. Janicki, *The influence of the shielding gas on the properties of a laser-melted surface of austenitic stainless steel.* Proceedings of the Institution of Mechanical Engineers Part B-Journal of Engineering Manufacture, 2004. **218**(9): p. 1137-1144.
60. Manna, I., et al., *Laser surface alloying of ferritic steel to enhance oxidation resistance.* Surface Engineering: in Materials Science I, 2000: p. 367-376.
61. Gutierrez, A. and J. deDamborenea, *Laser-surface-alloying of the iron based superalloy Incoloy-800H with Al.* Applied Physics a-Materials Science & Processing, 1996. **63**(5): p. 461-465.
62. Abboud, J.H. and D.R.F. West, *Processing Aspects of Laser Surface Alloying of Titanium with Aluminum.* Materials Science and Technology, 1991. **7**(4): p. 353-356.
63. Ariely, S., et al., *Laser Surface Alloying of Steel with Tic.* Surface & Coatings Technology, 1991. **45**(1-3): p. 403-408.
64. Man, H.C., S. Zhang, and F.T. Cheng, *Improving the wear resistance of AA 6061 by laser surface alloying with NiTi.* Materials Letters, 2007. **61**(19-20): p. 4058-4061.

65. Tomida, S. and K. Nakata, *Fe-Al composite layers on aluminum alloy formed by laser surface alloying with iron powder.* Surface & Coatings Technology, 2003. **174**: p. 559-563.
66. Kwok, C.T., H.C. Man, and F.T. Cheng, *Cavitation erosion-corrosion behaviour of laser surface alloyed AISI 1050 mild steel using NiCrSiB.* Materials Science and Engineering a-Structural Materials Properties Microstructure and Processing, 2001. **303**(1-2): p. 250-261.
67. Shin, J.K., et al., *Corrosion resistance of alloy 600 surface-alloyed by laser beam,* in *Laser Materials Processing Conference, Pts 1 & 2 - Icaleo '97*, R. Fabbro, A. Kar, and A. Matsunawa, Editors. 1997, Laser Inst America: Orlando. p. F108-F117.
68. Carroll, J.W., et al., *Laser surface alloying of aluminum 319 alloy with iron,* in *20th Icaleo 2001, Vols 92 & 93, Congress Proceedings.* 2001, Laser Inst America: Orlando. p. 885-894.
69. Jiang, P., et al., *Wear resistance of a laser surface alloyed Ti-6Al-4V alloy.* Surface & Coatings Technology, 2000. **130**(1): p. 24-28.
70. Huang, C.C., W.T. Tsai, and J.T. Lee, *Surface modification of carbon steel with laser treated nitrogen-containing stainless steel layers.* Surface & Coatings Technology, 1996. **79**(1-3): p. 67-70.
71. Sinha, V., et al., *Selective area laser surface alloying of mild steel with carbon,* in *Surface Engineering: in Materials Science I*, S. Seal, et al., Editors. 2000, Minerals, Metals & Materials Soc: Warrendale. p. 131-140.
72. Das, D.K., K.S. Prasad, and A.G. Paradkar, *Evolution of Microstructure in Laser-Surface Alloying of Aluminum with Nickel.* Materials Science and Engineering a-Structural Materials Properties Microstructure and Processing, 1994. **174**(1): p. 75-84.
73. Levcovici, S.M., et al., *Laser surface hardening of austenitic stainless steel.* Journal of Materials Engineering and Performance, 2000. **9**(5): p. 536-540.
74. ZumGahr, K.H., *Modeling and microstructural modification of alumina ceramic for improved tribological properties.* Wear, 1996. **200**(1-2): p. 215-224.
75. Xiong, Z., G.X. Chen, and X.Y. Zeng, *Effects of process variables on interfacial quality of laser cladding on aeroengine blade material GH4133.* Journal of Materials Processing Technology, 2009. **209**(2): p. 930-936.
76. Vilar, R., et al., *Structure of NiCrAlY coatings deposited on single-crystal alloy turbine blade material by laser cladding.* Acta Materialia, 2009. **57**(18): p. 5292-5302.
77. Sexton, L., et al., *Laser cladding of aerospace materials.* Journal of Materials Processing Technology, 2002. **122**(1): p. 63-68.
78. Shepeleva, L., et al., *Laser cladding of turbine blades.* Surface & Coatings Technology, 2000. **125**(1-3): p. 45-48.
79. Schubert, E., et al., *Laser beam cladding: A flexible tool for local surface treatment and repair.* Journal of Thermal Spray Technology, 1999. **8**(4): p. 590-596.
80. Yang, Y.L., et al., *Microstructure and wear properties of TiCN/Ti coatings on titanium alloy by laser cladding.* Optics and Lasers in Engineering. **48**(1): p. 119-124.

81. Wang, X.H., et al., *Microstructure and Wear Properties of In Situ Synthesized VC Carbide Reinforced Fe-based Surface Composite Coating Produced by Laser Cladding.* Tribology Letters, 2009. **34**(3): p. 177-183.
82. Ng, K.W., et al., *Laser cladding of copper with molybdenum for wear resistance enhancement in electrical contacts.* Applied Surface Science, 2007. **253**(14): p. 6236-6241.
83. Buytoz, S., *Microstructural properties of SiC based hardfacing on low alloy steel.* Surface & Coatings Technology, 2006. **200**(12-13): p. 3734-3742.
84. Chao, M.J. and E.J. Liang, *Effect of TiO2-doping on the microstructure and the wear properties of laser-clad nickel-based coatings.* Surface & Coatings Technology, 2004. **179**(2-3): p. 265-271.
85. Cadenas, M., et al., *Wear behaviour of laser cladded and plasma sprayed WC-Co coatings.* Wear, 1997. **212**(2): p. 244-253.
86. Yang, D.H. and X.H. Zhang, *The Friction and Wear of Metals Modified by a Continuous-Wave Co2-Laser.* Surface & Coatings Technology, 1994. **63**(1): p. 43-48.
87. Osvay, K., I. Kepiro, and O. Berkesi, *Laser treatment of white China surface.* Applied Surface Science, 2006. **252**(13): p. 4516-4522.
88. Képíró, I., K. Osvay, and M. Divall, *Correction of small imperfections on white glazed china surfaces by laser radiation.* Applied Surface Science, 2007. **253**(19): p. 7798-7805.
89. Sato, T., et al., *Laser-assisted Direct Write for aerospace applications.* Proceedings of the Institution of Mechanical Engineers, Part G: Journal of Aerospace Engineering.
90. Davis, M., et al., *Heat Hardening of Metal-Surfaces with a Scanning Laser-Beam.* Journal of Physics D-Applied Physics, 1986. **19**(10): p. 1981-1997.
91. Ion, J.C., H.R. Shercliff, and M.F. Ashby, *Diagrams for Laser Materials Processing.* Acta Metallurgica Et Materialia, 1992. **40**(7): p. 1539-1551.
92. Rosenthal, D., *Mathematical theory of heat distribution during welding and cutting.* Weld J, 1941. **20**(5): p. 220-234.
93. Carslaw, H.J., J, *Conduction of Heat in Solids.* 2nd ed. 1959, Oxford.
94. Christensen, N.D., V and Gjermundsen, K, *The Distribution of Temperature in Arc Welding.* British Welding Journal, 1965. **9**(3/4): p. 112-132.
95. Eagar, T.W.a.T., N. S, *Temperature fields produced by traveling distributed heat sources.* Welding Journal, 1983. **62**(12): p. 346-355.
96. Perktold, K. and G. Rappitsch, *Computer-Simulation of Local Blood-Flow and Vessel Mechanics in a Compliant Carotid-Artery Bifurcation Model.* Journal of Biomechanics, 1995. **28**(7): p. 845-856.
97. Chavanis, P.H., *Relativistic stars with a linear equation of state: analogy with classical isothermal spheres and black holes.* Astronomy & Astrophysics, 2008. **483**(3): p. 673-698.
98. *COMSOL Multiphysics 3.3a.* 2007, COMSOL AB.: Stockholm, Sweden.
99. Foster, W.J., et al., *The fluid mechanics of scleral buckling surgery for the repair of retinal detachment.* Graefe's Archive for Clinical and Experimental Ophthalmology. **248**(1): p. 31-36.

100. Shashank, A., et al., *Design, simulation and fabrication of a low cost capacitive tactile shear sensor for a robotic hand.* Conf Proc IEEE Eng Med Biol Soc, 2009. **2009**: p. 4132-5.
101. Bianco, N., O. Manca, and D. Ricci, *Numerical Model for Multilayer Thin Films Irradiated by a Moving Laser Source*, in *Diffusion in Solids and Liquids Iv*, A. Ochsner, G.E. Murch, and A. Shokuhfar, Editors. 2009, Trans Tech Publications Ltd: Stafa-Zurich. p. 352-357.
102. Bianco, N., et al., *Transient Heat Conduction in Solids Irradiated by a Moving Heat Source*, in *Diffusion in Solids and Liquids Iv*, A. Ochsner, G.E. Murch, and A. Shokuhfar, Editors. 2009, Trans Tech Publications Ltd: Stafa-Zurich. p. 358-363.
103. Chakraborty, N. and S. Chakraborty, *Thermal transport regimes and generalized regime diagram for high energy surface melting processes.* Metallurgical and Materials Transactions B-Process Metallurgy and Materials Processing Science, 2007. **38**(1): p. 143-147.
104. Chakraborty, N., *Thermal transport regimes and effects of prandtl number in molten pool transport in laser surface melting processes.* Numerical Heat Transfer Part a-Applications, 2008. **53**(3): p. 273-294.
105. Dowden, J., *The Mathematics of Thermal Modelling: An Introduction to the Theory of Laser Materials Processing*. 2001, Boca Raton: Chapman & Hall/CRC.
106. Helebrant, A., C. Buerhop, and R. Weissmann, *MATHEMATICAL-MODELING OF TEMPERATURE DISTRIBUTION DURING CO2-LASER IRRADIATION OF GLASS*, in *Glass Technology*. 1993. p. 154-158.
107. Hirai, M. and S. Ishimoto, *THERMAL DIFFUSIVITIES AND THERMAL-CONDUCTIVITIES OF UO2-GD2O3*, in *Journal of Nuclear Science and Technology*. 1991. p. 995-1000.
108. Lu, Y.F., *LASER-INDUCED TEMPERATURE RISE IN SUBSTRATES WITH COMPLEX TEMPERATURE-DEPENDENCE IN THERMAL-CONDUCTIVITY*, in *Lasers in Engineering*. 1995. p. 45-50.
109. Murti, P.S. and C.K. Mathews, *THERMAL-DIFFUSIVITY AND THERMAL-CONDUCTIVITY STUDIES ON THORIUM-LANTHANUM MIXED-OXIDE SOLID-SOLUTIONS*, in *Journal of Physics D-Applied Physics*. 1991. p. 2202-2209.
110. Phanikumar, G., K. Chattopadhyay, and P. Dutta, *Modelling of transport phenomena in laser welding of dissimilar metals.* International Journal of Numerical Methods for Heat & Fluid Flow, 2001. **11**(2-3): p. 156-171.
111. Ehlen, G., et al., *Influence of convection and surface effects on macrosegregations in eutectic and peritectic systems*, in *Solidification and Gravity 2000*, A. Roosz, M. Rettenmayr, and D. Watring, Editors. 2000, Trans Tech Publications Ltd: Zurich-Uetikon. p. 105-110.
112. Phanikumar, G., P. Dutta, and K. Chattopadhyay, *Computational modeling of laser welding of Cu-Ni dissimilar couple.* Metallurgical and Materials Transactions B-Process Metallurgy and Materials Processing Science, 2004. **35**(2): p. 339-350.
113. Chakraborty, N. and S. Chakraborty, *Modelling of turbulent molten pool convection in laser welding of a copper-nickel dissimilar couple.* International Journal of Heat and Mass Transfer, 2007. **50**(9-10): p. 1805-1822.
114. Sarkar, S., et al., *Transport phenomena in laser surface alloying.* Journal of Materials Science, 2003. **38**(1): p. 155-164.

115. Chakraborty, N., *The effects of turbulence on molten pool transport during melting and solidification processes in continuous conduction mode laser welding of copper-nickel dissimilar couple.* Applied Thermal Engineering, 2009. **29**(17-18): p. 3618-3631.
116. Han, L. and F.W. Liou, *Numerical investigation of the influence of laser beam mode on melt pool.* International Journal of Heat and Mass Transfer, 2004. **47**(19-20): p. 4385-4402.
117. Li, J.F., L. Li, and F.H. Stott, *Thermal stresses and their implication on cracking during laser melting of ceramic materials.* Acta Materialia, 2004. **52**(14): p. 4385-4398.
118. Edited by Mazumder, J.C., O; Villar, R; Steen, W, *Proceedings of the NATO Advanced Study Institute on Laser Processing: Surface Treatment and Film Deposition*. 1994, Dordrecht, The Netherlands: Kluwer Academic Publishers.
119. Reed, R.C., et al., *Laser transformation hardening of steel: effects of beam mode, beam size, and composition*. 1999. p. 109-118.
120. Van Ingelgem, Y., et al., *Influence of laser surface hardening on the corrosion resistance of martensitic stainless steel*, in *Electrochimica Acta*. 2007. p. 7796-7801.
121. Kim, J.D., et al., *Laser transformation hardening on rod-shaped carbon steel by Gaussian beam*, in *Transactions of Nonferrous Metals Society of China*. 2009. p. 941-945.
122. Bonss, S.S., M; Brenner, B; Beyer, E. *Precise hardening with high power diode lasers using beam shaping mirror optics*. in *High-Power Diode Laser Technology and Applications, Proceedings of the SPIE*. 2003: SPIE.
123. Cole, C.E.N., S. C; Tyrer, J.R;, *The Application of Diffractive Optical Elements in High Power Laser Material Processing*, in *17th ICALEO*. 1998, Laser Institute of America: Orlando, FL.
124. Victor, B.R., S; Walters, C. T, *Custom Beam Shaping For High-Power Fiber Laser Welding*, in *27th ICALEO*. 2008, Laser Institute of America: Temecula, CA.
125. Bitterli, R.e.a., *Refractive Statistical Concave 1D Diffusers for Laser Beam Shaping*, in *Laser Beam Shaping IX*. 2008, SPIE.
126. Forbes, A.L., C. S; Litvina, I; Loveday, P. W; Belyi, V and Kazak, N. S, *Variable flattened Gaussian beam order selection by dynamic control of an intracavity diffractive mirror*, in *Laser Beam Shaping IX, Proceedings of SPIE* 2008, SPIE.
127. Herrit, G.H., A; Reedy, H, *Novel Focusing Optics For IR Lasers*, in *24th ICALEO*. 2005, Laser Institute of America.
128. Lu, Y.F., *Square-Shaped Temperature Distribution Induced By A Gaussian-Shaped Laser-Beam.* Applied Surface Science, 1994. **81**(3): p. 357-364.
129. Kar, A. and M.D. Langlais, *Optothermal effects of laser modes in laser materials processing.* Optical and Quantum Electronics, 1995. **27**(12): p. 1165-1180.
130. Sharp, M.C., *Mathematical Modelling of Continuous Wave CO2 Laser Processing of Materials*. 1986, University of London: London.
131. Hagino, H.A., H; Kikuta, H, *Development of Computer Generated Hologram for Laser Processing of a High Power Diode Laser*, in *ICALEO*. 2008, Laser Institute of America: Temecula, CA.
132. Burger, D., *Optermierung der Strahlqualitat beim Laserharten*, in *9th International Congress LASER '89*. 1989, Springer-Verlag: Berlin.

133. Triantafyllidis, D., L. Li, and F.H. Stott, *Investigation of the effects of nonconventional beam geometries in laser surface treatment of ceramics: Theoretical analysis*. 2006. p. 161-168.
134. Zeng, D., W.P. Latham, and A. Kar, *Shaping of annular laser intensity profiles and their thermal effects for optical trepanning*. 2006.
135. Crafer, R.C.O., P. J, *Heat Treatment of Workpiece by Laser*, E.P. Office, Editor. 1982: EU EP 0062 517.
136. Dickey, F.M.H., S. C (Editors), *Laser Beam Shaping: Theory and Techniques*. 2000, NY: Marcel Dekker Inc.
137. Kogelnik, H. and T. Li, *Laser Beams and Resonators*. Proceedings of the Institute of Electrical and Electronics Engineers, 1966. **54**(10): p. 1312-&.
138. Pare, C. and P.A. Belanger, *Custom Laser Resonators Using Graded-Phase Mirrors*. Ieee Journal of Quantum Electronics, 1992. **28**(1): p. 355-362.
139. Tao, S.H. and X.C. Yuan, *Mode shaping at a given distance outside a resonator with diffractive optical elements*. Journal of Optics a-Pure and Applied Optics, 2003. **5**(5): p. 511-514.
140. Karim, M.A., et al., *Realization of a Uniform Circular Source Using a Two-Dimensional Binary Filter*. Optics Letters, 1985. **10**(10): p. 470-471.
141. Almarzouk, K., *Generation of a Uniform Line Source Using a Binary Filter*. Optics Communications, 1980. **35**(2): p. 161-163.
142. Simmons, W.W., Leppelme.Gw, and B.C. Johnson, *Optical Beam Shaping Devices Using Polarization Effects*. Applied Optics, 1974. **13**(7): p. 1629-1632.
143. Belvaux, Y. and S.P.S. Virdi, *Method For Obtaining A Uniform Non-Gaussian Laser Illumination*. Optics Communications, 1975. **15**(2): p. 193-195.
144. Kreuzer, J.L., *Coherent Light Optical System Yielding an Output Beam of Desired Intensity Distribution at a Desired Equiphase Surface*, U.P. Office, Editor. 1969: US.
145. Shealy, D.L. and S.H. Chao, *Geometric optics-based design of laser beam shapers*. 2003. p. 3123-3138.
146. Zhang, S., G. Neil, and M. Shinn, *Single-element laser beam shaper for uniform flat-top profiles*. Optics Express, 2003. **11**(16): p. 1942-1948.
147. Wang, C. and D.L. Shealy, *DESIGN OF GRADIENT-INDEX LENS SYSTEMS FOR LASER-BEAM RESHAPING*. 1993. p. 4763-4769.
148. Hoffnagle, J.A. and C.M. Jefferson, *Design and performance of a refractive optical system that converts a Gaussian to a flattop beam*. Applied Optics, 2000. **39**(30): p. 5488-5499.
149. McDermit, J.H. and T.E. Horton, *Reflective Optics For Obtaining Prescribed Irradiative Distributions From Collimated Sources*. Applied Optics, 1974. **13**(6): p. 1444-1450.
150. Ocana, J.L., et al., *Laser heat treatments driven by integrated beams: role of irradiation nonuniformities*. Applied Optics, 1999. **38**(21): p. 4570-4576.
151. Weible, K.J., et al., *Randomly varying micro-optical elements for the generation of uniform intensity profiles in coherent laser sources - art. no. 70620R*, in *Laser Beam Shaping Ix*, A. Forbes and T.E. Lizotte, Editors. 2008, Spie-Int Soc Optical Engineering: Bellingham. p. R620-R620.
152. Unnebrink, L., et al., *Excimer laser beam homogenization for materials processing*, in *Optika '98 - 5th Congress on Modern Optics*, G. Akos, G.

Lupkovics, and A. Podmaniczky, Editors. 1998, Spie-Int Soc Optical Engineering: Bellingham. p. 126-129.
153. Dagenais, D.M., J.A. Woodroffe, and I. Itzkan, *Optical Beam Shaping of a High-Power Laser for Uniform Target Illumination.* Applied Optics, 1985. **24**(5): p. 671-675.
154. Brown, D.M. and J.D. Brown, *Multi-aperture beam integrators and odd-shaped irradiance patterns*, in *Laser Beam Shaping*, F.M. Dickey and S.C. Holswade, Editors. 2000, Spie-Int Soc Optical Engineering: Bellingham. p. 140-146.
155. Lee, W.H., *Method for Converting a Gaussian Laser-Beam into a Uniform Beam.* Optics Communications, 1981. **36**(6): p. 469-471.
156. Veldkamp, W.B., *Laser-Beam Profile Shaping with Binary Diffraction Gratings.* Optics Communications, 1981. **38**(5-6): p. 381-386.
157. Aleksoff, C.C., K.K. Ellis, and B.D. Neagle, *Holographic Conversion of a Gaussian-Beam to a near-Field Uniform Beam.* Optical Engineering, 1991. **30**(5): p. 537-543.
158. Duparre, M., et al., *Investigation of Computer-Generated Diffractive Beam Shapers for Flattening of Single-Modal Co2-Laser Beams.* Applied Optics, 1995. **34**(14): p. 2489-2497.
159. Wang, J.Y., et al., *Multifunctional diffractive optics element for high-energy laser system*, in *Apoc 2001: Asia-Pacific Optical and Wireless Communications: Optoelectronics, Materials, and Devices for Communications*, T.P. Lee and Q. Wang, Editors. 2001, Spie-Int Soc Optical Engineering: Bellingham. p. 369-379.
160. Waddle, A.J., et al., *Beam shaping diffractive optical elements for high power laser applications - art. no. 70700H*, in *Optical Technologies for Arming, Safing, Fuzing, and Firing Iv*, F.M. Dickey and R.A. Beyer, Editors. 2008, Spie-Int Soc Optical Engineering: Bellingham. p. H700-H700.
161. Βελανγερ, Π.α.Ρ., Μ, *Ring pattern of a lens-axicon doublet illuminated by a Gaussian.* Applied Optics, 1978. **17**(7).
162. Schwede, H.K., R; Hansel, K; Klos, M, *Multi Spot Laser Beam Processing*, in *20th ICALEO*. 2001, Laser Institute of America.
163. Enguebard, S. and B. Hatfield, *Continuous beam shaping with optical phased arrays using diffractive optics optimization*, in *2002 Ieee Aerospace Conference Proceedings, Vols 1-7*. 2002, Ieee: New York. p. 1417-1422.
164. Passilly, N., et al., *1-D laser beam shaping using an adjustable binary diffractive optical element.* Optics Communications, 2004. **241**(4-6): p. 465-473.
165. Shealy, D.L. and S.H. Chao, *Geometric optics-based design of laser beam shapers*, in *Optical Engineering*. 2003. p. 3123-3138.
166. Shealy, D.L. and S.H. Chao, *Geometric optics-based design of laser beam shapers.* Optical Engineering, 2003. **42**(11): p. 3123-3138.
167. Frieden, B.R., *Lossless Conversion Of A Plane Laser Wave To A Plane Wave Of Uniform Irradiance*, in *Applied Optics*. 1965. p. 1400-&.
168. Rhodes, P.W. and D.L. Shealy, *Refractive Optical-Systems for Irradiance Redistribution of Collimated Radiation - Their Design and Analysis.* Applied Optics, 1980. **19**(20): p. 3545-3553.
169. Cornwell, D.F., *Non-Projective Transformations in Optics.* Proceedings of the Society of Photo-Optical Instrumentation Engineers, 1981. **294**: p. 62-72.

170. Wang, C. and D.L. Shealy, *Design Of Gradient-Index Lens Systems For Laser-Beam Reshaping.* Applied Optics, 1993. **32**(25): p. 4763-4769.
171. Shealy, D.L. and S.H. Chao, *Design of GRIN laser beam shaping system*, in *Laser Beam Shaping V*, F.M. Dickey and D.L. Shealy, Editors. 2004, Spie-Int Soc Optical Engineering: Bellingham. p. 138-147.

Appendices

Appendix A Integrating the Gaussian Function

Integrating the Gaussian function gives us the total power entering the objective lens

$$P_{IN}(\infty) = 2\pi \int_0^{\infty} I_{0IN} e^{\left(\frac{-2r^2}{w_{0IN}^2}\right)} r dr$$

For the purposes of integrating by substitution let:

$$u = \frac{\sqrt{2}r}{w_{0IN}} \quad \therefore r = \frac{u w_{0IN}}{\sqrt{2}}$$

$$\frac{dr}{du} = \frac{w_{0IN}}{\sqrt{2}} \quad \therefore dr = \frac{w_{0IN}}{\sqrt{2}} du$$

now:

$$P_{IN}(\infty) = \pi I_{0IN} w_{0IN}^2 \int_0^{\infty} e^{(-u)^2} u du = -\frac{\pi I_{0IN} w_{0IN}^2}{2} e^{(-u)^2}$$

Substituting values of 0 and infinity for r (and hence u) to find the definite integral allows us to quantify the total Power in the Gaussian distribution based on the intensity and beam radius of the beam incident on the objective lens:

$$P_{IN}(\infty) = \frac{\pi I_{0IN} w_{0IN}^2}{2}$$

Appendix B: Integrating the Annular Ring Function

$$P_{AR}(\infty) = \int_0^{2\pi}\int_0^{\infty} I_{0AR} e^{\left(\frac{-2(r-b)^2}{w_{0AR}^2}\right)} r dr d\theta$$

Integrating with respect to $d\theta$ and taking I_{0AR} as a constant the following is obtained:

$$P_{AR}(\infty) = 2\pi I_{0AR}\int_0^{\infty} e^{\left(\frac{-2(r-b)^2}{w_{0AR}^2}\right)} r dr$$

Making the following substitutions:

$$u = \frac{\sqrt{2}(r-b)}{w_{0AR}} \quad \therefore r = \frac{u w_{0AR}}{\sqrt{2}} + b$$

$$dr = \left(\frac{dr}{du}\right) du \quad \therefore dr = \frac{w_{0AR}}{\sqrt{2}} du$$

The following is obtained:

$$P_{AR}(\infty) = 2\pi I_{0AR}\int_{\frac{-\sqrt{2}b}{w_{0AR}}}^{\infty} e^{(-u^2)} \frac{w_{0AR}}{\sqrt{2}}\left(\frac{u w_{0AR}}{\sqrt{2}} + b\right) du$$

Multiplying out we then obtain:

$$\left\{\pi I_{0AR} w_{0AR}^2 \int_{\frac{-\sqrt{2}b}{w_{0AR}}}^{\infty} e^{(-u^2)} u du\right\} + \left\{\frac{2\pi I_{0AR} w_{0AR} b}{\sqrt{2}} \int_{\frac{-\sqrt{2}b}{w_{0AR}}}^{\infty} e^{(-u^2)} du\right\}$$

Using the identities:

$$\int_0^u e^{-u^2} u du \equiv -\frac{1}{2} e^{-u^2}$$

And:

$$\int_0^u e^{-u^2} du \equiv \frac{\sqrt{\pi}}{2} \operatorname{erf}(u)$$

It follows that:

$$\left[-\frac{\pi I_{0AR} w_{0AR}^2}{2} e^{(-u^2)} + \frac{\pi\sqrt{\pi} I_{0AR} w_{0AR} b}{\sqrt{2}} \operatorname{erf}(u)\right]_{\frac{-\sqrt{2}b}{w_{0AR}}}^{\infty}$$

Where *erf(u)* is the error function which is twice the integral of the normal Gaussian distribution between *0* and *u*. Here, *erf(u)* has a value of 1 at ∞ and -1 at the lower limit since the ratio of *b* to w_0 is much greater than 1. $exp(-u^2)$ is 0 when *u* is at infinity and 0 at the lower limit since (in this case) u^2 yields a high value. Substituting in the upper and lower limits and simplifying an expression can be obtained for the total power in the annular ring:

$$P_{AR}(\infty) = \frac{2\pi\sqrt{\pi} I_{0AR} w_{0AR} b}{\sqrt{2}}$$